SLAC–374
UC–414
(E)

NEUTRAL KAON AND LAMBDA PRODUCTION IN ELECTRON-POSITRON ANNIHILATION AT 29 GeV AND THE Z BOSON RESONANCE*

Carrie Sue Fordham

Stanford Linear Accelerator Center
Stanford University
Stanford, California 94309

October 1990

Prepared for the Department of Energy
under contract number DE-AC03-76SF00515

Printed in the United States of America. Available from the National Technical Information Service, U.S. Department of Commerce, 5285 Port Royal Road, Springfield, Virginia 22161.

* Ph. D. thesis

Abstract

The production of K^0 and Λ in the hadronization of $q\bar{q}$ events from e^+e^- collisions at 29 GeV and the Z^0 resonance is studied using the Mark II detector as upgraded for running at the Stanford Linear Collider (SLC).

Hadronization processes cannot presently be calculated with Quantum Chromodynamics; instead, hadronization models must be used in comparisons with data. In these models, hadronization occurs at local energy scales of a few GeV, a level at which small differences in quark and diquark mass significantly affect the production of particles such as K^0 and Λ, the lightest neutral meson and baryon containing strange quarks. Their production and behavior in hadronic events is a test for the accuracy of our understanding of hadronization.

Two-charged-particle decays of the K^0 and Λ are isolated within the hadronic event sample. The resulting distributions of K^0 and Λ are corrected for inefficiencies and generalized to include all K^0 and Λ. The number of K^0 per hadronic event is found to be $1.26 \pm 0.04 \pm 0.14$ at 29 GeV and $1.54 \pm 0.21 \pm 0.18$ at the Z^0 resonance. The value at 29 GeV is consistent with other measurements and the models tuned at that energy. The value at 91 GeV is lower than some previous measurements at lower energy. Hadronization models predict a value about 3σ higher. The number of Λ per hadronic event is found to be $0.170 \pm 0.015 \pm 0.018$ at 29 GeV and $0.47 \pm 0.10 \pm 0.05$ at 91 GeV. The value at both energies is consistent with hadronization models and previous measurements.

Various kinematic distributions of the strange particles are examined. These distributions include the momentum and scaled momentum of the particles. The kinematics of the particles with respect to the original quark direction are

examined through the distributions of rapidity and momentum transverse to the thrust both in and out of the event plane. The dependence of K^0 and Λ production on the sphericity of the hadronic events is also examined. All these distributions show that the behavior of K^0 and Λ in hadronic events is consistent with the hadronization models.

Acknowledgements

Many people have helped to make this thesis possible; to thank all of them would require more paper than the thesis itself. The entire Mark II collaboration has contributed many things: time spent in building and maintaining the detector, time spent on shifts collecting the data, the code used to collect and process the data into forms which can be readily used in individual analyses, and a stimulating atmosphere in which to learn.

Some individuals in particular have made my career as a graduate student rewarding: first and most importantly, I would like to thank my advisor, Tom Himel, for teaching me much about methods of physics while leaving me free enough to learn from my own mistakes, and for providing a caring atmosphere in which to learn. I learned a great deal about methods of analysis from my collaboration on an earlier analysis with Sachio Komamiya, who has also provided much information and support for the analysis contained in this thesis. Discussions with Vera Luth have also provided insight into this analysis. And I would like to thank Chris Hearty, Dave Coupal, and Chang Kee Jung, who have always been willing to pause in their work to talk with students.

I would also like to thank my fellow graduate students for their continual help and support: my officemates Rick van Kooten, Jordan Nash, and Bob Jacobsen have always been ready to discuss problems or answer questions, as well as providing moral support and friendship. Kathy O'Shaughnessy and Christoph Von Zanthier have contributed much to this thesis with their analyses of hadronic events, and discussions of those analyses. Paul Weber has been of particular help, both with the intricacies of TeX and with problems arising in analysis, and with his long and

very valued friendship. Others whose friendship and insight have been important include Don Fujino, Dale Koetke, Dean Hinshaw, and Mike Yurko.

For providing diversion as well as knowledge, I would like to thank all of my friends. Thomas has provided support from abroad. I would also like to thank Guy, who has helped to keep me sane during the writing of this thesis. My roommates have sometimes had to exercise much patience with me while I wrote this thesis: for this I thank Michael and especially Judy, who knows little about physics but much about friendship.

Most of all, I would like to thank my family for their continual support and encouragement all through my life, without which I would never have reached this point.

CONTENTS

TABLES

Table

FIGURES

Figure

CHAPTER 1

INTRODUCTION

In 1894 some physicists believed that the field of physics was closed: that everything was fundamentally understood, and only applications of basic principles still needed to be calculated. At that time, atoms were believed to be the fundamental particles of matter, and electromagnetism and gravity were the only known forces. Two more years brought the discovery of radioactivity[1] and confusion to the field of physics. In the next year, Thomson deduced the existence of electrons,[2] a particle smaller than the atom and carrying charge. When they were found among the products of radioactive decay, physicists were forced to the conclusion that the atom was not a fundamental particle, but was instead made up of positive and negative charge. Rutherford's evidence that all the positive charge lay in a nucleus much smaller than the atom[3] provided the impetus for the development of quantum mechanics, and once again the field of physics was wide open.

The subsequent decades brought the discovery of a plethora of new particles. Theoretical efforts to explain all these discoveries struggled to keep up, using the new tools of quantum mechanics and quantum field theory. However, in the last two decades a theory has emerged which explains most of the known phenomena of particle physics very well: the Standard Model of Weinberg, Salam, and Glashow.[4][5]

The Standard Model has had great successes: the prediction of the W and Z bosons, the prediction of charm, etc. However, there are many things it does not explain, such as the number of fermion families and the gravitational force. Also, a key element in the Standard Model, the Higgs boson, has yet to be found by experiment. In general, physicists do not think it a complete theory, and

experiments have been searching for flaws in the model which will suggest in which direction theory should go next.

Some areas within the scope of the Standard Model are not well understood either. One of the chief of these is the production of hadrons in high energy collisions. When quarks are produced in such collisions, they do not appear singly in detecting equipment, but appear as a shower of hadrons. Quantum Chromodynamics, the theory of the strong force within the Standard Model, gives the basic reason for this phenomenon and gives some general predictions for the process. Unfortunately, it is at present opaque to anything more than general predictions; it cannot be used to calculate what happens on the small scale in the hadronization of quarks, because at that scale the coupling constant for the force is too large (~ 1) for calculations to be made perturbatively. We must resort to phenomenological models to predict that.

This thesis represents an attempt to gain some insight into this process of hadronization by studying K^0 and Λ. The K^0 and the Λ are two distinctive particles produced in hadronization, being the lightest neutral meson and baryon containing a strange quark. They provide a window to study how quarks and antiquarks appear from the vacuum to combine into hadrons. Unlike many other particles, they can be easily identified over a large momentum range in quantities copious enough to admit study. In this thesis, production of K^0 and Λ will be studied at two different center-of-mass energies using the Mark II detector, and key distributions will be compared with hadronization models.

The remainder of this chapter will give an introduction to the Standard Model and to the mechanics of e^+e^- collisions. Chapter 2 delves more deeply into the theory of strong interactions and our models of hadronization. The apparatus used for this study is described in Chapter 3. The description of the analysis begins in Chapter 4 with the criteria used to isolate the desired signal. Chapter 5 discusses the backgrounds and errors for this measurement. The results of the measurement

are described in Chapter 6, and the seventh chapter concludes the thesis with a summary discussion of these results.

1.1 The Standard Model

The Standard Model describes nature as four basic forces acting upon particles of matter. The smallest known units which make up matter are spin-$\frac{1}{2}$ particles known as *fermions*. The forces are gravity, electromagnetism, the weak force, and the strong force. The forces are "carried" or mediated by particles with integral spin, known as *bosons*. On the quantum level, an interaction between a force and a fermion consists of the fermion emitting or absorbing the appropriate boson, as shown schematically in Figure 1. The size of the coupling constants between the bosons and the fermions determine the respective strengths of the forces. These coupling constants can be pictured as the probability of emission or absorption of each boson.

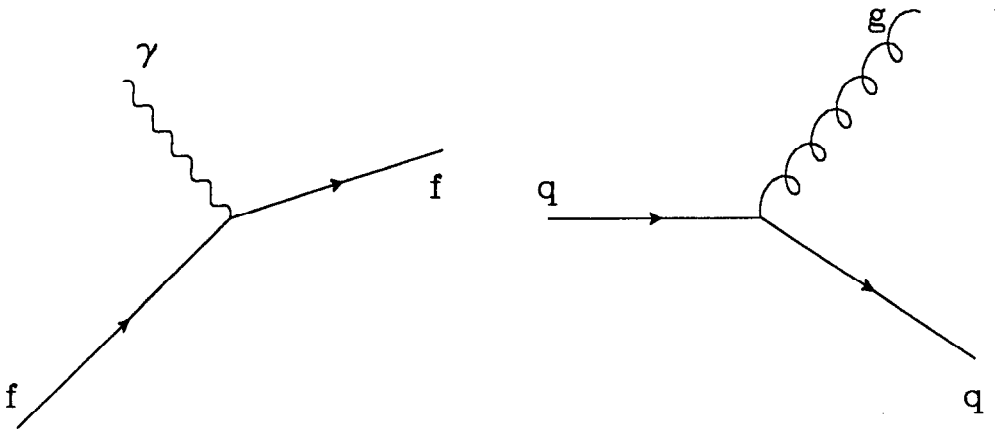

FIGURE 1. Feynman diagrams of the basic interaction of a force with a fermion, consisting of the fermion emitting or absorbing the force-carrying boson. The first diagram shows a fermion absorbing a photon, the second shows a quark emitting a gluon.

Some of these force-carrying bosons have mass. The mass helps to

determine the range of the force, in keeping with the Yukawa potential:

$$V(r) = \frac{1}{r} e^{-\frac{mcr}{\hbar}}.$$

The forces are listed in Table 1 with their ranges, strengths, and mediating bosons. Gravity, which seems to us the strongest force, is actually the weakest. Since its range is infinite and it has no opposite charge to neutralize it, its effects are most observable. It is not integrated into the Standard Model, but is listed here for completeness.

TABLE 1. The four forces are listed together with their ranges, strengths, and mediating bosons. The strengths are given relative to the strong force, for two up quarks separated by 10^{-18} m.

Force	Range	Strength	Mediating Boson
strong	10^{-16} m	1	gluon (0 mass)
electromagnetic	∞	0.04	γ (0 mass)
weak	10^{-18} m	0.032	$W^{\pm}$ (82 GeV) Z^0 (91.17 GeV)[6]
gravity	∞	10^{-43}	graviton (0 mass)

The other three forces have all been unified within the Standard Model. The forces can be represented by their symmetry groups: the transformations under which they are unchanged. In the language of symmetry groups, the Standard Model is $SU(3)_{color} \times SU(2)_L \times U(1)_Y$.

The matter upon which these forces act is made up of fermions. These particles of matter fall into two classes: quarks and leptons. The quarks and leptons are in turn grouped into three generations, with each generation a duplicate of the preceding generation except for higher mass. Table 2 shows the generations of quarks and leptons currently known. There is no known reason for the number of

TABLE 2. The fundamental fermions are grouped according to their generation. Masses given for the quarks are the constituent quark masses, and are only approximate.

Generation	1	2	3	Charge
Quarks (mass)	up (u) (330 MeV/c^2)	charm (c) (1.5 GeV/c^2)	top (t) (?)	$+\frac{2}{3}$
	down (d) (330 MeV/c^2)	strange (s) (500 MeV/c^2)	bottom (b) (5 GeV/c^2)	$-\frac{1}{3}$
Leptons (mass)	electron (e) (0.51 MeV/c^2)	muon (μ) (106 MeV/c^2)	tau (τ) (1.8 GeV/c^2)	-1
	ν_e (< 46 eV/c^2)	ν_μ (< 0.25 MeV/c^2)	ν_τ (< 35 MeV/c^2)	0

generations to be three, but searches for higher mass generations have so far found nothing.[7]

The heavier generations are unstable and decay through the weak force into lighter generations. Only the lowest lying generation is stable. Thus, most of matter as we know it is made up of the first generation: combinations of up and down quarks form the protons and neutrons which make up the atomic nucleus, and electrons orbiting these nuclei complete the atom.

For each particle type there exists an antiparticle. These antiparticles have the same mass as the particle but opposite quantum numbers. Any particle interaction can be made into the corresponding antiparticle interaction by reversing all quantum numbers (substituting antiparticles for all particles, and vice versa). Therefore, the lifetimes and decay modes for the antiparticles are the same as those

for the particle. A particle and its antiparticle can annihilate each other to make energy in the form of a photon or Z^0 boson.

Most of the leptons listed in Table 2 have been directly observed, but quarks have not. The theory of the inter-quark force, the strong force, predicts that single quarks cannot exist alone: they can only appear paired with an antiquark to form a type of particle called a *meson*, or with two other quarks to form a type of particle called a *baryon*. The most common baryons are protons, consisting of two up quarks and one down quark, and neutrons, consisting of one up and two down quarks. The most common mesons are pions, made up of an up or down quark combined with an up or down antiquark. Both mesons and baryons are grouped into a larger class known as *hadrons*.

The electromagnetic and weak forces interact with both quarks and leptons. The electromagnetic force is carried by the photon, a spin-1 boson which couples to charge. The weak force is carried by three particles: the W^+, W^-, and Z^0 bosons. These are also spin-1 particles; they couple to weak charge. The weak force is the only force which couples to neutrinos; it only couples to left-handed fermions or right-handed anti-fermions.

The weak and electromagnetic forces have been unified into a single electroweak theory, which states that at very high energies the two are the same force. For the electroweak force, the symmetry group is $SU(2)_L \times U(1)_Y$. The photon and the Z^0 boson are both combinations of the conserved currents of this symmetry group. The symmetry among these forces is broken at low energy scales by the Higgs mechanism, whereby the W and Z bosons absorb other fields to become massive.

Unlike the electroweak forces, The strong force only acts between quarks. Its symmetry group is $SU(3)$. It is carried by gluons, which couple to the color charge of quarks. There are three colors: red, blue, and green. Antiquarks carry anticolor: anti-red, anti-blue, and anti-green, also known as cyan, yellow, and magenta. Gluons carry both color and anticolor. Three colors and three anti-

colors would seem to indicate nine possible varieties of gluon, but actually the $B\bar{B} + R\bar{R} + G\bar{G}$ state is an SU(3) color singlet and therefore completely colorless; it cannot couple with anything else. This leaves eight gluons to carry the strong force.

The strong force is neutralized on a large scale by combinations of color charge which produce a net colorless state, analogous to the positively charged proton and negatively charged electron combining to make an electrically neutral atom. There are three ways to achieve these colorless states: a combination of all three colors giving white, the color neutral state; a combination of all three anticolors, or a combination of a color and its anticolor. Thus the bound states of the strong force are three quarks, three antiquarks, or a quark plus an antiquark: baryons, antibaryons, and mesons.

Quarks have never been observed outside of these bound states, for an interesting reason. Gluons carry three different color charges and couple to themselves. Therefore, an isolated color charge generates a cloud of gluons about itself which polarizes in such a way that the apparent color charge increases with distance. Thus the color force increases with distance. In the bound states of quarks, the distances are small and the color force is not great, so that quarks can move around much as if they were free particles. This phenomenon is known as asymptotic freedom. However, quarks can never be seen as free particles owing to the gluon self-couplings; the forces increase too much with distance to allow them to appear outside of bound states. This leads to the phenomenon known as hadronization in high energy collision experiments.

1.2 High Energy e^+e^- Interactions

Since early in the study of particle physics, accelerators have been used to increase the particle energy available for study. At first the accelerated particles were collided with fixed targets, but early in the 1970s scientists began to build accelerators which accelerated two bunches of particles in opposite directions and

collided them together, thus increasing the center-of-mass energy and allowing experimenters to observe interactions in the center-of-mass frame. At SLAC, the first such collider was the SPEAR e^+e^- storage ring, built to study 3 to 6 GeV interactions. It has been followed at SLAC by the PEP storage ring at 29 GeV and the SLC at the Z^0 resonance, both also e^+e^- colliders.

The reaction basic to e^+e^- colliders consists of an electron from one beam and a positron from the other annihilating to create a virtual photon or Z^0 boson with virtual mass equal to the collision energy. This photon or Z^0 boson quickly decays into a fermion-antifermion pair which is energetically available (*i.e.*, the mass of the fermion must be less than half of the mass of the virtual particle). Figure 2 shows the Feynman diagram for this process. The virtual photon can decay into charged leptons or quarks; the Z^0 boson can also decay into neutrinos.

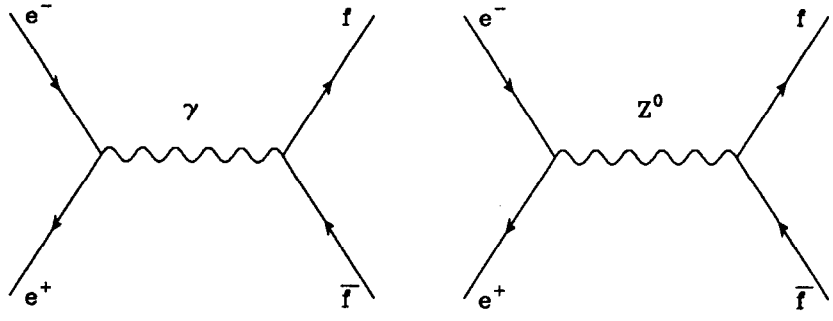

FIGURE 2. Feynman diagram for fermion production in e^+e^- collisions. For fermion production through a photon, any charged fermion can be the product; for the Z^0, neutrinos can also be produced.

There are three terms in the differential cross section for this process, a pure QED term (the photon diagram alone), a pure weak term (the Z^0 diagram alone) and a term for the interference between the two diagrams. The pure QED

term is

$$\frac{d\sigma}{d\cos\theta} = \frac{\pi\alpha^2 Q_f^2 C_f}{2s}(1+\cos^2\theta)$$

where Q_f is the fermion charge, C_f is a color factor which is one for leptons and three for quarks, θ is the production angle of the fermions with respect to the e^+e^- pair, α is the electromagnetic coupling constant, and $s = E_{cm}^2$. The pure weak term is

$$\frac{d\sigma}{d\cos\theta} = \frac{C_f G_f^2 M_Z^4 s}{64\pi[(s-M_Z^2)^2 + M_Z^2\Gamma_Z^2]} \times [(R_e^2+L_e^2)(R_f^2+L_f^2)(1+\cos^2\theta) + 2(R_e^2-L_e^2)(R_f^2+L_f^2)\cos\theta].$$

Here Γ_Z is the width of the Z^0, G_f is the Fermi constant, and R_f and L_f are the couplings of the fermion to the right and left handed components of the Z^0.

$$R_f = 2[(T_3)_{f_R} - Q_f \sin^2\theta_W]$$

$$L_f = 2[(T_3)_{f_L} - Q_f \sin^2\theta_W]$$

$(T_3)_{f_R}$ and $(T_3)_{f_L}$ are the right and left handed third components of weak isospin, and θ_W is the Weinberg angle. The interference term between the QED process and the weak process is given by:

$$\frac{d\sigma}{d\cos\theta} = -\frac{C_f \alpha Q_f G_f M_Z^2 (s-M_z^2)}{8\sqrt{2}[(s-M_Z^2)^2 + M_Z^2 G_Z^2]} \times [(R_e+L_e)(R_f+L_f)(1+\cos^2\theta) + 2(R_e-L_e)(R_f-L_f)\cos\theta].$$

These terms must all be included in calculations of particle production in e^+e^- colliders.

Energy and momentum are conserved in these reactions, so that if the fermion-antifermion pair are much lighter than the collision energy, they fly apart with considerable momentum and can then be observed in the detector.

1.3 $q\bar{q}$ Production in e^+e^- Colliders

If the fermion-antifermion pair are quark and antiquark, the fact that they must fly apart with equal and opposite momentum produces a problem, because quarks and antiquarks cannot exist singly. The color field between them increases in strength as they move apart, decelerating them. In order to conserve energy, other quark-antiquark pairs are spontaneously generated out of the vacuum and combine with the original pair and each other to form hadrons in such a way that energy and momentum are conserved. Thus, when a quark-antiquark pair are generated in a collider, what appears in the detector are showers of hadrons.

This process is called hadronization or, alternatively, fragmentation. It remains one of the less well understood aspects of Standard Model physics. To see why this is so, we must look more closely at the theory of the strong force: Quantum Chromodynamics, or QCD, the subject of the next chapter. The next chapter will also explore the models of hadronization which have been generated in the absence of theoretical calculations. The major portion of the thesis which follows will investigate one particular aspect of hadronization: the production of K^0 and Λ, which are the lowest lying mesons and baryons containing strange quarks.

1.4 The K^0 and Λ

The K^0 is the lightest neutral meson containing a strange quark; the Λ is the lightest neutral strange baryon. Because these two particles contain strange quarks, they are heavier than matter containing only up and down quarks. The K^0 has a mass of about 0.4977 GeV/c^2; the Λ mass is 1.1156 GeV/c^2. These masses are respectively about 350 MeV higher than the pion mass and 180 MeV higher than the proton mass. These mass differences are small on the scale of the center-of-mass energies of the collisions studied in this thesis; however, since hadronization, as will be seen in the following chapters, occurs at a smaller energy scale, the mass difference between the strange and the up and down quarks or the strange and the non-strange hadrons becomes important. The K^0 and the Λ should show effects of

the energy scale of hadronization, and are therefore a good test of hadronization models. Also, the K^0 and Λ can be found over a wide range in momentum, which allows a glimpse into the whole spectrum of hadron production.

A K^0 is made of a strange quark and an anti-down quark, $s\bar{d}$, combined with spins opposite to give a pseudoscalar particle. Its antiparticle, the $\bar{K}^0$, is composed of $d\bar{s}$. However, neither the K^0 nor the $\bar{K}^0$ exist in their pure state in nature, because they are not eigenstates of CP. Instead, the particles which appear in nature are combinations of K^0 and $\bar{K}^0$: the K^0_S, with composition $\frac{1}{\sqrt{2}}(s\bar{d} + d\bar{s})$, which is CP even, and the K^0_L, with composition $\frac{1}{\sqrt{2}}(s\bar{d} - d\bar{s})$, which is CP odd. These composite states are labelled with a subscript S and L because of their different lifetimes. The K^0_S decays predominantly into two pions relatively quickly. The K^0_L decays mostly into three pions, which owing to limited phase space takes much longer. Only K^0_S can be found in this analysis, but results for K^0_S will be generalized to include the K^0_L. The term K^0 here includes both the K^0_S and the K^0_L.

The Λ is composed of sdu, or $\bar{s}\bar{d}\bar{u}$ for the $\bar{\Lambda}$, arranged in an isospin singlet with spin $\frac{1}{2}$. Because the particle and antiparticle have opposite quantum numbers, they should behave as mirror images of each other. For the purposes of this thesis, the Λ and $\bar{\Lambda}$ are treated the same; they will both be referred to as Λ unless otherwise stated.

CHAPTER 2

QUANTUM CHROMODYNAMICS AND HADRONIZATION MODELS

Quantum Chromodynamics is the basic theory of the strong force. It is analogous to the quantum theory of electromagnetism, QED. In QCD, basic interactions are pictured as the emission by a quark of a field quanta, the gluon, followed by the interaction of that quanta with other quarks or gluons. The strength of the particular interaction can be calculated according to formal rules by assigning coupling terms to the points of emission and reabsorption and a propagator term for the boson exchanged.

However, no interaction consists of merely a single boson exchange; it is actually an infinite sum of possibilities, where the exchange gluon can couple to quark loops, or extra gluons can be emitted and reabsorbed, as shown by the Feynman diagrams in Figure 3.

Some of these loops make the calculation diverge logarithmically. However, this logarithmic divergence is removed by a process called renormalization, which reparametrizes the bare coupling constant represented by the vertex in Figure 3a to be the "measured" coupling constant. Measurement of the coupling constant includes all of the loops, so the final result of the sum is known, and by calculating the diagram in Figure 3a with the measured coupling constant, we have taken all loops into account. This is equivalent to stripping the vertex diagram of loops.

Because of the renormalization, the coupling constant α_s depends on the energy at which it is measured; all coupling constants at any energy are referred to a base value measured at some arbitrary energy. To first order, the dependence of α_s on the energy of the interaction is given by:

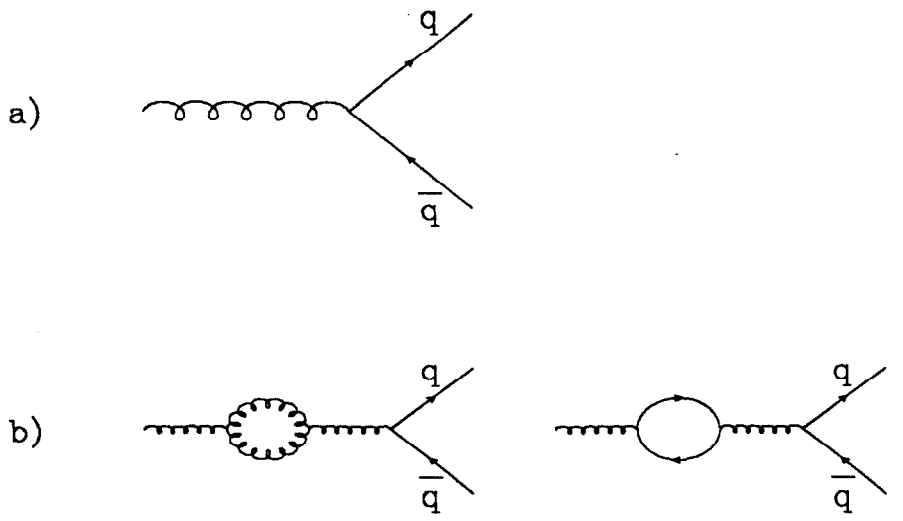

FIGURE 3. The Feynman diagrams of the corrections to second order of the quark gluon vertex.

$$\alpha_s(Q^2) = \frac{\alpha_s(\mu^2)}{(1 + \frac{\alpha_s(\mu^2)}{12\pi}(33 - 2n_f)\ln(\frac{Q^2}{\mu^2})}$$

where Q^2 is the momentum transfer for which α_s is being calculated, n_f is the number of quark flavors, and μ^2 is the arbitrary value of the momentum transfer chosen for renormalization. For a number of flavors less than or equal to 16, α_s (Q^2) becomes large for small enough Q^2; the dependence on number of flavors occurs because each quark flavor introduces another possible set of loop diagrams to the correction of the bare vertex. Presently five flavors are known and a sixth is believed to exist, but no evidence has been found for more, so α_s should become large at low momentum transfers. It is customary to choose the energy scale at which α_s becomes infinite as the renormalization scale, denoting it as Λ^2. Then the equations simplify to

$$\alpha_s(Q^2) = \frac{12\pi}{(33 - n_f)\ln(\frac{Q^2}{\Lambda^2})}$$

at first order, and at second order to

$$\alpha_s(Q^2) = \frac{12\pi}{b_0 \ln(\frac{Q^2}{\Lambda^2}) + \frac{b_1}{b_0} \ln(\ln(\frac{Q^2}{\Lambda^2})}$$

where $b_0 = 33 - 2n_f$ and $b_1 = 918 - 114n_f$. The precise value of Λ depends on the method by which renormalization is done. One widely used scheme is the modified Minimal Subtraction scheme; when this is used, the energy for infinite α_s is denoted by $\Lambda_{\overline{MS}}$. When a leading logarithm scheme is used, it is denoted by Λ_{LLA}.

For a number of quark flavors of 16 or less, the coefficient of the $\ln(\frac{Q^2}{\Lambda^2})$ term is positive, which means that as Q^2 increases α_s will decrease. This phenomenon is known as the "running" of the coupling constant. The value of α_s can vary between infinity and zero.

2.1 Perturbative QCD

Renormalization has removed the infinities due to vertex loops from QCD calculations. However, other problems remain: to make exact calculations, all possible diagrams other than the vertex loops must be added together. Figure 4 shows some of the contributions to $e^+e^- \rightarrow q\bar{q}$ production. Many more can be made by adding further loops and gluon emission lines. Each vertex between quarks and gluons or gluons and gluons contributes a factor of $\sqrt{\alpha_s}$. Owing to this, the magnitudes of the contributions of different diagrams can be grouped according to powers of α_s , as shown in the figure.

When α_s is small compared to 1 ($O \sim 0.1$), terms of high order in α_s can be ignored; QCD can be calculated perturbatively in this regime, although calculations of specific final states may suffer from infrared divergences. There are two common perturbative QCD calculations of parton production in e^+e^- collisions: the exact second order matrix element calculation, which uses the diagrams shown in Figure 4, and the leading logarithm approximation.

The leading logarithm approximation regularizes the matrix element at each branching in the parton shower by giving mass to the gluon and summing up

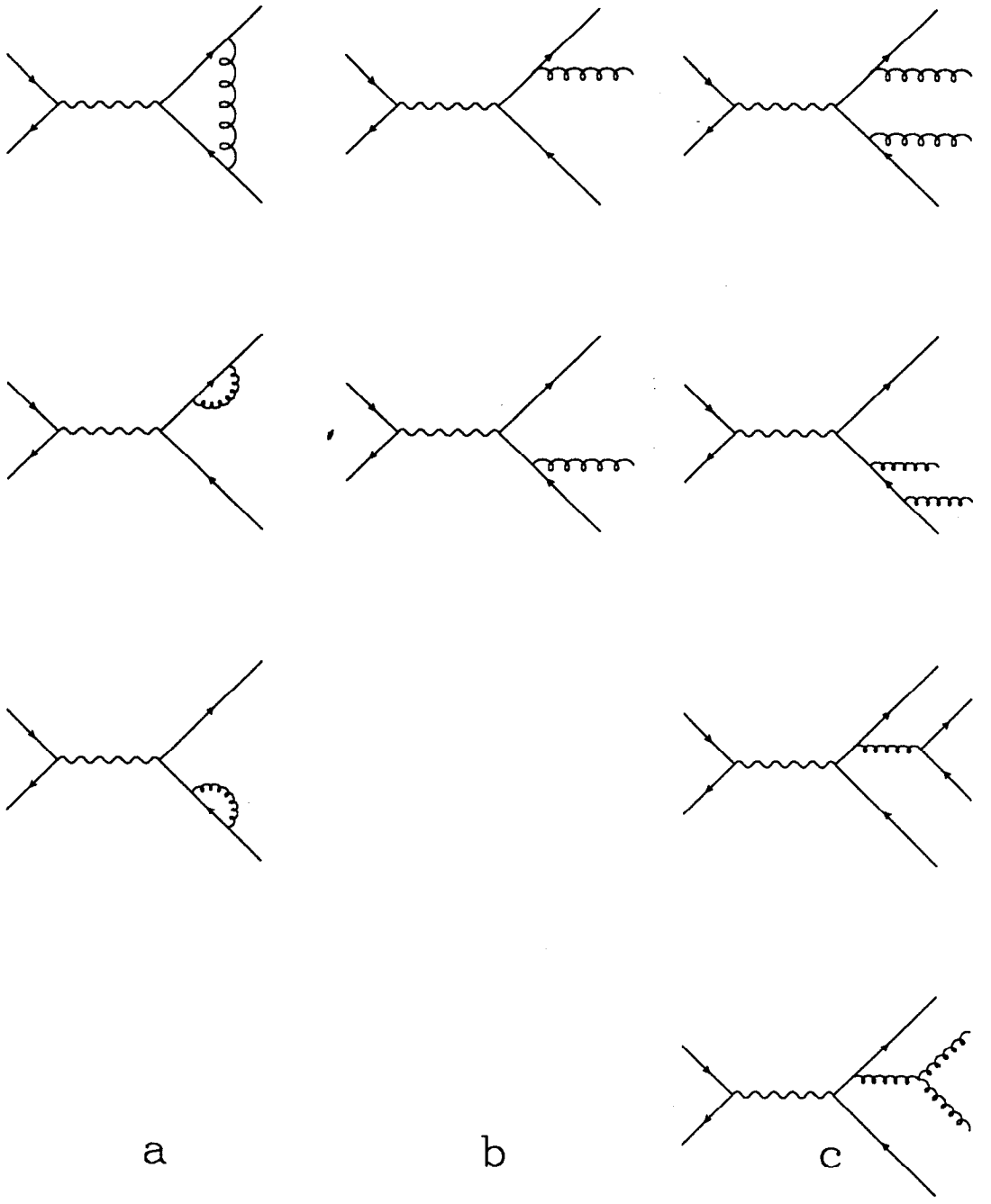

FIGURE 4. Feynman diagrams for some of the contributions to second order calculations of parton generation. The first column shows the diagrams for second order calculations of $q\bar{q}$ production, the second the first order diagrams for $q\bar{q}g$ production, and the third diagrams for $q\bar{q}gg$ production.

the leading logarithmic contributions. At each branching the partons become less virtual until they reach a cutoff mass Q_0, at which point the showering stops and the calculation is considered complete.

2.2 Non-Perturbative Regime of QCD

However, as the energy of interactions decreases (the distance scale of the interaction increases) α_s becomes greater than one, and perturbative calculations can no longer be done. The strength of interactions between quarks and gluons or gluons and gluons becomes quite large. This leads to the phenomenon called confinement, which was mentioned previously: quarks cannot be observed outside of hadrons. When quarks are produced in high energy interactions they quickly pull quark-antiquark pairs out of the vacuum to "dress" themselves as hadrons.

In e^+e^- annihilation, a produced quark-antiquark pair fly apart from each other. The gluons radiated from each, instead of forming a spherical cloud, are drawn together by their self-interactions to form a color tube between the pair. The force exerted by the tube grows stronger with the length of the tube; it can be approximated by

$$F \propto kr.$$

The longer this tube of force becomes, the higher grows its energy, until eventually the production of new particles is energetically favored. Quarks and antiquarks appear out of the vacuum and combine with the original pair to give hadron showers.

We have no way of calculating how this process takes place; the energies at which quarks combine into hadrons are in the non-perturbative regime of QCD. Instead, we must use models which attempt to explain experimental phenomena.

2.3 Models of Fragmentation

Fragmentation models use basic assumptions about the nature of the fragmentation process to calculate its phenomenology. The assumptions are put into Monte Carlo programs which generate fake hadronic events which can be compared to real data.

One of the earliest fragmentation models was the Independent Fragmentation model by Feynman and Field.[8] In this model, the two primary quarks fragment independently of each other, pulling a $q\bar{q}$ pair out of the vacuum and combining with one of them to form a meson. The pair is pulled from the vacuum with some of the original quark's momentum, so the remaining quark is left with momentum after the meson is formed. This remaining quark then pulls another $q\bar{q}$ pair from the vacuum and combines with one of them. The process iterates until the remaining quark on one side has little energy, whereupon it combines with the remaining antiquark from the other side. Each quark in the chain is treated exactly like the first quark, as if the other quarks already produced have no effect on it.

The meson produced by this method from the original quark and the antiquark from the vacuum pair is given a fraction of the original quark momentum according to a fragmentation function $D(z)dz$ giving the probability that the meson has momentum fraction between z and $z + dz$. The momentum fraction z is

$$z = \frac{(E + P_{\|})_{meson}}{(E + P_{\|})_{quark}},$$

where $P_{\|}$ is the momentum along the primary quark direction. The denominator represents the original energy and momentum of the quark and the numerator the energy and momentum of the meson of which it becomes part. These fragmentation functions can be varied to fit the data; a commonly used form for light quarks is

$$D(z) \propto (1 - z)^r,$$

where r is a parameter chosen to match the data.

In order to incorporate hard radiated gluons in the model, such gluons are treated either as another quark or as a $q\bar{q}$ pair and are also allowed to fragment independently. If the gluon is treated as a $q\bar{q}$ pair, the gluon energy is split between them according to the Altarelli-Parisi equation.[9]

This model has failed to predict some effects seen in hadronic events. For instance, it does not display the observed depletion of particles in the region opposite the third jet of three-jet events.[11] Because it does not agree well with the data, it has largely given place to two more recent types of models: string models and cluster models.

2.3.1 String Models

String models take their inspiration partly from the $F \propto kr$ nature of the force between quarks. The quark and antiquark are pictured as the endpoints of a string, which gains energy as they move apart. The string constant is approximately $k \approx 1$ GeV/fm. Eventually the creation of a quark-antiquark pair is energetically favored and the string breaks, creating two strings with four endpoints. This process continues until all fragments have too little energy for $q\bar{q}$ production, and thus become hadrons. A conceptual picture of this process is shown in Figure 5. The end products may be unstable hadrons, which will decay into stable particles. Although this process is supposed to take place from the low momentum regions to the high,[10] (the inside out) it is calculationally equivalent to going from the high momentum regions to the low (the outside in). As a result of this process, the produced hadrons come out roughly aligned along the original $q\bar{q}$ direction, albeit with some transverse momentum.

The produced mesons take a fraction of the original quark momentum as in the Field-Feynman model. Again, this is done by means of a probability function in z known as the fragmentation function. These fragmentation functions are again somewhat arbitrary, chosen to fit the data.

The transverse momentum is acquired in the quantum mechanical

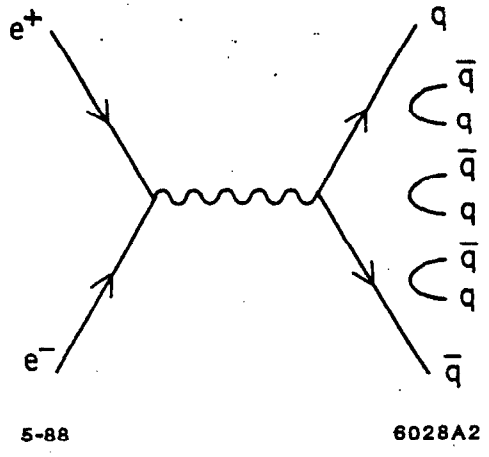

FIGURE 5. A conceptual view of string fragmentation.

tunneling of the $q\bar{q}$ pair from the vacuum. The creation of a $q\bar{q}$ pair demands a hole in the color field of length l where

$$kl = E_\perp = \sqrt{M^2 + P_\perp^2}.$$

The creation probability is therefore

$$\exp \frac{-E_\perp^2}{2\sigma_\perp^2}.$$

This gives a distribution Gaussian in $p_\perp$.

This creation probability also gives mass suppression through the M^2 term in $E_\perp$. This is a natural mechanism for the suppression of heavy flavors. Unfortunately, since the quark masses are needed, and their values are not well known, this mechanism cannot be tested exactly. The suppression of heavy quark flavors remains a free parameter of the theory, although general predictions such as suppression of charm compared to strange must still hold.

The transverse energy Gaussian also allows for suppression of baryons in fragmentation. Originally, fragmentation models did not allow baryon production,

until experiments showed that baryons were indeed produced in quark jets.[12] Then models allowed for it by letting $qq - \bar{q}\bar{q}$ pairs, known as *diquarks*, appear from the vacuum. A diquark obviously has larger mass than a quark; thus diquarks are suppressed by the $E_\perp$ term. As with quarks, the masses of diquarks are not well known. Although the model explains baryon production, the suppression of baryons is essentially a free parameter of the model.

Emission of gluons is taken into account by making gluons into kinks in the string. The gluon kink gives the center of the string transverse momentum, while the ends of the string pick up opposite momentum. Since the string itself carries momentum, this pulls the whole string to one side and accounts for the depletion of particles on the side of the event away from the gluon jet.

2.4 The Lund Model

The present most popular string model is the Lund model, implemented in the JETSET 6.3 Monte Carlo.[14] It is based on a semi-classical treatment of the string-like force field. In the Lund model, $q\bar{q}$ pairs are formed in the color field in such a manner that energy, momentum and internal quantum numbers are conserved. All $q\bar{q}$ production points are causally disconnected. If a pair $q_1\bar{q}_1$ is produced at (x_1, t_1), and another pair $q_2\bar{q}_2$ is produced at (x_2, t_2), $\bar{q}_1$ and q_2 can combine to produce a hadron with energy $E_1 = k(x_2 - x_1)$ and momentum $p_1 = k(t_2 - t_1)$ (k is the string constant). Therefore, the hadron can exist only if

$$(x_2 - x_1)^2 - (t_2 - t_1)^2 = \frac{m^2}{k^2}.$$

In other words, the hadron must be produced on a hyperbola of mass-shell states.

These produced hadrons have a fraction of the original quark momentum assigned by a fragmentation function in z. The "simple Lund" model uses

$$D_q^h(z) = f_q^h(z) + \int_z^1 \frac{dz'}{z'} f_q^{qq'}(1 - z') D_{q'}^h(\frac{z}{z'})$$

$$f(z) = (1 + c)(1 - z)^c$$

where $D_q^h(z)$ is the probability to find a hadron h in a quark jet q, $f(z)$ is the probability to find a hadron containing the original quark at momentum fraction z, and the integral term reflects the probability that the remnant jet will produce a hadron at z. As before, z represents the fraction of $(E + p_\parallel)$ carried by the hadron.

A more sophisticated version of the Lund model is "symmetric Lund," which gives left-right symmetric jets. Unlike in simple Lund, the properties of the particles in the jet do not depend upon the end at which fragmentation starts. The fragmentation function for a quark with flavor α to combine with an antiquark of flavor β to give a meson with transverse mass $m_\perp$ and energy momentum fraction z becomes

$$f_{\alpha\beta}(z) = N_{\alpha\beta}\frac{1}{z}z^{a_\alpha}(\frac{1-z}{z})^{a_\beta}\exp(-\frac{bm_\perp^2}{z}).$$

where a_α and a_β are tunable parameters.

Massive quarks produced from the vacuum are treated as appearing a distance $2l$ apart so that the field energy between them can be used to create the mass:

$$2kl = 2\mu$$

where μ is the quark mass. If this is treated as quantum mechanical tunneling, the probability is

$$d^2p_\perp \exp(-\frac{\pi\mu_\perp^2}{k}).$$

$$\mu_\perp = \sqrt{\mu^2 + p_\perp^2}$$

This gives, for $k \approx 1$ GeV/fm, suppression of heavier quarks in the approximate ratio

$$u : d : s : c \approx 1 : 1 : \frac{1}{3} : 10^{-11}$$

Therefore, fragmentation production of charm should be virtually nonexistent.

Diquarks in the Lund model are treated as a unit. The density of quarks in the vacuum state is considered high enough that the probability to form a diquark in the vacuum is essentially one. This means that the production probability for diquarks is governed only by the mass term above. Therefore, baryons should have a Gaussian $p_\perp$ spectrum, as the mesons do. They should also be produced evenly in rapidity. Baryons and antibaryons are produced next to each other in rank (the rank is the order of the particle in the string breaking). As a consequence, they should show strong momentum correlations. Also, for all $\mu > \sqrt{\frac{k}{\pi}} \simeq 250$ MeV a small change in μ should give a large change in probability; strange diquarks therefore should be uncommon.

Radiated gluons, as mentioned previously, are treated as kinks in the color string. The string is broken on either side of the kink in such a way that the resultant hadron has a correct physical mass. The fact that the hadron contains the kink does not matter. After the production of this leading hadron, all that remains is straight string pieces on either side, which fragment in the usual manner. Owing to the fact that the formation of the leading hadron in the gluon jet involves a double breaking of the string, giving twice the probability of pulling a diquark from the vacuum, the fraction of high-z baryons should be somewhat higher in the gluon jet than in the quark jets.

Soft gluons are treated by summing their momentum in a rapidity bin to give an effective gluon with finite $p_\perp$. This gives a small bump in the color flux tube. This $p_\perp$ is then shared by the hadrons produced in that rapidity bin, and the rest of the fragmenting particles pick up some recoil momentum. This has the effect of increasing the $p_\perp$ of events from that given by the Gaussian $p_\perp$ distribution.

2.4.1 The JETSET 6.3 Monte Carlo

The JETSET 6.3 Monte Carlo uses the Lund fragmentation described above. It generates the the primary quarks and radiated gluons to be used in fragmentation by two methods. One uses the $O(\alpha_s^2)$ matrix element calculation made by Gottschalk and Schatz.[13] The parameter Λ used to define α_s is denoted by $\Lambda_{\overline{MS}}$. These calculations give at most four partons in an event. Also, no partons can be generated with invariant mass less than some cutoff value; this is done to prevent soft gluon divergences. This method cannot be used with the same parameters at both 29 GEV and 91 GeV; therefore it is not used in this thesis.

The other method implemented in JETSET 6.3 does parton shower generation with a leading log approximation. Here Λ is defined as Λ_{LLA}. This approximation can be used at both 29 GEV and 91 GeV with the same parameters; it is the one used in this thesis. The parameters for the Lund Monte Carlo with leading log approximation are listed in Table 3. These are the values tuned by Mark II and TASSO.[15] [16]

TABLE 3. Parameters for the Lund Monte Carlo (JETSET 6.3) hadronization model are listed. Values were tuned independently by Mark II and TASSO. Only parameters for the shower version of the model are listed.

Parameter	Mark II value	TASSO value
Λ_{LLA} QCD scale	0.4	0.26
Q_0 cutoff for parton shower	1.0	1.0
a (fragmentation function)	0.45	0.18
b (fragmentation function)	0.9	0.34
$\sigma_\perp$ for $p_\perp$	0.23	0.39

2.5 The UCLA Model

Another variant of string models which is of interest is the UCLA model.[17] This model was inspired by the fact that the Lund symmetric fragmentation function

$$f(z) = N\frac{(1-z)^a}{z}e^{-bm^2/z}$$

where

$$m^2 = m^2_{hadron} + p^2_\perp$$

could be used to give the production density of hadrons in mass and $p_\perp$ as well as in z without the use of additional quantum tunneling terms and suppression factors. This could be done by making N a global constant instead of renormalizing the function for each particle species, and using the Clebsch-Gordon coefficients (CG_i) to couple the quarks into hadrons:

$$dP_n \sim \prod_{i=1}^{n} F_i(z_i, m_i, P^2_{Ti})CG^2_i$$

$$F_i(z_i, m_i, p^2_{Ti})dz_i dP^2_{Thad} = N\frac{(1-z)^a}{z}e^{-\frac{b}{z}(m^2_{had}+P^2_{Thad})}dz dP^2_{Thad}$$

where P_n is the probability for a given n-particle state. This method has the advantage of dispensing with many of the parameters of the Lund Monte Carlo, leaving the only tunable parameters as a and b. The predictions of particle populations achieved by this method agreed fairly well with the data, in spite of the reduction in parameters, except for some underestimation of baryon populations; however, the original UCLA model did not take popcorn diagrams into account, where "popcorn" means the production of $q\bar{q}$ pairs between the two halves of a diquark pair.

The current version of the UCLA model, derived from longitudinal phase space and a linear confining quark potential as expressed by the Wilson Area Law,[18]

arrives at the probability

$$dP^{(1)}(m_1, z_1) = \left[N_1 \frac{dz_1}{z_1}(1-z_1)^a e^{-bm_1^2/z_1}\right] \times (1 - \frac{m_1^2}{sz_1})^a,$$

together with the Clebsch-Gordon couplings, for the first particle formed in a chain of fragmentation. The term in square brackets duplicates the Lund fragmentation function. The following term introduces dependence on the center-of-mass energy of the event.

Presently, the P_T of a produced hadron is compensated by the next two hadrons in the iterative series. Full treatment of P_T production is still being worked on.

Baryons produced from popcorn are taken into account by including all possible popcorn diagrams up to the average number of directly produced hadrons for any particular E_{CM}. In practice, this is done by using Clebsch-Gordon coefficients to couple each leading quark into the possibilities for the next hadron, weighted additionally by the possibilities of the three hadrons after it in the fragmentation series, in order to take into account neighboring popcorn diagrams. Higher order popcorn diagrams are taken into account by a correction factor.

The current UCLA model has very good agreement with particle multiplicities found in data in the region of 29 GeV, and also duplicates kinematic distributions well. Its kinematics are similar to those of the Lund model, since the form of the fragmentation function is the same. Differences between the kinematic predictions of the two models will be too small for the statistics of this measurement to differentiate between the two, but the overall multiplicity predictions are of interest.

Several variations of the UCLA model allow the factor a to be larger for baryons than for mesons. These will not be treated here. The parameters currently in use for the UCLA model are $a = 2.0$ and $b = 1.0$.

2.6 Cluster Models

The cluster models are an attempt to integrate QCD more closely into a fragmentation model. In the cluster models, perturbative QCD is used to generate a parton shower until the energies available to the showering process become low enough that perturbative methods begin to lose their validity. At this point, all quarks are combined into colorless clusters. These clusters then decay through phase space into the final state hadrons.

2.6.1 The Webber Model

The best known of the cluster models is the Webber Model.[19] In the Webber Model, parton showers are generated with the leading-logarithm approximation. At the perturbative level, jets exhibit a property called *preconfinement*.[20] Preconfinement means that generated partons tend to cluster in colored singlets. Webber assumes these clusters are the basic unit of hadronization. The mass scale is controlled by the infrared cut-off at which perturbative branching is terminated. This cut-off is somewhat arbitrary and is used as a free parameter in the theory, which is denoted by Q_0. When the value of Q_0 is set fairly low most clusters have masses below a few GeV. These clusters are then treated as resonances which decay via phase space.

In the perturbative phase of QCD jet development, the initial parton is far off mass-shell and emits gluons until all partons are near mass-shell. The distribution of energy and momentum for each splitting is given by the appropriate Altarelli-Parisi function.[9] Infrared interference leads to angular ordering: the successive opening angles in the branching process decrease. The angular variable is $\xi = \frac{q_j \cdot q_k}{\omega_j \omega_k}$ where q_i are the virtualities of the partons and ω_i are the energies. The net effect of angular ordering is suppression of soft gluon radiation.

The Monte Carlo takes a parton with energy E and initial angular variable $\xi \leq 1$ ($\theta \leq \frac{\pi}{2}$) and develops the cascade until the remaining energy is too low to continue. The cut-off is given by:

$$\xi_{min} = \frac{(Q_j + Q_k)^2}{\omega^2}$$

where Q_i represents the quark mass, for splitting into quarks, or Q_0 for splitting into gluons. Above this threshold the probability distribution in ξ is given by a Sudakov-type form factor. For any splitting, the largest possible value of the angular variable, ξ_{max}, is the ξ value for the previous branching.

After all branching is complete the parton masses are set at Q_j and the parton momenta are calculated from the energies, the ξ, and a random azimuthal orientation. Phase space constraints are not needed because angular ordering provides a constraint stronger than kinematics.

After all partons have branched down to the cutoff parameters, the gluons are split into $q\bar{q}$ pairs and all the quarks combine into color singlet clusters as shown in Figure 6.

The $g \rightarrow q\bar{q}$ probability distribution is

$$\xi = \frac{\bar{\Lambda}^2}{\omega^2}\left(\frac{\omega^2 \xi_{max}}{\bar{\Lambda}^2}\right)^{R^{6\pi b}}$$

where R is a random number between 0 and 1, and $\bar{\Lambda}$ is some constant times Λ. If $\bar{\Lambda} = 2m_0 = Q_0$ all gluons eventually decay into $q\bar{q}$ pairs when their energy comes close to the light quark threshold.

The resulting cluster mass is peaked at small values with a long tail. For those with mass M_c well above some critical threshold M_f the cluster splits into two smaller clusters via string fragmentation. If the cluster is formed of a (di)quark with momentum p_1^μ and an anti(di)quark with momentum p_2^μ, the process $C \rightarrow X + Y$ gives

$$p_X^\mu = (1 - \frac{Q_0}{M_c})p_1^\mu + \frac{Q_0}{M_c}p_2^\mu$$

and

$$p_Y^\mu = (1 - \frac{Q_0}{M_c})p_2^\mu + \frac{Q_0}{M_c}p_1^\mu.$$

The resulting clusters undergo quasi-two-body decay with branching

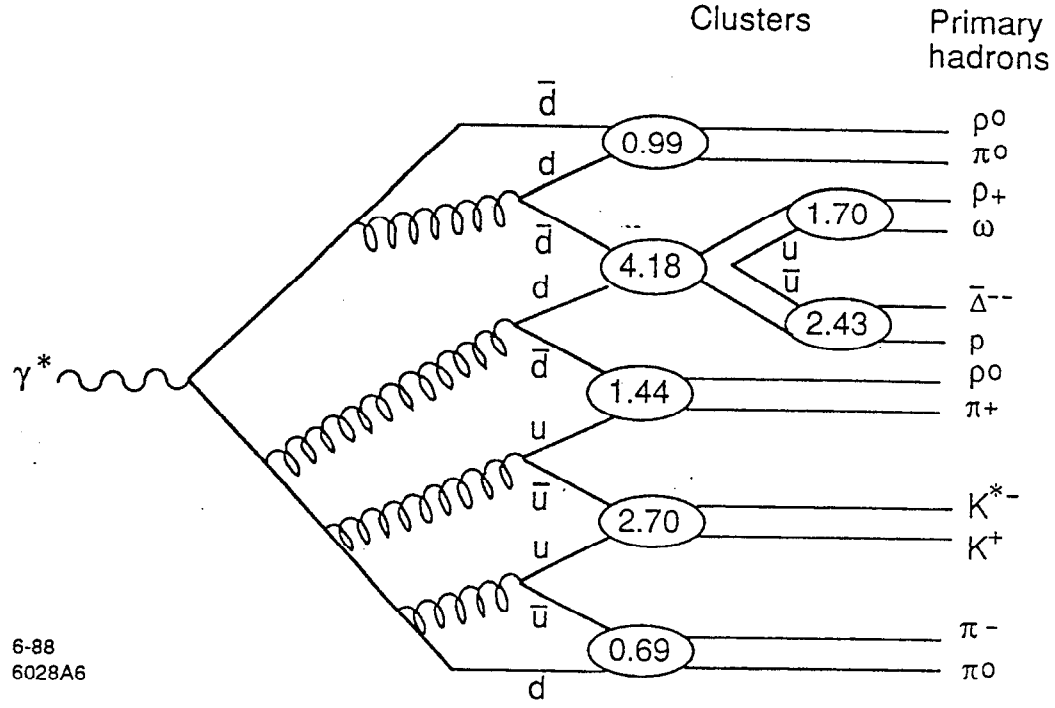

FIGURE 6. A conceptual picture of the cluster model of hadronization shows partons showering and then forming into colorless clusters.

ratios determined by the density of states, given by phase space times spin degeneracy. There are no spin correlations, so decay is isotropic. For a cluster made of $q_1\bar{q}_2$, another flavor is chosen at random from among the three light flavors in either a quark or diquark configuration. The decay products are then made of $q_1\bar{q}_3$ $(q_1 d_3)$ and $\bar{q}_2 q_3$ $(\bar{q}_2 \bar{d}_3)$. The decay products are selected from a list of resonances for those flavor combinations, weighted by the spin degeneracy $(2S+1)$ and tested for available phase space with a random number. If that combination fails, another flavor is chosen. The resonances are chosen among the 0^-, $1^\pm$, 2^+ $SU(3)$ octets of mesons and the $\frac{1}{2}^+$ octet and $\frac{1}{2}^+$ decuplet of baryons.

As the above description shows, strangeness and baryon suppression occur only through reduction of phase space. The transverse momentum of the decay products comes from the cluster decay and the original parton momenta.

The Monte Carlo formulation of the Webber model allows for extra suppression of strangeness and baryon production with extra parameters; however, this thesis uses the pure Webber model Monte Carlo with only three parameters. The values of the parameters used are shown in Table 4. For the Webber Monte Carlo as well as the Lund Monte Carlo, the parameters are kept the same at 29 GeV and 91 GeV for this analysis. These values are those tuned at 29 GeV and 35 GeV by Mark II and TASSO.[15] [16]

TABLE 4. The parameters for the Webber model as tuned for the BIGWIG 4.1 Monte Carlo by Mark II and TASSO are given.

Parameter	Mark II value	TASSO value
Λ_{LLA} QCD scale	0.20	0.25
Q_0 cutoff for parton shower	0.75	0.61
M_c cluster cutoff mass	3.0	2.3

CHAPTER 3

APPARATUS

The data discussed in this thesis were taken with the Mark II detector at two different colliders. The Mark II detector has had a long and varied history. In its first incarnation as the Mark I detector, it collected data at the SPEAR storage ring at SLAC, where it participated in the discovery of the J/Ψ.[22] Thereafter, it was moved to the PEP storage ring to take data at 29 GeV. When the Stanford Linear Collider (SLC) was proposed, the Mark II detector was upgraded so that it could be used in the SLC while the SLD detector was being built. In order to understand the upgraded detector, the Mark II collaboration continued to take data at PEP until 1986, when the detector was moved to the interaction region of the linear collider. It began to take data at the Z^0 resonance in April 1989. This thesis uses the data accumulated by the upgraded detector at PEP and the data from the first year of running at the Z^0 resonance.

3.1 The PEP Storage Ring

In the Positron Electron Project (PEP) storage ring, electrons and positrons rotate in opposite directions and collide at six interaction regions around the ring.[23] The layout of the PEP ring is shown in Figure 7.

The electrons and positrons circulate in three bunches, which are filled by the SLAC linear accelerator whenever the luminosity dips too low. Both positrons and electrons have an energy of 14.5 GeV. Thus, the center-of-mass energy is 29 GeV, and the CM frame and the lab frame are the same. Collisions between the bunches occurred every 2.4 μsec. This gave a maximum luminosity of about 3×10^{31} cm^{2}sec^{-1}. The beams were ellipsoidal at the interaction regions, measuring about 480 μm in x, 80 μm in y, and 1.5 cm in z. Changes in machine tuning moved

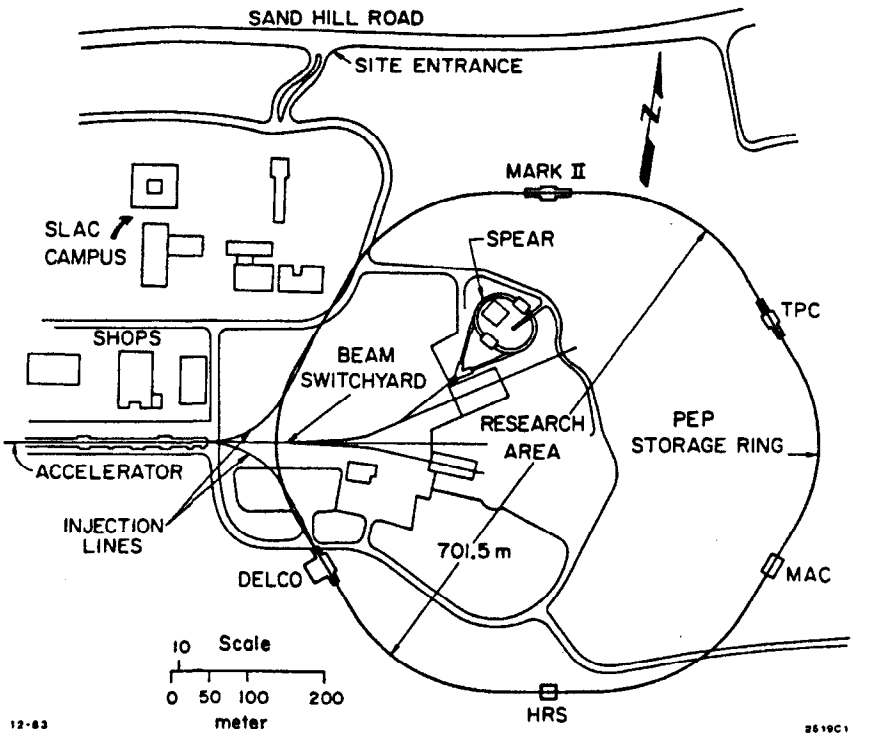

FIGURE 7. An overview of the SLAC site and PEP ring. There are six interaction regions around the ring.

the collision point, but significant movement seldom happened during a run, so that the interaction point for a run could be well defined. A total of 24.5 $pb^{-}1$ of data was accumulated with the upgraded Mark II detector at PEP.[24]

3.2 The Stanford Linear Collider

When SLAC decided to study Z^0 production, a new kind of colliding beam machine was built: the SLAC Linear Collider (SLC). Its layout is shown in Figure 8. It has been described extensively elsewhere.[25]

The SLC takes a beam of positrons from the LINAC into one arc and a beam of electrons into the other, and bends them to collide with each other at the interaction region. After the collision, both beams are extracted to dumps. Since the beams do not circulate repeatedly, energy loss due to synchrotron radiation

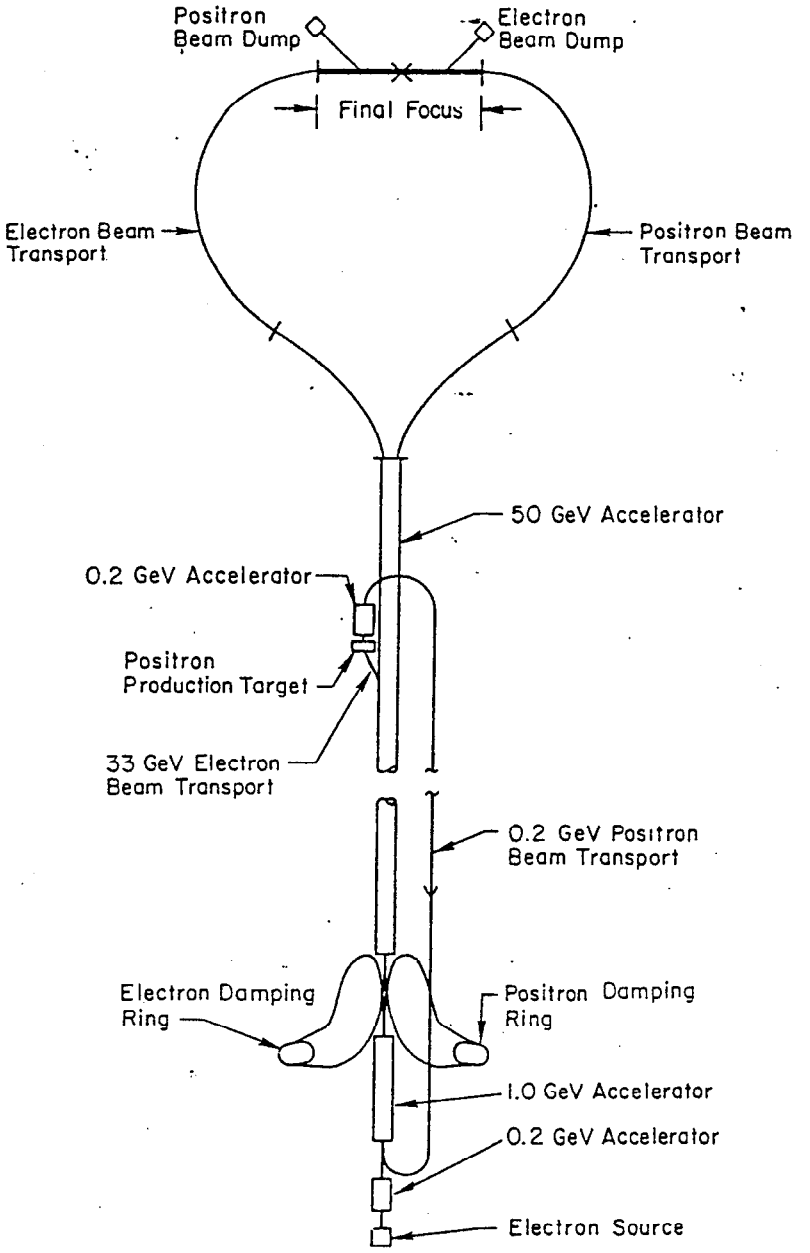

FIGURE 8. The layout of the SLAC Linear Collider.

does not matter, except that the beam energy has to be higher at the beginning of the arc than the desired energy at the interaction point.

The lack of stored beams makes many changes to standard accelerator technology necessary. Since the beams are not damped by circulating in a storage ring while colliding, they must be damped before injection. This occurs near the beginning of the linac in two storage rings known as the damping rings. Two

bunches circulate in the damping rings at an energy of $\simeq$ 1.2 GeV ; the damping time is 2.9 ms. A kicker extracts bunches and sends them down the Linac. Behind these, a high intensity electron beam is extracted to be sent to the positron target to generate more positrons. First a bunch of positrons is extracted, followed about 60 feet later by a bunch of electrons; both of these are injected into the arcs to collide at the interaction point.

Knowledge of the magnet strengths together with the tuning of a storage ring can be used to determine the energy of the stored beams. In a single pass collider, pulse-to-pulse energy is not necessarily stable, so another method of measuring energy must be found. At the SLC, this is accomplished with an energy spectrometer in the extraction line to each dump. These energy spectrometers measure positron and electron energy on a pulse-to-pulse basis with great accuracy. They will be described further later in this chapter.

The SLC beams are not constrained in size and position by a storage ring. One beam can move on a pulse-to-pulse basis without being tracked by the other. In order to monitor beam sizes and keep the beams in collision, the SLC uses the fact that the beams deflect each other as they cross at the IP.[26] Deflections are small when the beams are far apart, and largest when they are close but not overlapping. The deflections decrease as the beams become centered on each other and then increase in the opposite direction as they pass through. To center the beams, one beam is scanned across the other, and the deflections are measured with beam position monitors downstream; the beam is set to the position which gives zero deflection. The size of the deflections gives a measure of beam size. Beam size is also measured by scanning the beam across a small wire.[27]

The SLC ran at ten energies between 89.2 and 93.0 GeV while generating the data used in this thesis; the values are listed in Table 5.[28] For the purposes of this analysis, all energies are included and treated as the measured Z^0 mass; the differences are very small and hadronization properties should not change much over the range of energies. The statistics would have to be many orders of magnitude

TABLE 5. Energy scan points for the SLC.

Scan Point	$< E >$ (GeV)	Lum ($nb^{-}1$)	σ_Z (nb)
1	92.16	0.54 ± 0.05	$21.5^{+9.2}_{-6.6}$
2	90.74	1.21 ± 0.07	$31.7^{+6.8}_{-5.5}$
3	89.24	0.68 ± 0.05	$4.5^{+4.5}_{-2.5}$
4	91.50	1.23 ± 0.07	$34.3^{+7.0}_{-5.7}$
5	89.98	0.76 ± 0.05	$13.5^{+6.0}_{-4.3}$
6	92.96	1.00 ± 0.07	$14.6^{+5.4}_{-4.0}$
7	91.06	4.08 ± 0.12	$31.6^{+3.4}_{-3.1}$
8	91.43	4.12 ± 0.13	$29.8^{+3.3}_{-2.9}$
9	92.22	3.05 ± 0.11	$24.3^{+3.4}_{-3.0}$
10	90.35	0.76 ± 0.05	$13.5^{+6.0}_{-4.3}$

greater in order to make differentiating among the energies informative at all. In the first period of running, luminosities were very low; by the end of the run period, the detector was accumulating about ten Z^0's a day, or 0.3 nb^{-1}, for a total accumulated luminosity of 20 nb^{-1}.

3.3 The Mark II Detector

The Mark II detector is a general purpose detector for high energy particles. It is composed of many different subsystems. Most of these remained the same after the major changes of the upgrade. However, certain components were altered or added after it was moved to the interaction region of the SLC. Reference 29 gives a good description of the detector in its SLC incarnation. Figure 9 shows a view of the detector in the SLC running configuration.

Starting from the interaction region and travelling radially, the upgraded detector at PEP consisted of a straw chamber vertex detector, a drift chamber, time-of-flight scintillator, the solenoid coil, lead-liquid argon electromagnetic

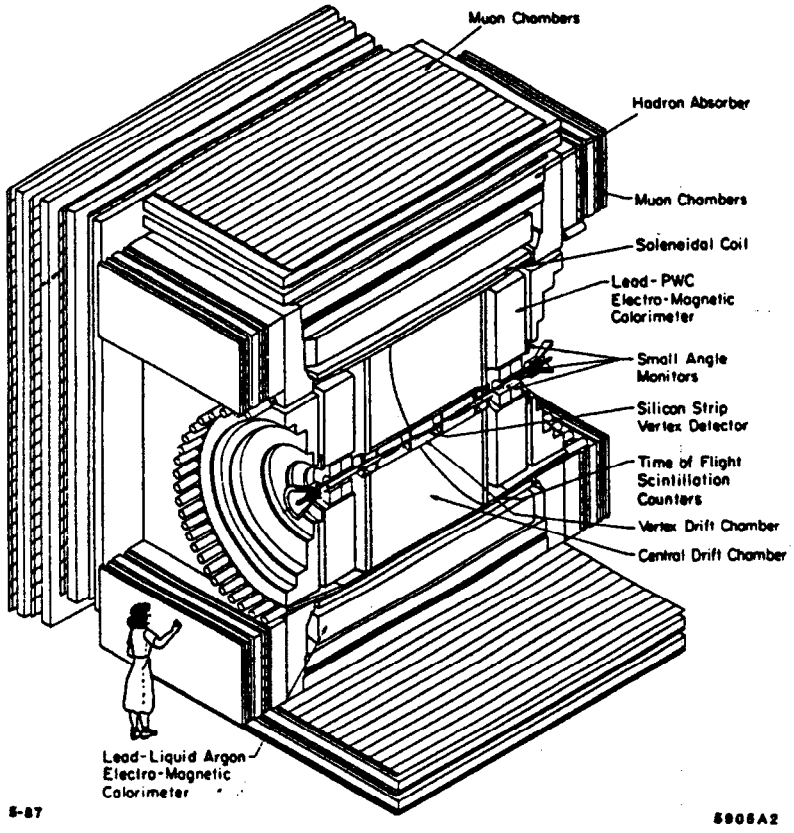

FIGURE 9. Isometric cut-away view of the Mark II/SLC detector, including vertex chambers which were not installed for the data used in this thesis. The central drift chamber is the component of most significance for this analysis.

calorimeters, and muon chambers. At either end were a lead-proportional tube electromagnetic calorimeter and a small angle tagger. When the detector was moved to the SLC interaction region, the straw chamber vertex detector was removed, since the beampipe size changed and new vertex detectors were to be installed. These were not installed for the period of data-taking included in this thesis. In addition, the small angle detector was replaced by two components called the Small Angle Monitor (SAM) and the Mini-SAM. Gaps in the calorimetry were covered with small electromagnetic shower detectors. In addition, muon solid angle coverage was increased by adding muon facades on the ends of the detector. Also, the energy spectrometer discussed above was installed. All of the components of the PEP upgrade detector and the SLC detector used in this thesis will be described in

more detail here, beginning with the central drift chamber. Components common to both the PEP running and the SLC running will be described first, followed by those elements of the detector which changed between PEP and SLC.

3.3.1 The Central Drift Chamber

A drift chamber detects charged particles with an array of wires held at different potentials in a gas. The passage of a charged particle through the gas splits the gas atoms into ions, which drift along the electric field set up by the wires and are collected on wires known as sense wires. Electronics attached to the sense wires detect the charged pulse from these ions. With enough of these wires in a drift chamber, the path of a charged particle can be followed. If a magnetic field is generated in the drift chamber, the charged particles will curve, and their momentum and charge can be determined by measuring the curve of the track that they leave in the drift chamber.

The drift chamber is the detector element of most importance for the reconstruction of K^0 and Λ. The momentum and charge of the decay products of the K^0 and Λ must be well measured in order to separate them from the background and accurately reconstruct the mass peak. This demands measurement of momentum in all three spatial dimensions.

The Mark II central drift chamber was replaced in the upgrade in order to improve measurement of track parameters in the high energy, high multiplicity environment of the SLC.[30] The chamber is cylindrical along z, with an inner radius of 19.2 cm and an outer radius of 151.9 cm. Its active length along the beam direction is 2.30 m.

The upgrade chamber is based on a jet cell with six sense wires; Figure 10 shows the cell design. These jet cells are known as supercells; their clustering of sense wires in tight groups allows precise local measurements to be made on a track without densely packing the drift chamber with wires. Figure 11 shows the arrangement of these supercells in the drift chamber. The sense wires are staggered

by ± 380 μm from the cell axis; this provides left-right ambiguity resolution within the cell. A row of 19 field wires on the edges of the cell controls the electric field. Guard and potential wires in the sense wire plane adjust the field direction in order to keep drift times uniform through the cell, thus improving position measurements, and they also adjust the gains to give uniformity of the signal size on the sense wires. The location of the wires must be well known in order to give accurate measurements of track position; this is accomplished by fixing all wires in one plane of the cell to notches in a feedthrough which is in turn fastened to machined holes in the endplate. The uncertainty in wire position is 35 μm.

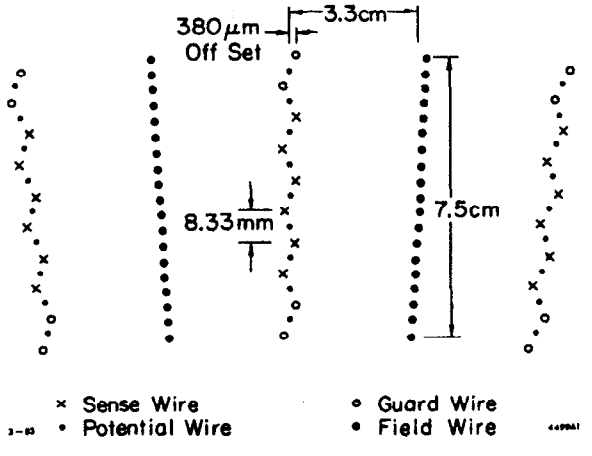

FIGURE 10. The configuration of the supercells in the upgraded drift chamber. A supercell contains six sense wires in the center of the cell, staggered to provide left-right ambiguity resolution. The sense wires are surrounded by guard and potential wires which shape the field; the sides of the cell hold the field wires which create the electric field in the cell.

These cells are arranged in twelve concentric cylindrical layers, as shown in Figure 11. Starting with the inner layer, the odd-numbered layers have their wires strung parallel to the beam direction. The even numbered layers are canted at $\pm 3.8°$ to provide stereo measurements, giving some z resolution to the chamber. This is crucial to the ability of the chamber to reconstruct the mass peak of the K^0 and Λ.

The endplates are 5.1-cm-thick aluminum, the inner shell is 2-mm-thick

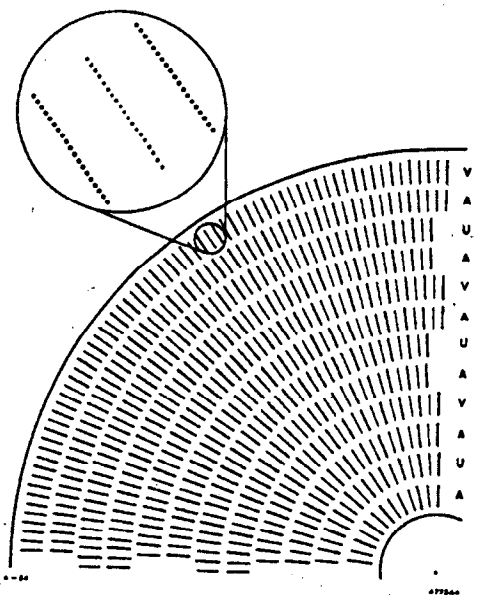

FIGURE 11. The configuration of the wires at the end plate of the drift chamber. Each cell contains six sense wires, as shown in the previous figure. The even numbered layers, here labelled U and V, have wires at an angle to the z axis to give z resolution.

beryllium, and the outer shell is 1.27-cm-thick aluminum. Aluminum ribs in the outer shell provide support. The inner and outer shells are lined with copper-clad Kapton; voltage on these linings maintains a uniform electric field in the nearby layers of drift cells.

The chamber was filled with a gas mixture of 89% Ar, 10% CO_2, and 1% CH_4 at a pressure slightly above 1 atmosphere. The magnetic field in the chamber was 4.5 kG at PEP and is 4.75 kG at SLC.

Graded high voltage is supplied to each cell, with field wires in the center of the cells typically at -4.5 kV, the potential and guard wires at about -1.5 kV and -200 V respectively, the sense wires at ground, and the copper linings at -2.5 kV. Voltages and currents were monitored by an IBM PC. The voltages are set so that the drift field is uniform at 900 V/cm, giving a drift velocity of 52 μm/nsec.

Signals from the drift chamber first pass through a preamplifier which is mounted directly on the wire feedthrough. Then the signal passes to a postamplifier which also shapes and splits the signal.[31] Timing is done with a LeCroy MVL407

comparator with its threshold set at 4% of the mean pulse height due to a minimum ionizing particle. Precise information on the time taken for ionization to drift to the sense wire indicates how far the track passed from the wire.

The timing signals are digitized by 96-channel LeCroy 1879 TDCs with a time bin width of 2 ns, allowing multihit discrimination so that two tracks both passing through the same cell can be separated. The pulse shape signals are brought to 16-channel 100-MHz Flash-ADCs (FADCs).[32] These FADCs have 6-bit resolution and are used for dE/dX measurements, which indicate how much energy the particle has lost while traversing the chamber and can be used for particle identification. This feature was not used in this thesis because other methods of identifying K^0 and Λ proved superior. However, the FADCs also provide pulse shape information which can be used to improve two-track separation, which is useful in reconstruction of neutral decays. Only one third of the chamber was instrumented with FADCs for the PEP test run.

Both the TDCs and the FADCs are read out through FASTBUS by SLAC Scanner Processors (SSPs).[33] There is one SSP in each FASTBUS crate; it performs zero suppression and pedestal corrections and formats the data. These are read out by system SSPs which communicate with the host VAX 8600.

Systems are calibrated with pulses injected into the preamplifier inputs. The calibration measures time propagation differences in each channel so that timing measurements will be accurate, and measures the pedestal and gain corrections for the dE/dx measurements.

Tracks in the drift chamber are found by fitting track segments within the supercells. Then these track segments were matched to form tracks passing through more than one superlayer.[34] The efficiency for finding tracks was measured at 99% at PEP and estimated from Monte Carlo for the SLC to be 96%; the drop is due to high multiplicity and track density in the SLC environment.[35]

The resolution for the distance of a track from an individual wire depends on the spread in the arrival time of the ionization which in turn depends on the

distance of the track from the wire. For tracks near the wire, the point resolution is 130 μm; for tracks far from the wire, it is 220 μm. Figure 12 shows the dependence of resolution on drift distance.

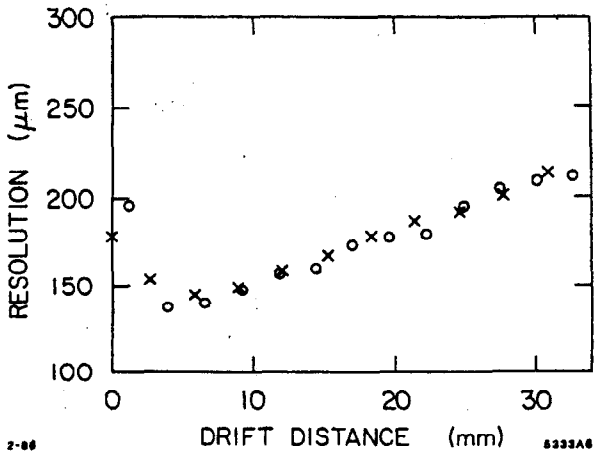

FIGURE 12. Upgrade drift chamber resolution *versus* distance of the particle from the wire. The circles show the resolution for Bhabha electrons while the X's give the intrinsic resolution.

Position resolution in the r-ϕ plane for fitted tracks extrapolated to the interaction point is 185 μm. With fitted velocities for the three drift distance regions of the cell and for different layers, it improves to 170 μm. Resolution in z is about 2.6 mm for the whole track extrapolated to the interaction point. The good resolution in r-ϕ is helpful for separating K^0 and Λ decays from backgrounds; as will be discussed in the next chapter, the distance of closest approach of the decay products from the interaction point provides an effective selection criteria in the search for K^0 and Λ. Two track separation from the TDC information was about 6.4 mm (for 80% separation). If pulse shape information from the FADCs is included, this improves to 3.8 mm, as shown in Figure 13.

The momentum resolution was measured from Bhabha scattering events at PEP for tracks with $|\cos\theta| < 0.64$. (Note that the magnetic field was 0.25 kG higher at the SLC.) It is $\sigma(p)/p^2 = 0.46\%(\mathrm{GeV/c})^{-1}$. It improves if tracks are

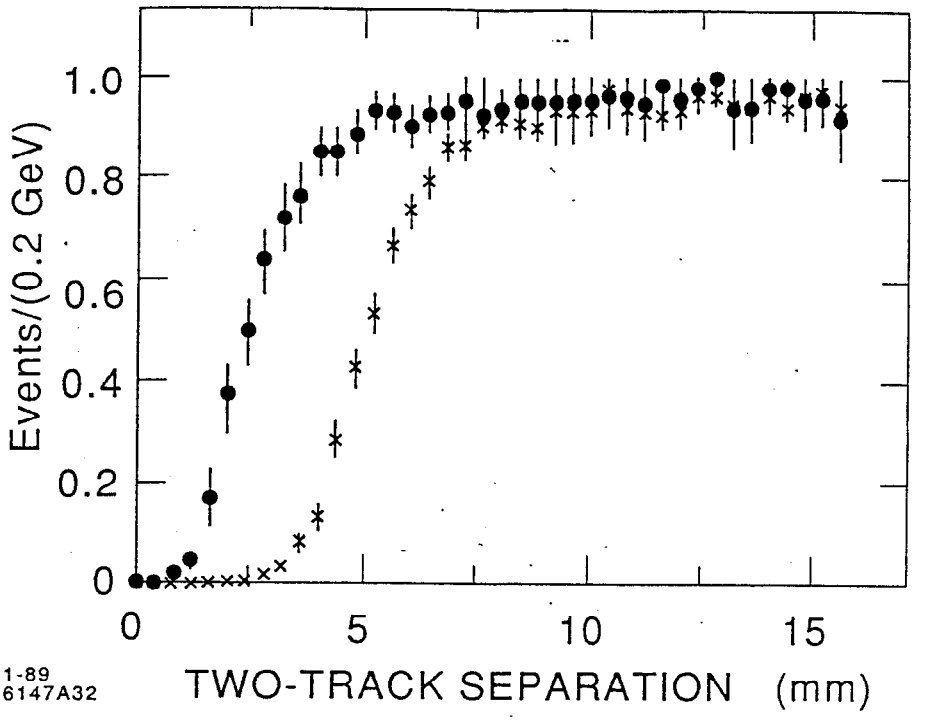

FIGURE 13. The efficiency of two track resolution of the drift chamber *versus* the track separation. Both TDC and FADC information are shown; the crosses represent the TDCs and the closed circles represent the inclusion of the FADC information.

constrained to come from a single point, but that feature is not used in the K^0 and Λ analysis, as their decay products do not come from the primary vertex. Multiple scattering from the drift chamber alone adds 1.4% to the resolution. Devices within the inner radius of the drift chamber degrade the resolution further through multiple scattering.

3.3.2 Time of Flight System

Outside the drift chamber is a time-of-flight (TOF) system, used to provide charged particle and cosmic ray identification. The system consists of 48 plastic scintillator counters arranged in a cylinder coaxial with the central drift chamber at a radius of 152.4 cm from the beam line. Charged particles passing through the scintillator give a flash of light; these flashes of light are read out at both ends by photomultiplier tubes. Reading out both ends allows for measurement of mean time and z position. Together with the momentum measured by the drift chamber, the mean time can give particle identification for low momentum particles.

The resolution of the time-of-flight system varied from 180 to 250 ps and gave an average value of 221 ps. The particle identification capabilities of the TOF system are not used in this analysis, as they are limited in energy range, and other methods of identifying K^0 and Λ were found to be more effective.

3.3.3 Solenoid

The magnetic field used for charged-track momentum measurement in the Mark II is provided by a conventional cylindrical coil which gives a maximum magnetic field of 5.0 kG in the center of the detector. The accurate measurement of momentum provided by this magnetic field is important to the reconstruction of K^0 and Λ, which are identified primarily by their reconstructed mass. The solenoid was run at 4.5 kG at PEP and 4.75 kG at the SLC. The coil is 405 cm long, with an inner radius of 156 cm and an outer radius of 171 cm. The coil is made of twelve aluminum conductors connected in series and wound into four contiguous cylinders. For a field of 4.75 kG the current is 7325 A and the heat dissipation is 1.8 MW. The inner radius of the coil is covered by a heat shield containing temperature-controlled water which keeps the central drift chamber temperature stable within a few degrees, giving stability to the gas gain of the chamber.

The field in the drift chamber has been measured and fit to polynomials in r and z. It is uniform to within 3% inside the tracking volume; The error in the polynomial fit of the field is less than 0.1%. During data taking the fit is normalized to the field measured by two Hall probes at either end of the chamber. This gives an absolute error on the field strength which is also less than 0.1%.

3.3.4 Liquid Argon Barrel Calorimeter

Outside of the magnet coil lies the barrel electromagnetic calorimeter, still working since the Mark II at SPEAR.[36] Its electron and photon identification capabilities were not used in the K^0 and Λ selection but were used in selecting the hadronic event sample for the analysis.

The electromagnetic calorimeter is made of alternating layers of 2 mm

of lead and 3 mm of liquid argon. Electrons and photons cause electromagnetic showers in the lead which cause ionization in the liquid argon. Alternate layers of lead are kept at positive voltage so that the ionization charge can be detected on the lead strips. The layers are arranged in eight modules in an octagonal vacuum vessel. They cover the polar range of $47° < \theta < 133°$ and the full range in azimuth except for 3° gaps between each module. Each module is $1.5 \times 3.8 \times 0.21$ m^3. The lead strips are aligned in layers parallel to the beam axis to measure ϕ, perpendicular to the beam axis to measure θ, and at 45° to aid in track reconstruction. Strips in layers with the same orientation are ganged together to reduce the requirement for readout electronics. Ganging is designed so that the section of layers and strips ganged together form an angular road which points back to the interaction region; this ensures that the energy from a particle coming from the interaction point will be deposited in layers read out by a single set of electronics. The ganging scheme is shown in Figure 14.

Inside the lead-liquid argon stack are two liquid argon gaps sandwiched with 1.6-mm aluminum strips. This measures shower energy for radiative losses in the solenoid coil. There are 1.86 radiation lengths of material before the lead stack, mainly from the magnet coil, giving a total of 16.0 radiation lengths to the back of the calorimeter.

The temperature in the liquid argon is maintained at 85 K with liquid nitrogen refrigeration in the module shells, which are enclosed in a common vacuum vessel. The field in the liquid argon is 12 kV/cm. The signals on the strips are amplified and shaped at the detector and then sent to sample-and-hold modules (SHAMs),[37] after which they are digitized by BADCs[38], which perform pedestal subtractions, linear gain corrections, and threshold cuts before sending the data to the host computer.

Electromagnetic showers are reconstructed[39] by projecting drift chamber tracks into the calorimeter and associating all energy in a narrow cone about the track with the track. Neutral showers are found by combinations of clusters in

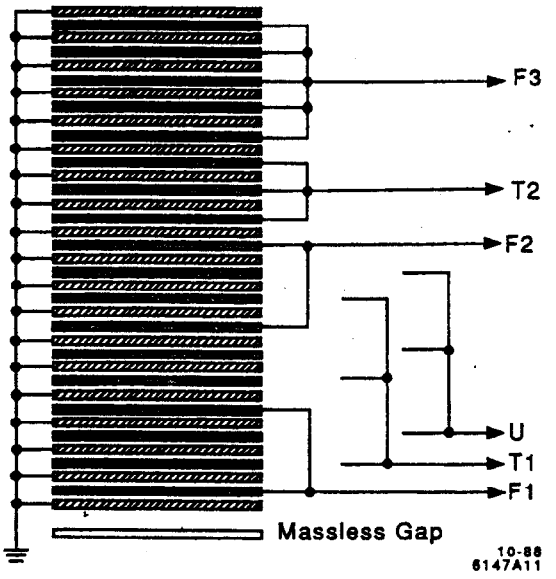

FIGURE 14. The liquid argon module ganging scheme. Nine layers oriented parallel to the z axis are ganged into three groups, covering the forward, central, and rear regions (F1,F2,F3). Six layers oriented perpendicular to z are ganged in two layers, front and middle (T1,T2). Three layers oriented at 45° to z are all ganged together (U).

different layers in the front half of the calorimeter; energy in the back half of the calorimeter is assigned after showers have been reconstructed in the front half.

The energy resolution, determined from Bhabha scattering at PEP, is $\sigma(E)/E = 4.6\%$. The σ represents the full width at half maximum for the energy distribution, shown in Figure 15, rather than the Gaussian width because the distribution is not Gaussian due to dead space in the calorimeter active volume and saturation in the electronics. Position resolution is $\sigma_\phi = 3$ mrad and $\sigma_z = 0.8$ cm.

3.3.5 Endcap Calorimeter

The endcap calorimeters extend electromagnetic calorimetric coverage in the Mark II over a range of $15° < \theta < 45°$, or 86% of the solid angle.[40] The fronts of the endcaps are located at 1.37 m in z from the interaction point. They are made of 36 layers of 0.28-cm-thick lead sandwiched with planes of aluminum proportional

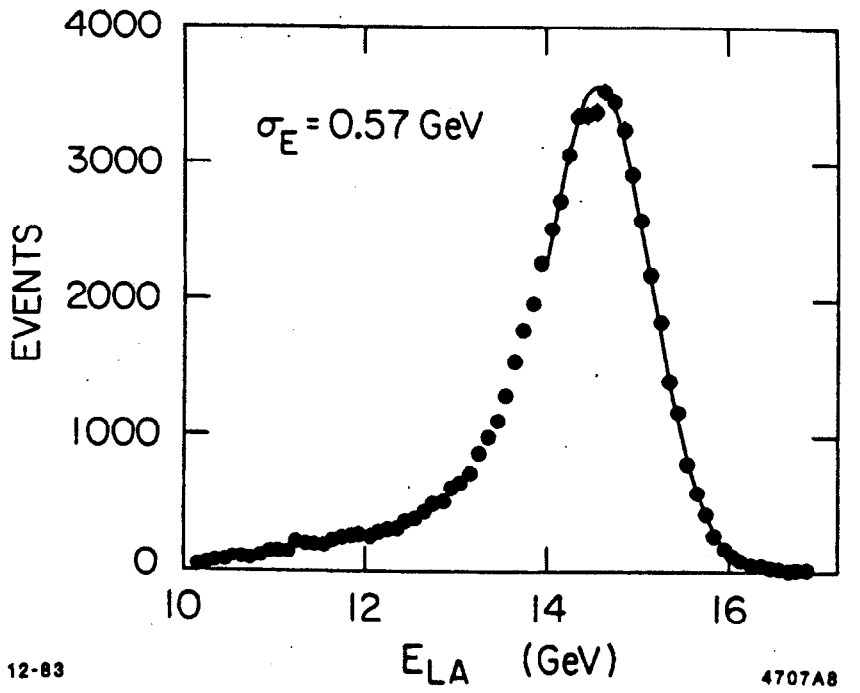

FIGURE 15. The energy resolution of the liquid argon, determined from Bhabha scattering at PEP. The non-Gaussian tails are due to dead space in the active volume and saturation in the trigger gap.

tubes. The charged particle showers generated in the lead produce ionization in the tube gas which is measured on a wire strung through the center of each tube. There are 191 proportional tubes per plane, each with a 0.9×1.5 cm^2 cross section. The tubes are glued together into an annular plane with inner radius 40 cm and outer radius 146 cm. There are five series of four planes oriented vertically, horizontally, and at $+45°$ and $-45°$. After these twenty planes, the last sixteen are oriented alternately horizontally and vertically. In total the endcap represents 18 radiation lengths of material.

The proportional tubes in the endcap are filled with HRS gas, like the drift chamber. Since the gas gain varies with density, temperature and pressure are monitored to correct the response to within 2%.

As in the barrel calorimeter, signals in the endcap are ganged together to reduce the number of electronic channels. Most grouping occurs in depth,

with some lateral ganging as well, all following a projective geometry from the interaction point. The readout electronics consists of preamplifiers and shaping amplifiers mounted nearby, followed by SHAMs[37] and BADCs[38] as for the liquid argon calorimeter.

Figure 16 shows the response of the endcap to a test beam containing from one to five 10-GeV positrons.

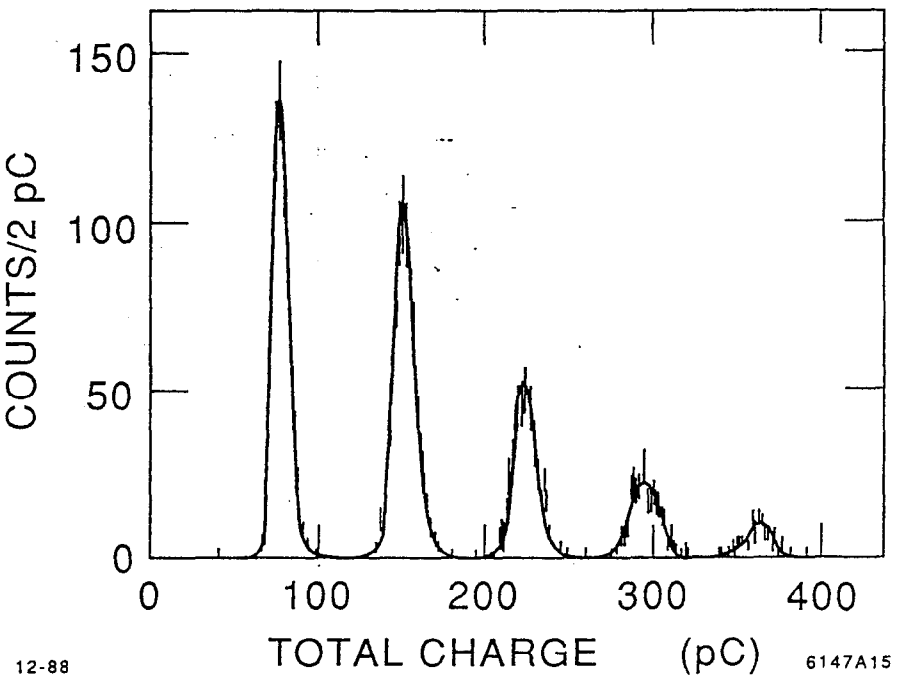

FIGURE 16. The response of the endcap to a test beam containing between one and five 10-GeV positrons. The peak for each number of positrons is clearly visible.

The endcap can reject 99% of pions while accepting 95% of electrons at a momentum of 5.0 GeV/c. The energy resolution, studied with Bhabha scattering events at PEP, is $22\%/\sqrt{E}$ (E in GeV).

3.3.6 The Muon System

The basic muon system for the upgraded Mark II consists of four muon walls, each made of four layers of iron, alternating with four layers of proportional tubes. These muon walls are mounted on the four sides of the detector parallel to the beam axis. The iron is expected to screen out all charged particles except muons, so that any charged particle which leaves hits in all four layers of the muon system is considered a muon. The solid angle coverage is 45% for particles penetrating all four layers.

For running at the SLC, a muon upgrade system was built to extend the solid angle coverage of the muon system. It was not installed during the PEP trial run. The muon systems are not used in this analysis, and will not be described further.

3.3.7 Vertex Detector: PEP

For the period when the upgraded Mark II detector was taking data at PEP, a new vertex chamber was installed. It was only used during the PEP run, as the size of the beam pipe at the SLC was to be smaller, and special vertex chambers were designed for the SLC running. The vertex chambers designed for the SLC were not installed for the data runs used in this analysis, and will not be discussed. However, the straw chamber vertex detector used for the trial of the upgraded detector at PEP had a significant effect on track resolution and therefore is important in the reconstruction of the K^0 and Λ in that data. Further information on the straw chamber vertex detector used at PEP can be found elsewhere;[41] a brief discussion follows.

The vertex chamber used in the PEP upgrade detector was primarily intended as an aid to the trigger, but since time-digitizing electronics were left from the previous vertex chamber, it was also designed to give position measurements. The chamber was composed of 552 single-wire proportional cells. These cells were designed to work on the same principles as the drift chamber: particles traversing

the gas inside them ionized the gas, and electric fields caused the ionization to drift to a central sense wire.

Each cell had a tubular cathode at a radius of 4 mm around an anode sense wire. These tubes were constructed of mylar, aluminized on the inner surface.[42] The sense wire was 20 μm diameter gold-plated tungsten.

TABLE 6. The radii and number of straws in the straw chamber layers, together with the stagger of the beginning of the layer from $\phi = 0$. The radii given are the values at the center of the straws, or the wire radii.

Layer	Radius (cm)	No. of Straws	Stagger (mrad)
1	9.49	72	0.0
2	10.55	80	−3.8
3	11.60	88	+35.4
4	12.65	96	+29.7
5	13.71	104	−0.5
6	14.76	112	−2.4

These proportional tubes were arranged in six layers, starting at a radius of 9.5 cm and ending at 14.8 cm. The radial distances of the layers are shown in Table 6, and Figure 17 shows a cross section of the straw chamber. Because the radius of the layers increased and the proportional tubes in a layer had no gaps between them, the number of proportional tubes per layer had to increase. It went from 72 to 112 by increments of eight cells per layer. The cells were offset along a given radius to minimize the dead space seen by tracks.

The active length of the tubes was 75 cm; this gave coverage in θ of $\pm 67°$, to match the acceptance of the first three superlayers of the central drift chamber. This fiducial volume gave efficient triggering for tracks coming from the interaction point but reduced the volume for triggering on beam-gas and cosmic ray events.

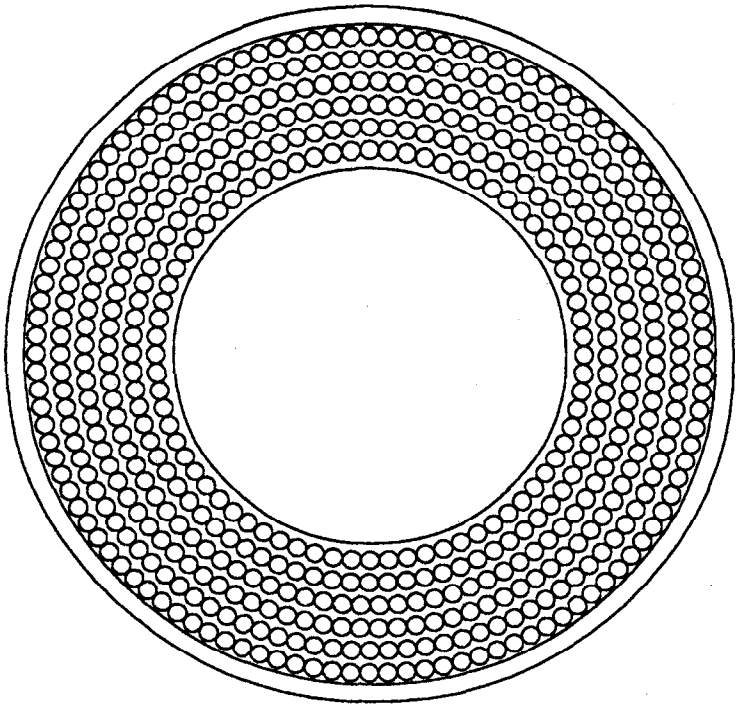

FIGURE 17. The cross section of the straw chamber vertex detector used in the trial of the upgraded Mark II detector at PEP. The tubes are arranged in six layers, staggered so that no track can pass only through the walls of tubes.

The wire placement tolerance was 25 μm in order to give good resolution on the impact parameter of tracks. To achieve this, tubes and wires were strung from the end plates under tension. The end plates were 1.9-cm-thick aluminum, which were held apart by a cylindrical outer shell made of 8-mm-thick acrylic foam between 75-μm aluminum foils. The use of foam between thin foils gave the chamber strength without presenting too much material for multiple scattering in front of the main drift chamber. The inner shell was copper-clad Kapton. The whole chamber represents 0.012 radiation lengths of material along the radial direction.

The cells of the vertex detector were operated with the anode at ground potential and the cathode at negative high voltage of -1.9 kV. Each layer was on a separate power supply, so a layer could be turned off if a cell within it failed until

such time as the cell could be disconnected from the high voltage bus and the layer brought back on. However, only one cell failed during running at PEP.

Signals from the straw cells were brought to a variable threshold discriminator, a LeCroy-MVL100 amplifier/comparator. The digital output from the MVL100 was sent to a time-to-amplitude converter (TAC)[37] which provided latched output signals to the Mark II trigger system and analog levels to a BADC/CAMAC readout module.[38] The BADC converted raw data to calibrated drift time before reporting the data to the Mark II host computer. For calibration, timed pulses were sent to the chamber on the cathode high voltage lines, and read back through the full series of electronics.

The gas used in the straw chamber vertex detector was 50% argon 50% ethane at atmospheric pressure. For high voltage of 1.9 kV, this gave a gain of $\sim 3 \times 10^5$. The discriminator threshold was set at 620 μV.

These parameters gave an efficiency for a given cell firing in response to a track of 0.93. Inefficiency came mostly from geometrical effects such as tracks passing through spaces between cells or tracks passing close to the tube wall, where they intersect a much smaller active region. The point resolution of the cells is 90 μm averaged over the entire cell.

Tracks in the vertex chamber are found by taking a found track in the central drift chamber and searching layers inward for hits matching that track. The tracking program loops over layers, hits in the layers, and left-right ambiguity (nested loops, layers forming outermost loop) until it finds a candidate that passes its χ^2 cut for matching the drift chamber track.

The resolution provided by including the straw chamber information in the track fits is an improvement on the drift chamber alone. The straw chamber information improves the extrapolation error on the distance of closest approach to 80 μm for high momentum tracks. This helps the background rejection in the search for K^0 and Λ. The straw chamber also improves the momentum resolution

for tracks in the drift chamber by 20%. The improvement in momentum resolution improves the mass resolution for K^0 and Λ which decay inside the straw chamber.

3.3.8 Vertex Detectors: SLC

Two vertex detectors were designed for use in the SLC: a silicon strip vertex detector (SSVD) and a drift chamber vertex detector (DCVD). However, during the first data taking at the Z^0 resonance, these were not yet ready for installation, and the beam pipe was too large to fit inside these detectors as it contained wire flippers for measuring the beam size. These vertex detectors are not used in this analysis.

3.3.9 Luminosity Monitors

The luminosity monitors also changed between the run of the Mark II upgrade at PEP and the running at the SLC. The purpose of the luminosity monitors is to measure small-angle Bhabha events. Since the cross section at small angles is large, this gives a more statistically accurate measure of luminosity than do Bhabhas at large angles in the liquid argon. All work on the principle of finding electromagnetic showers in a large amount of material. Some also include tracking capabilities. The are the Small Angle Tagger (SAT) used at PEP, and the Small Angle Monitor (SAM) and mini-SAM in use at the SLC. They are not used in this analysis and will not be described further.

3.3.10 Small Electromagnetic Shower Detectors

Scattered around the Mark II detector at the SLC are a number of small detector systems designed to cover holes in the main calorimetry. Their signals are all processed with those from the Mini-SAM. These were not used in this analysis, and will not be discussed further.

3.3.11 Energy Spectrometer

Since the SLC is a single pass colliding beam machine rather than a colliding storage ring, energy could not be calculated exactly from the machine tuning. Therefore, the energies for the electron and positron beams had to be determined separately on a continuous basis. To this end, energy spectrometers were installed in the extraction lines downstream of the interaction point. These are only used in this analysis in the sense that they measure the energy of the hadronic events; but since this thesis combines data from several energies in the region of the Z^0 and uses the average energy, 91 GeV, as the stated energy of the hadronic events, precise energy measurements are not of much importance to this analysis. Therefore the spectrometer will be described only briefly.

After the beams collide, kicker magnets dump them out into the extraction line. Spectrometers were installed in these extraction lines at a distance of 150 m downstream of the IP. The spectrometer consists of three dipole magnets, The middle magnet is a very- well-measured spectrometer magnet. The bending of the beam in this magnet is inversely proportional to E_{beam}. The other two dipoles bend the beam perpendicularly to the direction of the spectrometer magnet bend, causing the beam to emit synchrotron light in two lines, each about 5 cm wide. At the beam focal point, about 15 m downstream, the distance between these two lines of light is measured. This distance gives the angle through which the beam has been bent by the spectrometer magnet. The angle together with the magnet strength gives the beam energy, and the thickness of the synchrotron stripes gives the spread of the beam energy. Absolute accuracy of the energy measurement is ± 35 MeV.

3.3.12 Trigger System

There are two levels of trigger in the Mark II trigger system: a primary trigger which determines whether an event is of possible interest and, if it is, turns on the secondary trigger processors, and the secondary trigger, which prevents future events from entering the system until it decides whether the event is of sufficient interest to be read in to the computer for full processing and recording. An event of interest usually involves a certain level of neutral or charged energy. A primary trigger is necessary in a high rate environment in order to keep the detector available for data taking as much as possible; if the secondary trigger looks at every event, it misses many which come while it is busy with the first, and this reduces the efficiency for finding events of actual interest. There were some differences between the triggers at PEP and at the SLC; one of the chief of these was the primary trigger. The SLC has beam crossings at a rate of at most 180 Hz, whereas PEP beams collided every 2.3 μsec. Therefore, at the SLC the primary trigger came from the beam timing signal, but at PEP the primary trigger had to be more selective.

The trigger system for PEP and SLC contains three components: a charged particle trigger, a calorimeter energy trigger, and a small-angle Bhabha trigger. PEP primary triggers came from either a sum of calorimeter energies or a sum of hits in the tracking chambers. The liquid argon modules and endcaps had two thresholds. Various combinations of high and low thresholds could be required for a calorimeter trigger. Signals in the drift chamber, vertex chamber, and time-of-flight system were combined for track primary triggers as follows. Each layer was ORed together, and a programmable logic unit looked at these ORs to determine if enough layers showed hits to give a charged trigger pulse. A further programmable trigger unit made the primary trigger decision by combining the charged trigger pulse with the calorimeter trigger pulse. If there was not a primary trigger, the detector was cleared; otherwise, the secondary trigger was started.

The secondary trigger was based on a more sophisticated charged particle

trigger and on calorimeter trigger pulses. Actual tracks were required for a charged particle trigger; these were found by a fast track-finding processor, which used 24 curvature modules, each searching for tracks of a given charge and momentum range.[44] These modules accepted input from twelve layers. At PEP, these twelve layers were a mix of vertex chamber layers, the time-of-flight scintillator, and drift chamber supercells; at the SLC, these were the twelve supercell layers of the drift chamber. A supercell was considered hit if four out of six wires in the cell had seen signals. The modules started at $\phi = 0$ and progressed around the drift chamber in 252 steps of 100 nsec. The progression in ϕ was accomplished by connecting each layer used in the trigger to a circular shift register and passing through the shift register in unison in ϕ, using different clock signals to compensate for the different number of cells in each layer. The curvature modules put progressive programmable delays on each layer in order to search for coincidences along paths of the required radius (momentum). If a curvature module saw a number of hits in its momentum road greater than its programmable threshold, it recorded a found track. The number of found tracks was passed to the Master Interrupt Controller (MIC) which also received the summed calorimeter module energies. Various combinations of charged particles and calorimeter energy could be required.

The calorimeter trigger at the secondary level used a table of constants in the Memory Logic module to identify interesting patterns of energy deposition. It used the small angle luminosity monitors to form luminosity triggers, and endcap and liquid argon calorimeter information to generate a Total Energy Deposited (TED) trigger. The TED trigger looked at groups of eight neighboring channels in the calorimetry to compare their sums with programmable threshold voltages. If the MLM saw an interesting event either through the TED trigger or the luminosity trigger, it notified the MIC.

An SSP-based Software Trigger (SST) gave an alternate calorimeter trigger. A SLAC Scanner Processor, the base of the SST trigger, provided more flexibility than the TED trigger. Copies of the liquid argon and endcap trigger

sums were digitized and sent to the SSP, which defined hits based on three software thresholds. Clusters of energy pointing to the interaction region were found using a table of precalculated patterns.[45]

Cosmic ray data were used for testing the detector; their trigger was provided by the charged particle trigger without the beam crossing primary trigger. A Coplanar Track Finder could require back to back tracks in curvature modules in order to reduce the triggering frequency in cosmic ray runs.

3.3.13 Data Acquisition

The data acquisition system for the upgraded Mark II detector was controlled at the SLC by a VAX 8600 computer and at PEP by a VAX 11/780. These computers run independent processes which communicate via shared memory and instructions. These processes have to read both CAMAC and FASTBUS data, merge raw data with results of online processing, log data to tape and sometimes to disk, monitor detector performance and parameters, do online analysis, and communicate with operators.

All data reaches the VAX through CAMAC or FASTBUS interfaces. The CAMAC interface is a microprocessor system known as the VAX CAMAC channel (VCC).[46] The VCC monitors two system crates which are connected with the 44 data acquisition crates. Multiple reads of BADC memories and other modules are required in event acquisition from CAMAC. Data transfer occurs at about 1 Mbyte/s.

The FASTBUS data acquisition system is shown in Figure 18.

The VAX communicates with FASTBUS through a DEC DR-780 32-bit parallel port and DR-32 Device Interconnect cable (DDI). The DDI connects with another interface.[47] This interface connects with buffer modules in two system FASTBUS crates. One contains five system SSP modules each of which control five remote data acquisition crates[48] with an SSP serving as crate controller and data processor. The second crate is designated for future on-line data processing.

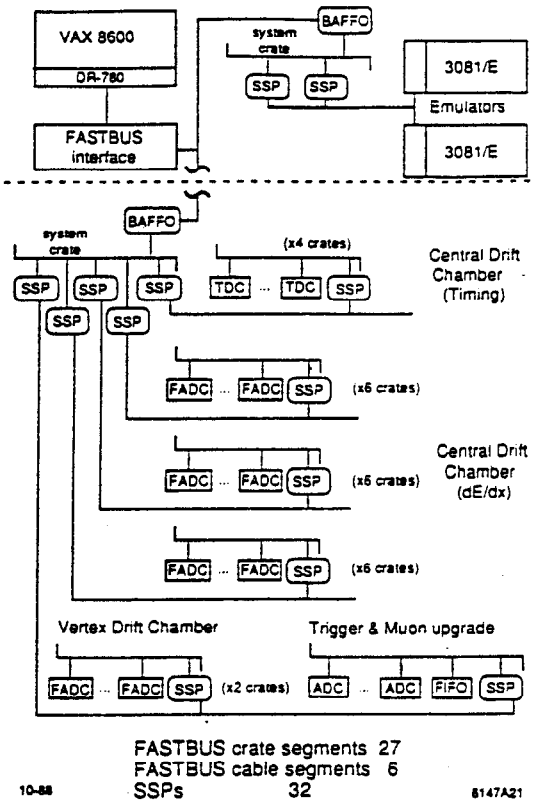

FIGURE 18. The data acquisition system for FASTBUS in the SLC configuration, with vertex chamber and muon upgrade in the system.

Events are first processed in the remote crate SSPs, then sent to the system SSPs. The master SSP collects all the FASTBUS data for an event and then interrupts the VAX, which acquires all the data in a single block read. The data transfer rate is about 5.5 Mbyte/s.

Data acquisition is started by the primary trigger. This starts the secondary trigger logic and BADC processing. The VAX reads the CAMAC data and when the master system SSP signals that the FASTBUS system is ready for data again, the trigger is reset. The FASTBUS data is read in and combined with the CAMAC data, and the whole event is put in a global buffer. Online analysis can be performed before tape logging. After tape logging is finished the event is removed from the buffer.

CHAPTER 4

DATA SELECTION

In order to study K^0 and Λ production in hadronic events, it is first necessary to define a sample of hadronic events: events where a Z^0 or γ decays into $q\bar{q}$, which subsequently form hadron showers. Most hadronic events are easily distinguished from other types of events by the fact that they have high multiplicity and a good deal of energy visible in the detector; some, however, send most of their energy down the beampipe or for other reasons do not appear in the detector. Others have low multiplicity. In this analysis, only hadronic events which possess the identifying features are used, and compensation is made for those lost with a Monte Carlo calculation of the detection efficiencies. The first part of this chapter describes the selection criteria for hadronic events at 29 and 91 GeV. The criteria are somewhat different at the two energies, partly because the properties of the hadronic events and their backgrounds change, and partly in order to match analyses already done on properties of hadronic events in these two data samples.

After the sample of hadronic events has been defined, the K^0 and Λ must be tagged. Because both the K^0 and the Λ contain a strange quark, they must undergo weak decay. The strange quark(antiquark) emits a $W^{-(+)}$ boson which then decays to a $d\bar{u}$ ($u\bar{d}$) pair, as shown in Figure 19.

The combination of this pair with the spectator quark or diquark and the $u(\bar{u})$-quark left by the emission of the W boson gives a two-prong decay topology. Depending on how the decay products combine, the two prongs are either both neutral or both charged. Table 7 shows the two-prong decays of the K^0 and Λ, together with their frequency. Of course, there are other decay modes, but decay into two pions (for the K^0) or a nucleon and a pion (for the Λ) dominates.

Since these particles must undergo weak decay, their lifetimes are long.

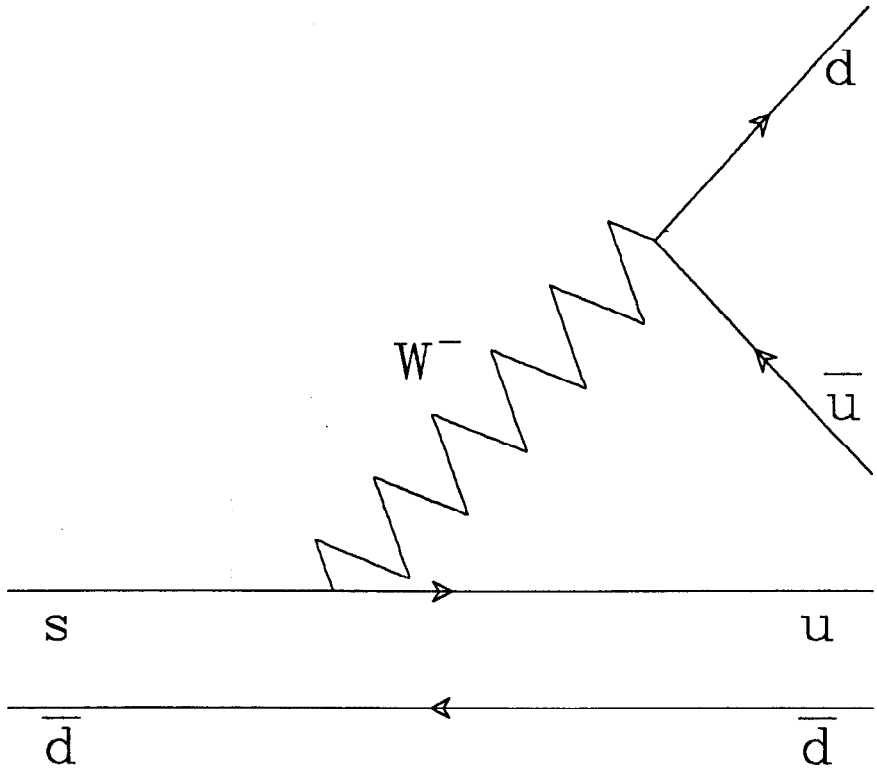

FIGURE 19. Schematic diagram of the process of K^0_S decay into two charged pions. The strange quark emits a W^- boson which decays into a pion, while the spectator antiquark combines with the up quark left from the s quark decay to make another pion. Λ decay is similar, except that the $\bar{d}$ quark line is replaced by a u quark line and a d quark line.

This leads to their appearing in the detector as two charged tracks originating from a point away from the main vertex, as shown in Figure 20.

Many of them decay very near the main vertex, but enough decay far away to make a search for detached two prong vertices an effective method for obtaining a clean sample of K^0 and Λ. The second part of this chapter details the cuts used to search for these detached vertices.

4.1 Hadronic Event Selection

Hadronic events are distinguishable by higher average multiplicity and visible energy than most other interactions. There are other types of interactions which can mimic hadronic events. Among these are hadronic decays of the tau lepton; however, tau decays usually have one or three charged prongs per tau

TABLE 7. The decay modes and branching ratios for the K_S^0 and Λ.[49]

Particle	Decay Mode	Branching Ratio
K_S^0	$\pi^+\pi^-$	$68.61 \pm 0.26\%$
	$\pi^0\pi^0$	$31.39 \pm 0.26\%$
	$\gamma\gamma$	$(2.4 \pm 1.2) \times 10^{-6}$
	$\pi^+\pi^-\gamma$	$(1.85 \pm 0.10) \times 10^{-3}$
	$\pi^+\pi^-\pi^0$	$< 5 \times 10^{-5}$
	$\pi^0\pi^0\pi^0$	$< 4 \times 10^{-5}$
	$\mu^+\mu^-$	$< 3.2 \times 10^{-7}$
	e^+e^-	$< 1 \times 10^{-5}$
Λ	$p\pi^-$	$64.1 \pm 0.5\%$
	$n\pi^0$	$35.7 \pm 0.5\%$
	$n\gamma$	$(1.02 \pm 0.33) \times 10^{-3}$
	$pe^-\nu$	$(8.34 \pm 0.14) \times 10^{-4}$
	$p\mu^-\nu$	$(1.57 \pm 0.35) \times 10^{-4}$
	$p\pi^-\gamma$	$(8.5 \pm 1.4) \times 10^{-4}$

and high multiplicity tau decays are rare. Another source of backgrounds can be beam-gas events, where the electron or positron interacts with residual gas in the beam-line and sends a spray of particles into the detector. The third major source of backgrounds is two-photon events which produce hadrons, as shown in the Feynman diagrams in Figure 21.

The hadronic event selection criteria described below are designed to minimize these backgrounds. The criteria vary between the PEP upgrade running at 29 GeV and the SLC running near 91 GeV because the importance of these backgrounds changes between energies, as do the topologies of the hadronic events themselves.

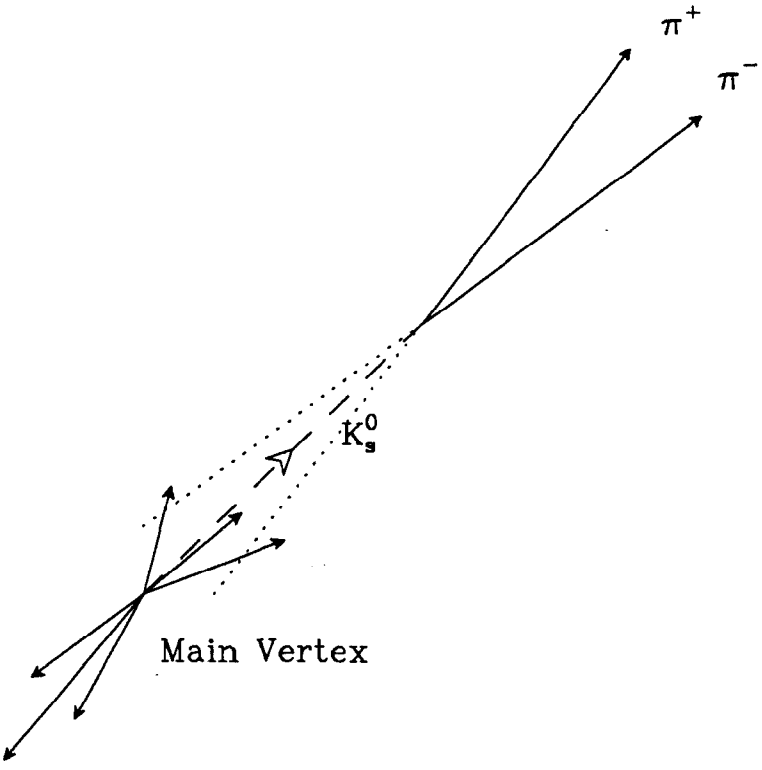

FIGURE 20. The topology of a K_S^0 decaying into two charged pions in a hadronic event. Note that the tracks from the decay products, if extrapolated back towards the primary vertex, can have a large miss distance from the primary vertex.

4.1.1 Event Selection at 29 GeV

The selection criteria used at 29 GeV have been chosen to match those used in the measurement of R in the data sample taken with the upgrade detector.[24] Before cuts can be made on quantities calculated from charged and neutral tracks, one must define what constitutes a good charged or neutral track.

To be a good charged track, a track must be well inside the detector, come from an area near the interaction region, and have well-measured momentum. The cuts imposed on charged tracks are:

1. The transverse momentum of the track must be greater than 0.10 GeV: $p_\perp > 0.10$. This cut eliminates tracks which have momenta so low that the magnetic field makes them spiral inside the detector. These spiraling tracks cannot be well measured.
2. The angle the track makes with the z-axis must have $|\cos\theta| < 0.825$. This

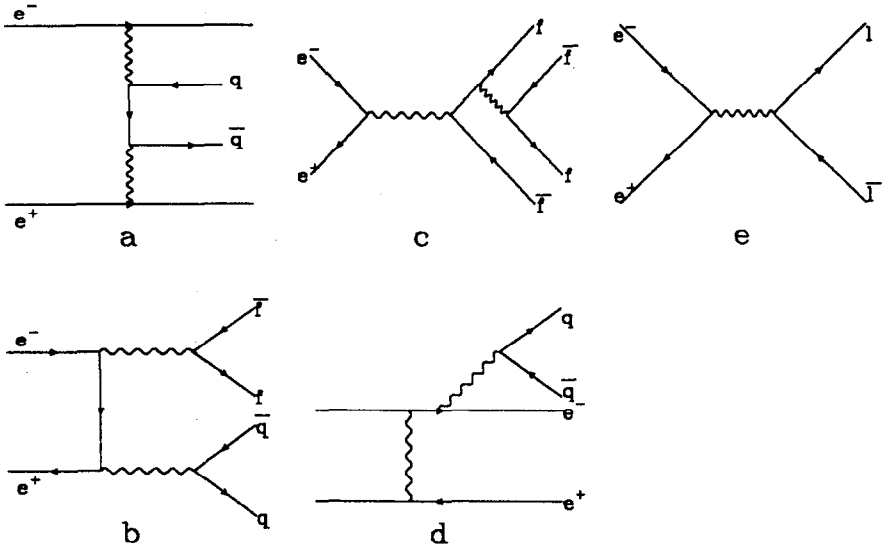

FIGURE 21. Some of the possible physics backgrounds to hadronic events, shown as Feynman diagrams. Drawings (a-d) represent the two-photon processes, and drawing (e) shows two-lepton production.

requirement keeps only those tracks which are in the good fiducial volume of the detector, where efficiency is well understood. Tracks with larger $|\cos\theta|$ exit the ends of the drift chamber before passing through enough layers of wires to be well measured.

3. The track must come from a cylinder around the interaction point with radius $R = 5$ cm and half-length in z of 7 cm. This requirement eliminates tracks from cosmic rays or beam-gas events which occur far from the interaction point.
4. The momentum of the track must be less than half the center-of-mass energy plus three times the error on the momentum:

$p > \frac{E_{cm}}{2}(1 + 0.015E_{cm})$. This eliminates tracks with unphysical momenta: no track from a particle created in the e^+e^-collision should have momentum greater than half of the center-of-mass energy. The factor of $0.015E_{cm}$ allows the track momenta to be smeared high by three times the error on the momentum. No track with error larger than this can be considered well-measured.

For selection of hadronic events, neutral energy is also considered. The criteria for a good neutral track measured in the calorimeter are:

1. The shower energy must be well within the energy range for high efficiency measurement: $E_{sh} > 250$ MeV. This gives well understood energy reconstruction efficiency.
2. The shower has to be isolated by at least 30 cm from any charged track at the front face of the calorimeter. This prevents double measurement of charged track energy.
3. The angle with respect to the beam direction must have $|\cos\theta| < 0.825$. This requirement was chosen to match the charged track acceptance.

The charged and neutral tracks thus selected are then passed through the hadron selection. Requirements for good hadrons are listed below.

1. The number of charged tracks must be greater than four. This requirement eliminates Bhabha and $\mu^+\mu^-$ events and eliminates most $\tau^+\tau^-$ and two photon events.
2. The charged energy must be greater than $0.26E_{cm}$.
3. The visible energy (charged energy plus photon energy) must be greater than $0.4E_{cm}$ These two requirements further reduce the background from two-photon events and beam-gas events.
4. The momentum must be balanced both along z and in the transverse direction. The requirements on momentum balance are:

$$p_\perp = \sqrt{(\Sigma p_{x_i})^2 + (\Sigma p_{y_i})^2} < 10 \text{ GeV}$$

$$|\Sigma p_{z_i}| < 10 \text{ GeV}$$

The sums include both charged and neutral tracks. The momentum balance requirement further reduces backgrounds from two-photon events, beam-gas events, and $\tau^+\tau^-$ events. It also cuts events which have very hard initial state radiation.

5. The charge of the event must be balanced to within five: $|\Sigma q_i| < 5$. This requirement further reduces backgrounds from beam-gas events.
6. The fitted vertex of the event has to be consistent with the measured beam interaction point to within 6 cm in z: $|z_v| < 6$ cm. This requirement also eliminates beam-gas events.

The final hadron sample resulting from these cuts is discussed in the next chapter.

4.2 Hadronic Event Selection in the Z Resonance Data

In the data sample taken at the Z^0 resonance, the requirements for hadron selection are different than those for the 29 GeV data. This arises for several reasons: since the energy is higher, multiplicity is higher in hadronic events, while some of the backgrounds remain the same in multiplicity. Likewise, the cross-section for Z^0 production of hadronic events becomes large at the resonance, but the cross-section for two-photon events falls from the value at 29 GeV, thus reducing a major contribution to the hadronic event background.

On the other hand, the beam-related backgrounds are worse at the SLC, so the Z^0 resonance data has backgrounds from synchrotron radiation and soft photon conversions mixed with the event information in the detectors. This can confuse the tracking algorithm. Also, the higher multiplicities and denser jets somewhat degrade the measurement of individual tracks.

These effects call for different selection criteria at the Z^0 resonance than those used at 29 GeV. The criteria used here are chosen to match the Mark II measurements of inclusive distributions in hadronic Z^0 boson decays.[50]

Again, good charged tracks and good neutral tracks have to be selected before the hadronic event sample can be determined. Good charged tracks are defined as follows:

1. The track must pass with 1 cm in radius and 3 cm in z of the measured interaction point. This cut eliminates tracks from beam-related backgrounds such as beam-gas events and photon conversion in the detector.
2. The polar angle of the track has to have $|\cos\theta| < 0.82$. This ensures that the track traverses enough layers of the drift chamber to have well measured momentum. This cut ensures that the track has passed through at least five superlayers, so that it can have hit information on thirty wires.
3. The transverse momentum of the track has to be greater than 0.3 GeV, which allows tracking efficiency to be well-understood. For tracks with momentum above 10 GeV, the momentum measured with a vertex-constrained fit is used, as this gives a better measurement of the momentum. Vertex-constrained fits to the tracks are not used for lower momenta because multiple scattering and secondary decays give too large an uncertainty.

Good neutral energy is defined by the following criteria:

1. In the barrel calorimeter, electromagnetic showers have to be within $|\cos\theta| < 0.68$ in polar angle. They also have to be inside the fiducial volume in azimuth, meaning that the center of the shower has to be inside a liquid argon barrel module by at least one strip. These criteria accept

showers in a fiducial volume of 63.5% of the solid angle. This ensures well-measured energy.

2. In the end cap, the showers have to lie within a fiducial volume extending over $0.74 < |\cos\theta| < 0.95$; again, this requirement ensures that the shower energy is well-measured.
3. The energy of the shower has to be greater than 0.5 GeV. This cut is imposed both to ensure that the shower energy is well-measured and to eliminate backgrounds from the machine, both in the form of soft photons and in the form of muons from upstream collimators which traverse the length of the liquid argon modules.

The electromagnetic showers which pass these criteria are retained whether or not they are associated with a charged track.

Using the charged tracks and electromagnetic showers thus chosen, events are tested with the hadronic event criteria, of which there are only two:

1. The number of charged tracks has to be greater than or equal to 7. This requirement eliminates nearly all tau decays and most of the two-photon events.
2. The visible energy of the event has to be greater than $0.5E_{cm}$, with visible energy defined by:

$$E_{vis} \equiv \Sigma_{ch}\sqrt{(p_{ch}^2 + m_\pi^2)} + \Sigma_{neu}E_{neu}$$

using charged and neutral tracks selected with the above criteria. This cut further reduces backgrounds from two-photon and beam-gas events. It also eliminates some of the true hadronic events which are not well-measured because the thrust axis of the event lies too near the beam axis, so that most of the energy of the event goes down the beampipe.

These cuts give the final hadronic event sample which is used for the

search for K^0 and Λ. The criteria used to find K^0 and Λ in these events are described in the next section.

4.3 K^0 and Λ Selection

As mentioned in the beginning of the chapter, the decay products of many K^0 and Λ should appear in the detector as two charged tracks coming from a vertex which is detached from the primary vertex. These vertices and decay products must somehow be separated from the random combinatorial background of other tracks in the event, which give an invariant mass distribution of the shape shown in Figure 22, in order to obtain a clean sample for studies of production distributions.

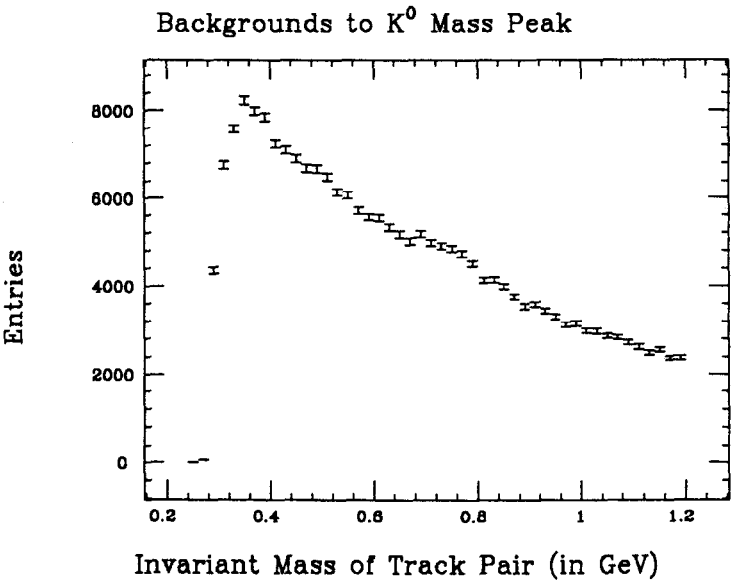

FIGURE 22. Shape of the combinatorial background to the invariant mass distribution for the K^0. The shape is similar for Λ, only boosted up in mass by the assumption that one of the tracks has the mass of a proton.

The selection criteria used in this analysis are chosen to give a quite clean sample while still keeping the efficiency for tagging K^0 and Λ decays as high as possible. The selection criteria are kept the same for analyzing the data at 29 GeV and the data at the Z^0 resonance, so that systematic errors arising from the detector and event reconstruction can remain as much the same as possible between the two

energy regions, given the different machine environments. A number of possible parameters of these vertices and decay products were studied; the values of cuts on these parameters were varied. These were studied at both 29 GeV and at 91 GeV, and a set chosen which worked well for both, although due to the dearth of data at the higher energy, primacy was given to the behavior of the Z^0 resonance data in setting the cuts.

The basic rationale behind the selection criteria chosen for this analysis is that the two tracks emanating from the decay vertex of a K^0 or Λ will, for the most part, have some opening angle and thus form a "V" in the detector. If the K^0 or Λ travels some distance from the primary vertex before decaying, its decay products, when extrapolated back from the decay vertex, should miss the primary vertex. Therefore, by taking all pairs of oppositely charged tracks which miss the primary vertex and form a reasonable secondary vertex, one can reconstruct a clean sample of K^0 and Λ. The precise criteria used to select these tracks and determine what constitutes a reasonable secondary vertex are discussed below. A standard Mark II package for reconstructing neutral decays is used as the framework in which to impose these criteria: VFINDP. It has been described extensively elsewhere.[51]

4.4 Track Selection for the K^0 and Λ Search

The tracks used for construction of secondary vertex candidates were subjected to six tests: four related to track quality, and two designed to separate out those tracks which do not come from the primary vertex. The first four selection criteria are deliberately set loosely to accept as many tracks as possible while holding to accepted standards of track quality. The final two track cuts provide the powerful background suppression.

It should be noted here that backgrounds in the first stereo superlayer of the drift chamber caused mismeasurement of the z position of tracks in the 91 GeV data.[52] Since this effect was not well-modelled in the Monte Carlo, the 91 GeV data and Monte Carlo were retracked without the first stereo layer.

4.4.1 Requirement on Angle to z Axis

The first of the cuts on track quality is a cut on the angle the track makes with the beam axis. This cut is imposed to make sure the track passes through enough layers of the drift chamber to be well-measured. A track with $|\cos\theta| = 0.82$ will pass through five superlayers of the drift chamber, which should give enough information to allow for well-measured momentum. Figure 23 shows the $|\cos\theta|$ distribution for tracks in the data and the Monte Carlo; the number of tracks found drops off drastically for values of $|\cos\theta| > 0.8$. The cut is made at $|\cos\theta| = 0.8$ because the efficiency outside this region differs between the Monte Carlo and the data.

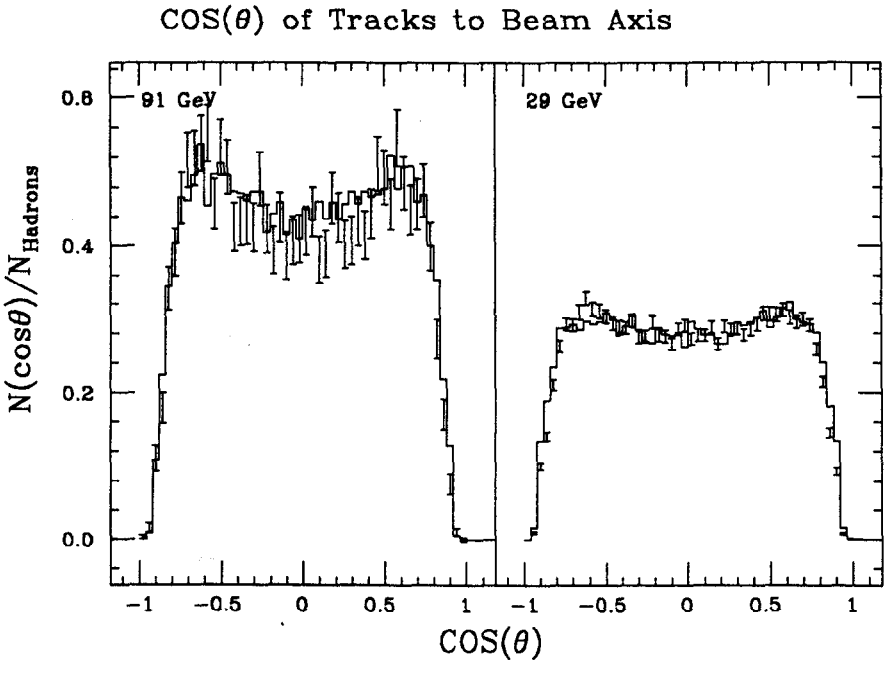

FIGURE 23. Distribution of tracks in $\cos\theta$ at 29 GeV and 91 GeV. The points represent the distribution for the data, the solid histograms represent the distribution in Monte Carlo. All plots are normalized to the number of hadronic events. The 91 GeV plot has larger values owing to the fact that the track multiplicity in hadronic events is higher.

4.4.2 Transverse Momentum Cut

Owing to the magnetic field in the drift chamber, tracks with low momentum will spiral without leaving the drift chamber volume. The momentum on these tracks is generally not well measured. The value of transverse momentum at which tracks make the transition between spiralling upon themselves and escaping the drift chamber is 0.1 GeV at 29 GeV and 0.11 GeV for the Z^0 data. This difference is due to the fact that the magnetic field was higher for the SLC running than for the PEP running. In order to ensure that all tracks are well-measured, the transverse momentum was required to be greater than 0.11 GeV. Figure 24 shows the data and the Monte Carlo distributions for transverse momentum. The efficiency for detecting tracks is small below 0.1 GeV.

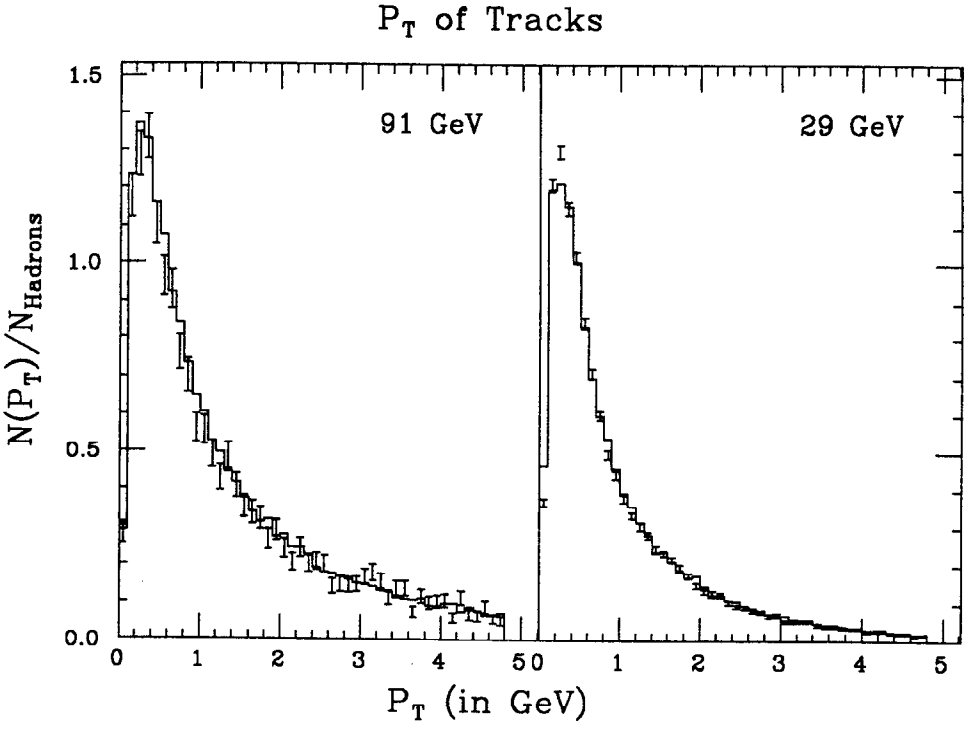

FIGURE 24. The transverse momentum distribution of tracks at 29 GeV and 91 GeV. The points represent the data and the solid histogram represents the Monte Carlo. All distributions are normalized to the number of hadronic events.

4.4.3 Fiducial Volume in z

Tracks originating far out in z tend to be mismeasured. The interaction point is defined to be $z = 0$, and most tracks should come from the interaction point. Of course, remote decays such as K^0_S and Λ decays can lead to tracks missing the interaction point by a large amount. However, if the impact parameter in z is large, this indicates that the plane of the decay is near the $r-z$ plane, giving little impact parameter or opening angle in the $r-\phi$ plane. Such remote decays will be difficult to reconstruct owing to the poor z resolution of the chamber. So to eliminate these poorly measured tracks, all tracks were required to extrapolate to within 10 cm of the interaction point in z. This is a looser cut on the fiducial volume than those used in the hadronic event selection; the reason for this discrepancy is that in the K^0 and Λ search the tracks are supposed to miss the interaction point, and signal would be lost with a tighter cut on the z fiducial volume. Figure 25 shows the distribution of signal and background tracks in z for both the SLC and PEP data. The mismatch apparent between Monte Carlo and data is due to slightly better z resolution in the Monte Carlo, arising from imperfect simulation of backgrounds and inefficiencies. This discrepancy will be treated in the discussion of systematic errors in the next chapter.

4.4.4 Number of DAZMs

The measurement made by a wire in the drift chamber of the position of a passing charged particle is called a DAZM. A track must have a minimum number of DAZMs in order for a good fit to be made to its position and momentum. The cut made on $|\cos\theta|$ ensures that charged particles will have traversed at least five superlayers of the drift chamber, which with perfect efficiency would give all tracks at least thirty DAZMs (six per superlayer). However, all wires do not necessarily produce a signal with the passage of a charged particle, nor does the tracking algorithm always correctly assign hits to tracks. Therefore an additional requirement is made on the tracks: that they have at least twenty-four DAZMs.

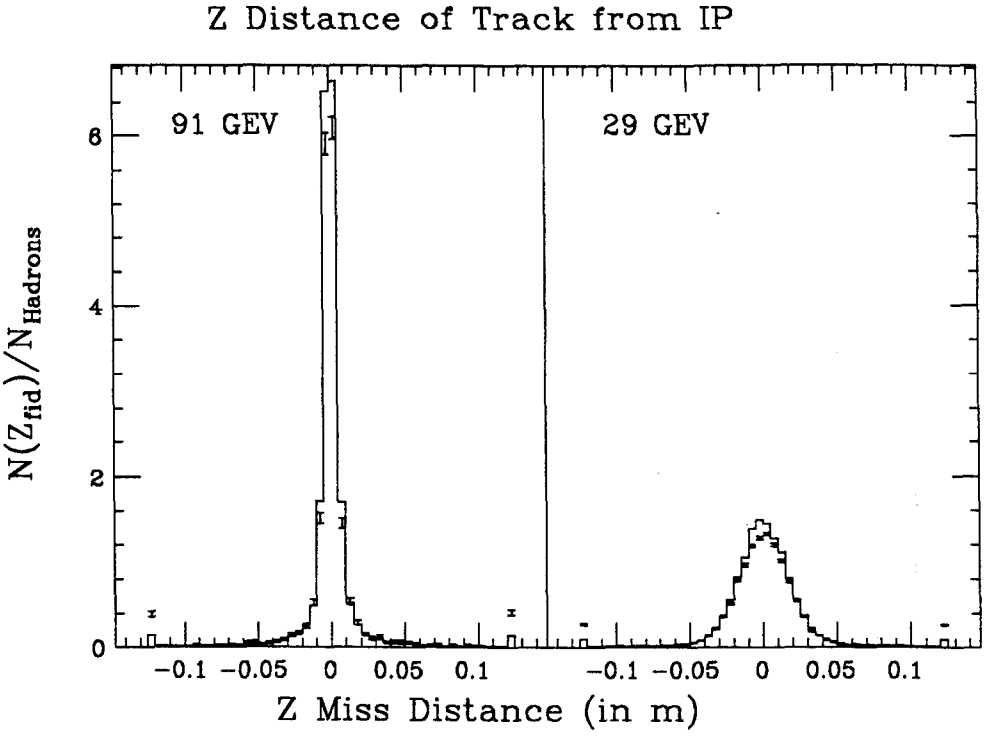

FIGURE 25. Distribution of miss distance in z of tracks from the interaction point, for both 29 GeV and 91 GeV. The points represent the data and the solid histogram represents the Monte Carlo. Both are normalized to the number of hadrons.

This allows for a 20% inefficiency in both the drift chamber electronics and in the tracking algorithm, but leaves enough hits on the track to ensure that the found track probably corresponds to a real charged particle passing through the detector. Figure 26 shows the number of DAZMs per track after the imposition of the $|\cos\theta|$ cut. Note that the 29 GeV distribution has a larger maximum: this is because of the presence of the vertex chamber during the data-taking at 29 GeV.

Again, the Monte Carlo shows slightly better distributions than the data, caused by imperfect simulation of backgrounds which confuse the tracking and by possible discrepancies in cell inefficiencies. These discrepancies will be taken into account in the chapter on systematic errors.

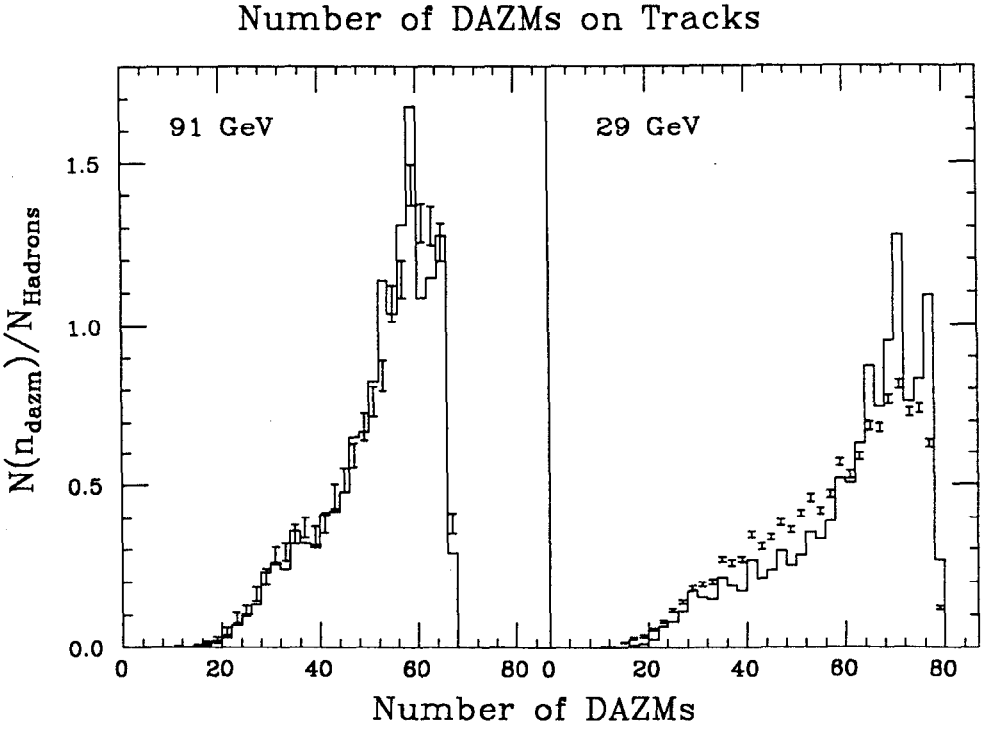

FIGURE 26. The distribution of number of drift chamber hits per track at 29 GeV and at 91 GeV. The points represent the data and the solid histogram represents the Monte Carlo. The maximum number of hits per track is higher at 29 GeV owing to the presence of the straw-tube vertex chamber.

4.4.5 Cuts on Miss Distance of Tracks from Vertex

The most important cuts for reducing backgrounds to the K^0 and Λ signals were the requirements on miss distance from the vertex. Because the z resolution of the chamber is much worse than the resolution of position in the $r-\phi$ plane, the miss distance of tracks was calculated only in the $r-\phi$ plane. The miss distance was defined as the perpendicular distance from the measured interaction point to a tangent of the curve. It is called the distance of closest approach (DCA). As Figure 27 shows, the signal and background differ greatly in the distribution of distance of closest approach of the track to the vertex. In order to reduce background as much as possible while keeping the efficiency large, the cut was set at the 1.0 mm, where the background curve begins to level out.

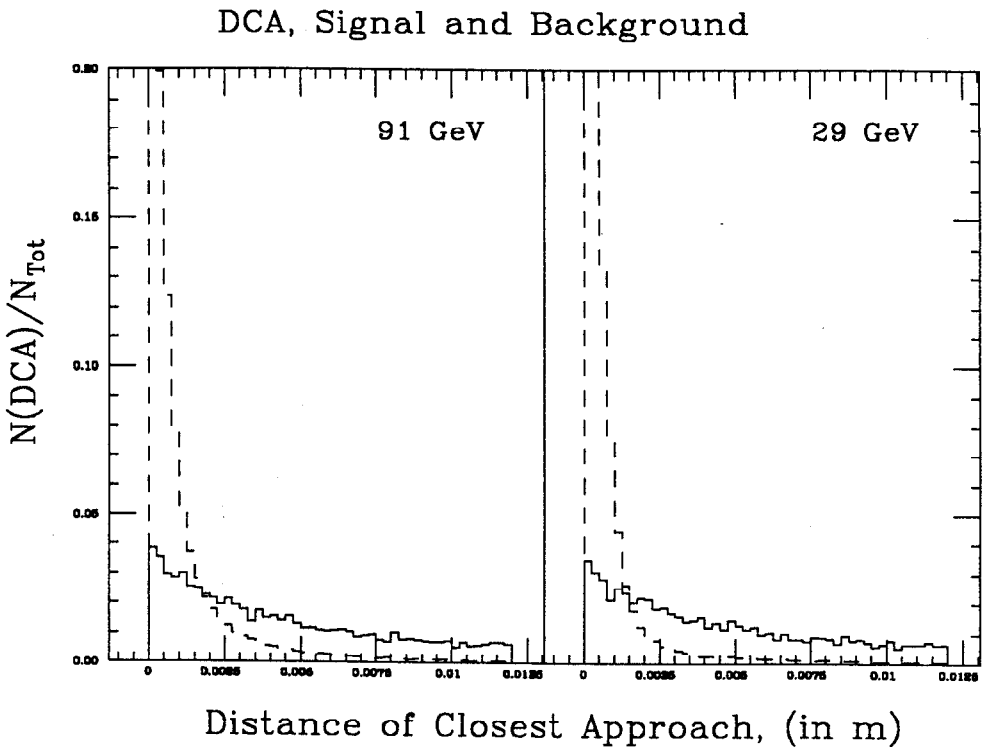

FIGURE 27. The distance of closest approach of tracks to the interaction point is shown for both signal and background at both 29 GeV and 91 GeV. These distributions are made with tagged signal and background events from the Monte Carlo simulations. The solid histogram represents the signal, while the dashed histogram represents the background. A large fraction of the signal (about 1/3) is in the high tail of the distribution not shown in this graph, whereas the background has virtually no tail in that region.

Unfortunately, as Figure 28 shows, the width of the distribution of the distances of closest approach depends on the track momentum. Low momentum tracks are bent more by multiple scattering in the beam-pipe and inner walls of the detector, so that when they are extrapolated back to the interaction point, they appear to originate at a point away from the primary vertex. Because of this effect, it is necessary to require tracks to miss the vertex by a greater distance if they have low momentum.

This is accomplished by imposing a cut on transverse momentum times distance of closest approach. The distributions for this variable are shown in Figure 29. The tracks were required to have $p_T \cdot DCA > 0.002$ GeV·m. This cut

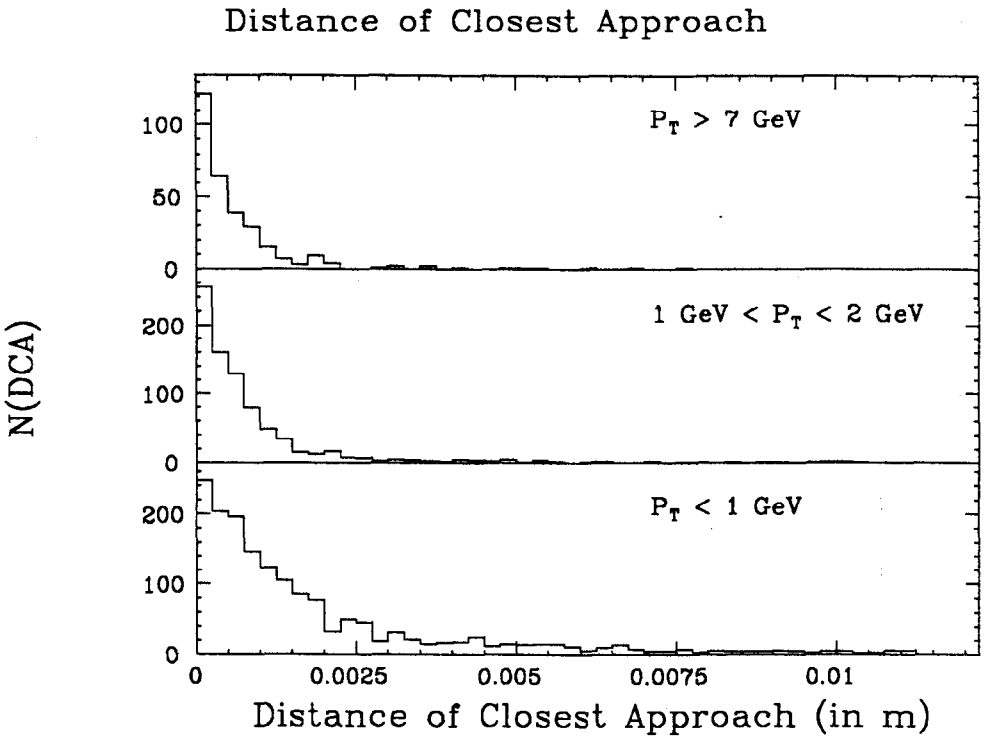

FIGURE 28. This figure shows distributions of the distance of closest approach of tracks to the interaction point for tracks with momenta below 1 GeV and for tracks with momenta above 7 GeV. These distributions were made from the Z^0 resonance data. Multiple scattering severely reduces the resolution on distance of closest approach for the low momentum tracks.

has no effect for tracks with $p_T > 2.0$ GeV, since for those tracks the requirement on distance of closest approach alone is more restrictive.

Figure 30 shows scatter plots of signal and background tracks from Monte Carlo events generated at 91 GeV. The points are plotted with their p_T and distance of closest approach. The solid line shows the areas eliminated by the cut on $p_T \cdot DCA$; the dashed lines show those areas eliminated by other cuts.

4.5 Selection Criteria for Vertex Candidates

When an oppositely charged pair of tracks passes the track selection described above, the vertex or vertices that they form are subjected to vertex selection criteria. The tracks are treated as arcs of circles and the two intersection points of the circles are found. The intersections that are within the detector are

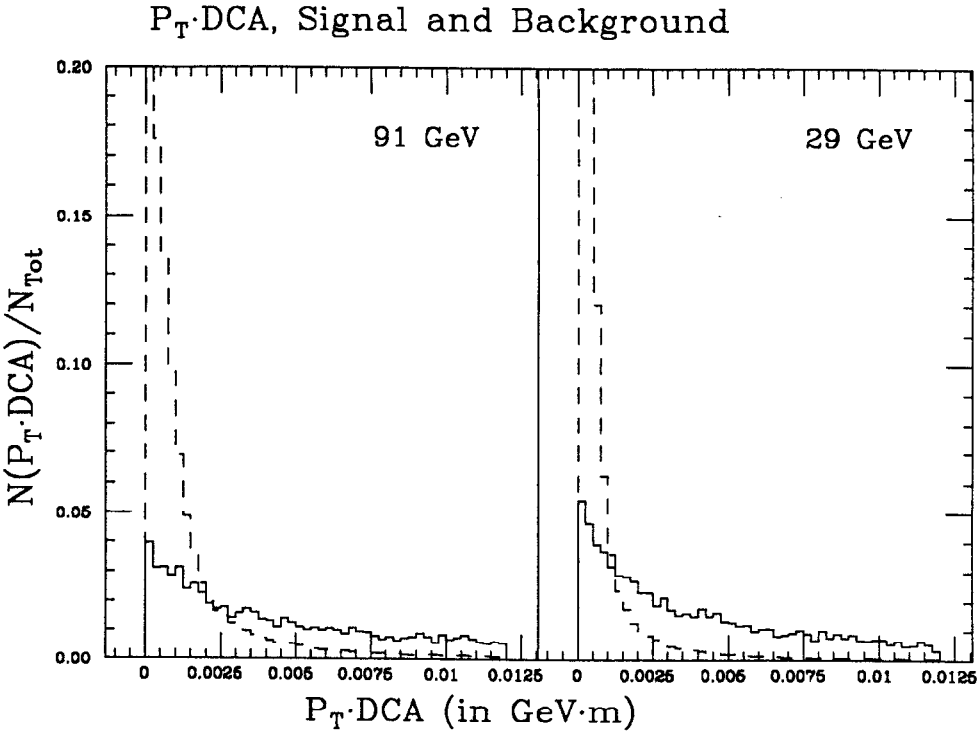

FIGURE 29. Distributions of $P_T \cdot DCA$ for signal and background tracks, for 29 GeV and 91 GeV. The distributions were made with tagged signal and background tracks from the Monte Carlo simulation. The signal distribution is shown with a solid histogram; the background distribution is shown with a dashed histogram. The signal distribution has a large tail in values above the limit of the plot; this represents about a quarter of the signal. The background distribution has a very small tail in this area.

subjected to the vertex selection. The intersections are defined as the meeting points in the $r - \phi$ plane, because position resolution in z is poor. After these intersections are found, two basic cuts on the vertex quality are made initially: a cut on the distance in z between the two tracks at the intersection in the $r - \phi$ plane, and a cut on the angle between the position vector of the vertex and the combined momentum vector of the two tracks forming the vertex. Any vertices passing these criteria are subjected to loose invariant mass cuts before passing to more serious vertex processing, to be described later.

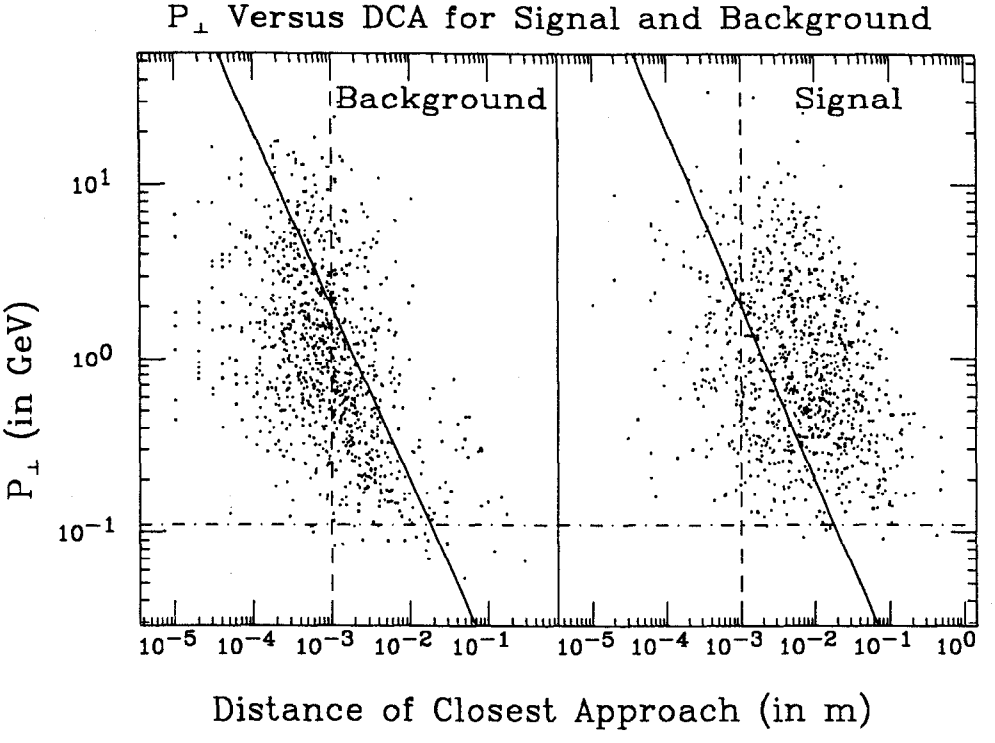

FIGURE 30. The distance of closest approach and p_T for one thousand signal and one thousand background tracks in the 91 GeV Monte Carlo. The solid line shows the $p_T \cdot DCA$ cut applied to the data to eliminate tracks with large impact parameter due to multiple scattering at low momenta. The dashed line shows the DCA cut, and the dot-dashed line shows the region eliminated by the p_T cut. Note that all tracks with distance of closest approach less than 1 mm or $p_T < 0.11$ GeV are eliminated by another cut.

4.5.1 Miss distance in z at Vertex

If a vertex candidate is really a kaon or lambda decay, one would expect the two tracks to come from the same place in z as well as in the $r-\phi$ plane. In order to eliminate bad vertex candidates, some cut on z miss distance (Δz) is needed. However, the z resolution of the drift chamber is significantly worse than the $r-\phi$ resolution, so the tracks can easily be sufficiently miss-tracked in z so as not to appear to come from one point in space. Also, the shape of the distribution of Δz is similar for signal and background, as can be seen in Figure 31. This similarity is due to the fact that the background tracks are also generally coming from one vertex, whether it be the primary vertex or other secondary decay vertices, and therefore should not have a large miss distance in z either.

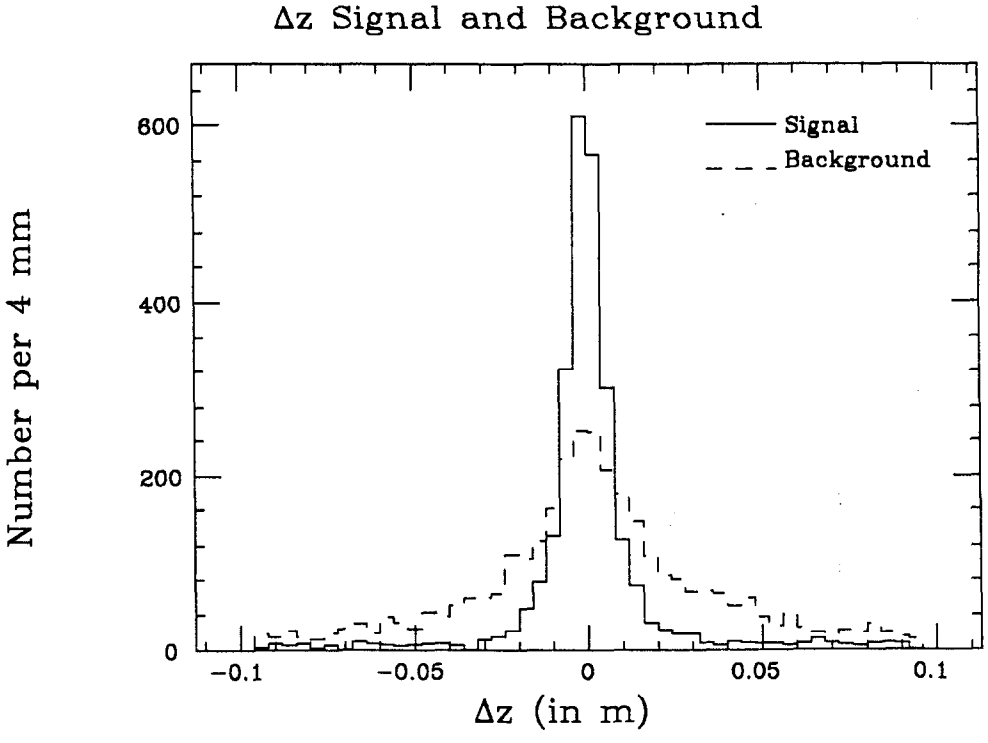

FIGURE 31. Distributions of z miss distance for all signal and background vertex candidates at 91 GeV which pass all previous cuts. The distributions were made from tagged signal and background tracks in the Monte Carlo. The solid histograms show the distribution for the signal, while the dashed histograms show the distribution for the background. The signal tracks in the wings are mostly from the second of two vertices formed by a given pair of tracks.

Because of the similarity between the signal and background distributions, the value of the cut was set fairly loosely, at 4 cm. The tails of the signal distribution which appear beyond this value are almost all from the wrong one of the pair of vertices generated by each pair of tracks: two curving tracks will cross twice in the $r-\phi$ plane, but if they have some opening angle in z they will be near each other at the true vertex but separate at the secondary crossing.

4.5.2 Angle Between Position Vector and Momentum Vector

A K^0_S or Λ generated in hadronization or in heavy quark decays which occur near the primary vertex should have a momentum vector which points directly away from the primary vertex. For this reason, the alignment between the position vector of a vertex candidate and its momentum vector can be a useful

test of whether it is a good vertex. Here the position vector is defined as the vector from the interaction point to the secondary vertex, and the momentum vector is defined as the summed momentum vector of the two tracks making up the secondary vertex, as shown in Figure 32.

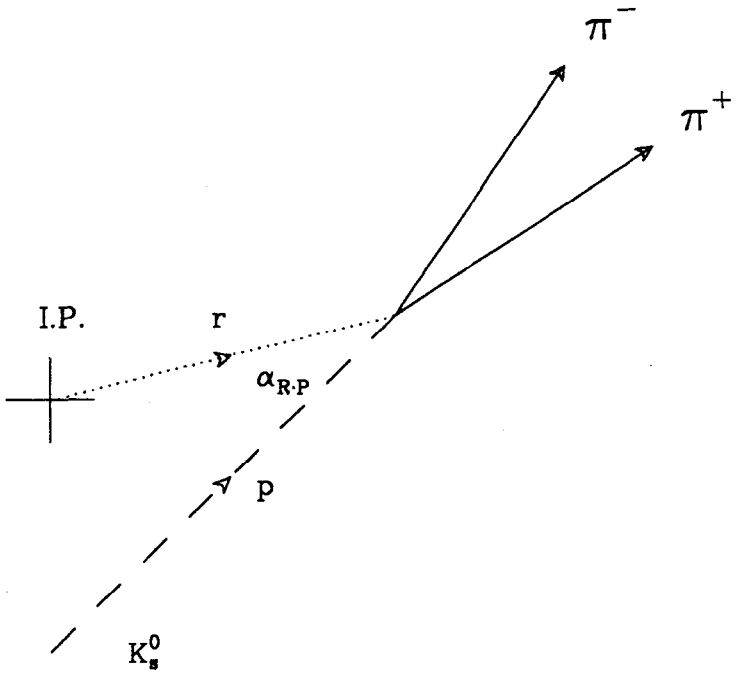

FIGURE 32. The angle between the position vector of a remote vertex and its momentum vector. The vectors are defined in the $r - \phi$ plane. This angle should be very small for real K^0 and Λ from the primary vertex.

The quantity chosen for discrimination is the cosine of the angle between the position vector and momentum vector, denoted here by $\cos\alpha_{r\cdot p}$ Figure 33 shows the distributions of $\cos\alpha_{r\cdot p}$ for signal and background.

Both signal and background distributions peak at $\cos\alpha_{r\cdot p} = \pm 1.00$; however, the signal distribution peaks much more strongly and very little of the signal appears below $\cos\alpha_{r\cdot p} = 0.99$. Some of the signal shows backwards correlation between the momentum and position vectors; this is due to the fact that one of the two vertices reconstructed from the two tracks is on the wrong side of the interaction point. To be classed as a good vertex, candidates are required to have $\cos\alpha_{r\cdot p} > 0.99$.

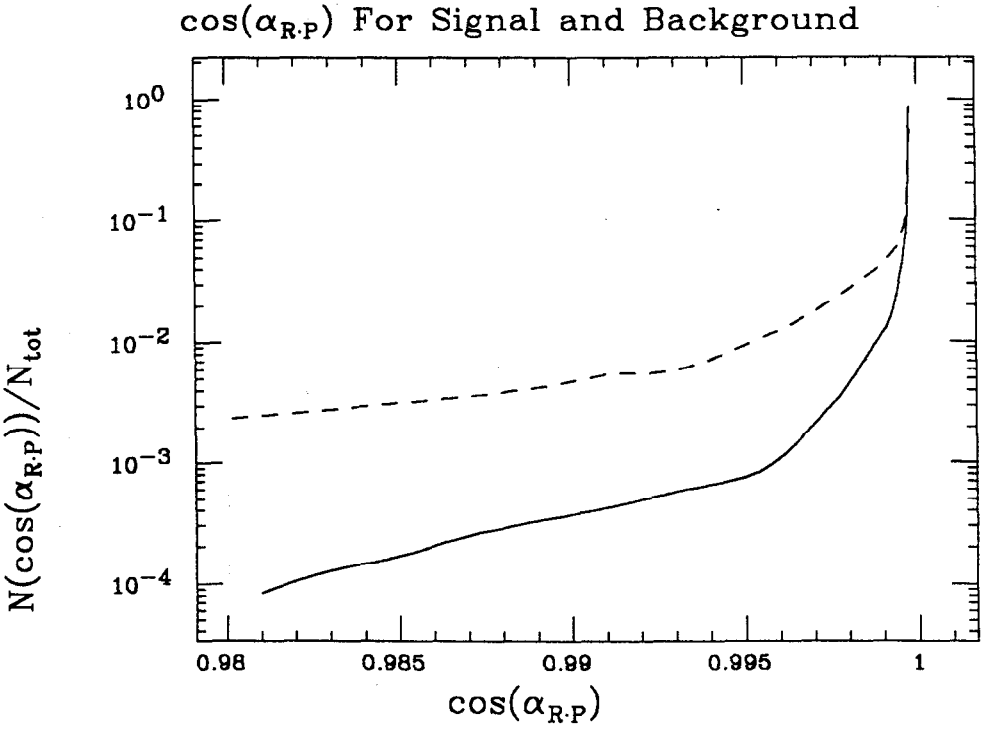

FIGURE 33. The signal and background distributions of $\cos\alpha_{r\cdot p}$ for 29 GeV and 91 GeV. All previous cuts have been imposed. The signal distribution is given by the solid line, the background distribution by the dashed line. Signal and background distributions are made from tagged Monte Carlo tracks.

4.5.3 First Level Mass Cuts

In order to reduce the volume of data to go through further processing, very loose cuts were made on the invariant mass of the vertex candidates. The possible invariant masses of every two-prong vertex that passes the previous selection criteria are calculated, allowing the track pair to be $\pi^+\pi^-$, $p\pi^-$, or $\bar{p}\pi^+$. All candidates which gave an invariant mass between 400 MeV and 600 MeV for the $\pi^+\pi^-$ hypothesis were kept as possible K^0_S, and all which gave an invariant mass between 1.08 GeV and 1.18 GeV for the other hypotheses were kept as possible Λ, for the $p\pi^-$ hypothesis, or $\bar{\Lambda}$, for the $\bar{p}\pi^+$ hypothesis.

4.5.4 Resolution of Ambiguities in Identification

Some of the vertex candidates remain as candidates for both K^0_S and Λ identification. At this point it must be decided whether the vertex is a probable K^0_S decay, a probable Λ^0 decay, or a probable $\bar{\Lambda}^0$ decay. Fortunately, there is no ambiguity between Λ and $\bar{\Lambda}^0$. However, K^0_S and Λ can be impossible to tell apart for certain decay kinematics without good particle identification; the particle identification in the Mark II proved to be no more helpful than discriminating between the candidate vertex identifications on the basis of their mass. Use of the particle identification is also subject to systematic errors, since the identification for protons and pions is only separated by a few sigma over most of the momentum range, and the Monte Carlo may not model the particle identification systems well. Discriminating between K^0_S and Λ can be done by assigning the identification which has a mass for the vertex closest to the appropriate particle mass.

However, this method is very sensitive to small changes in the mass resolution; the worse the resolution, the more vertices are misassigned. Therefore, the estimation of the amount of misidentification is dependent upon the agreement between Monte Carlo and data. In an effort to reduce possible errors, therefore, any vertex candidates which give a mass for the $\pi^+\pi^-$ calculation within 20 MeV of the K^0_S mass are identified as kaons. Since more kaons are produced than lambdas, these vertices are more likely to be kaons anyway; also, the misidentification background is proportionately smaller compared to the kaon signal. The misidentification that occurs through this method should not be dependent on Monte Carlo resolution; it should be determined by kinematics, since in the region of the K^0_S peak the background of lambdas is fairly flat. Vertices which fall outside the 20 MeV window for the kaon mass hypothesis are assigned to either the K^0_S candidates or the Λ candidates according to which hypothesis brings them closer to the appropriate mass.

4.5.5 Final Mass Calculation

Once the candidate vertices are found, corrections for dE/dx losses are made on the tracks, and the error matrices for the tracks are corrected for multiple scattering. Then a vertex-constrained fit is done on the two tracks. Any candidates for which the vertex-constrained fit gives a $\chi^2 > 16.0$ are dropped. This is a very loose cut on the χ^2; most signal events should have χ^2 less than 3.0, as shown in Figure 34; it is designed to eliminate only flagrantly bad candidates.

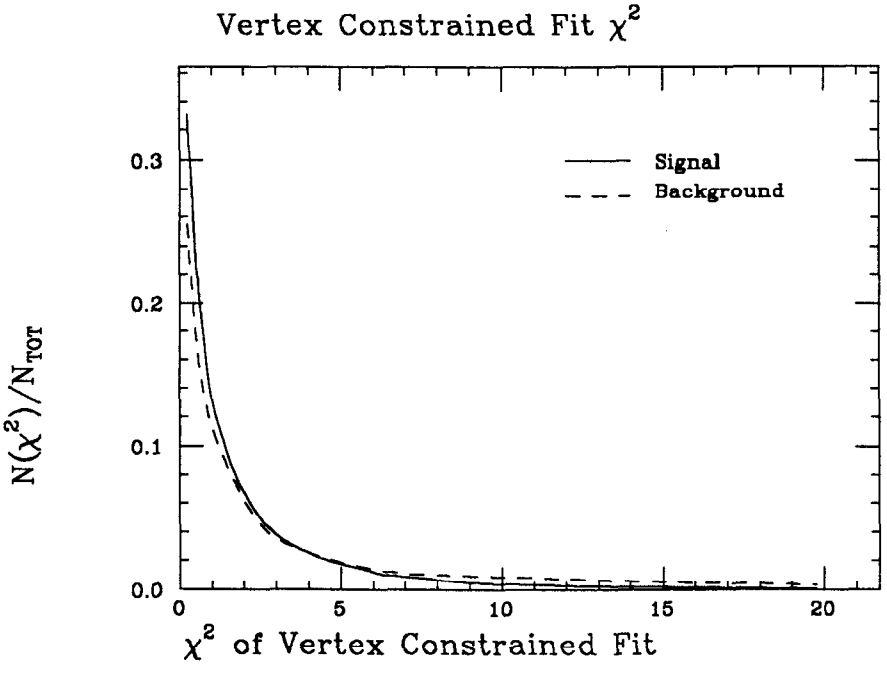

FIGURE 34. The distribution of χ^2 of the vertex-constrained fit for tagged signal and background vertices in the Monte Carlo.

The resultant distributions of signal events are shown in Figure 35a for the kaon mass calculation and in Figure 35b for the lambda mass calculation. As can be seen, the levels of background outside the peak regions are low. The fitted Gaussian widths of the peaks are small, and agree with the Monte Carlo within errors; however, the mass resolution for the data tends to be slightly larger than that for the Monte Carlo. This difference will be treated in the systematic error calculations. The mass resolution is worse in the 91 GeV data than in the 29 GeV

data; this is in part due to the lack of the straw chamber vertex detector, which improves both momentum and position resolution on tracks, and in part due to the high background levels present at the SLC, which degraded the tracking resolution somewhat.

The final mass cuts are placed at ± 20 MeV from the expected mass for the particle, 0.4977 GeV for the K^0_S and 1.1156 GeV for the Λ. The two track vertices lying within these boundaries are those used for the remainder of the analysis, described in the next two chapters.

Table 8 shows the reduction of the data sample arising from the various cuts, for data, all Monte Carlo tracks, and just those Monte Carlo tracks coming from K^0_S and Λ. Here the hadronic event selection has already been done. The reductions for K^0 and Λ occur in tandem until the final mass cuts. The numbers of Λ and $\bar{\Lambda}^0$ found inside these mass cuts were equal within errors: 14 and 20 respectively in the 91 GeV data sample, and 152 and 160 respectively in the 29 GeV data sample.

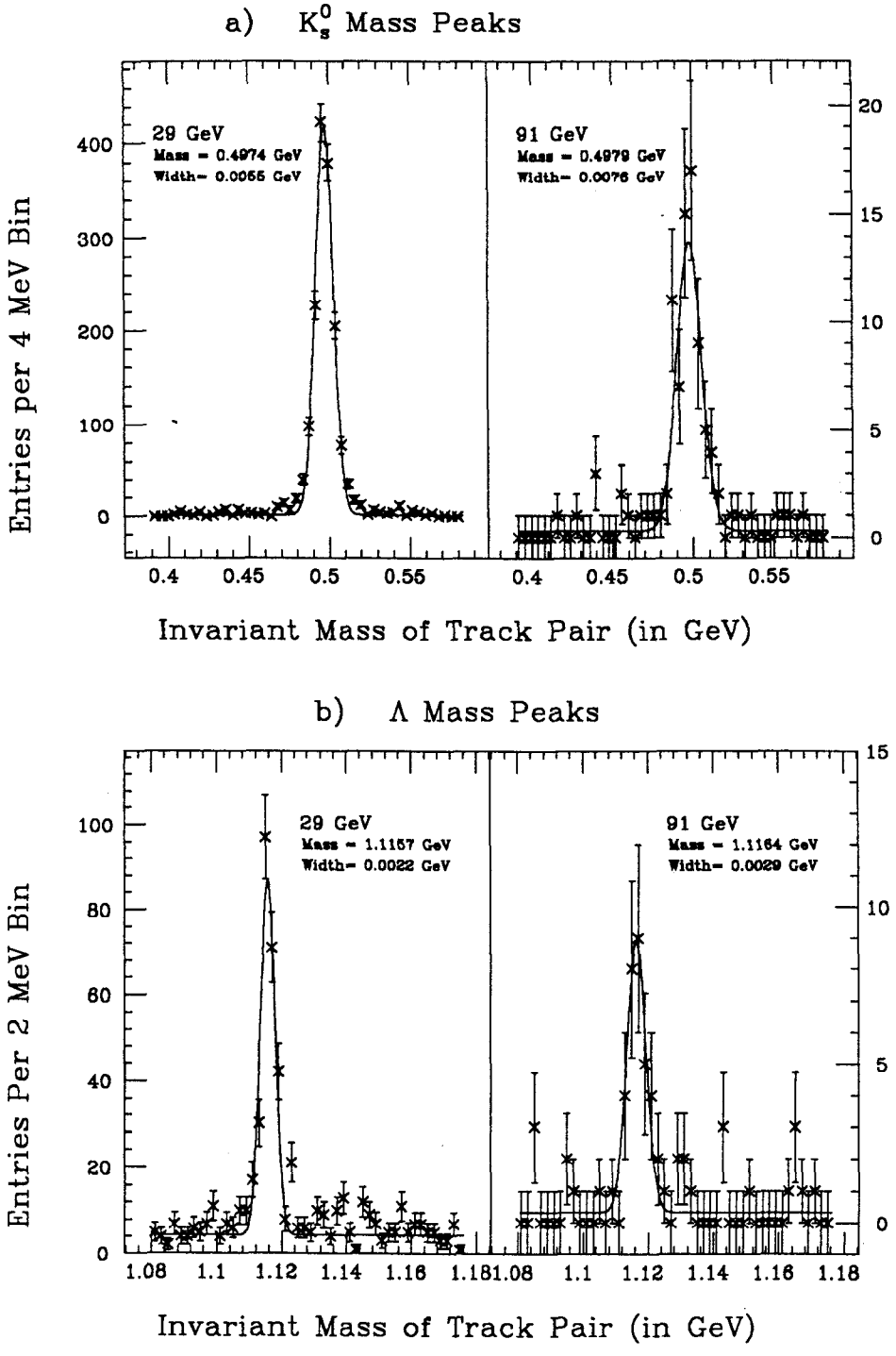

FIGURE 35. **a** shows the distribution of invariant mass for track pairs assuming both are pions; the K^0_S peak stands out clearly. **b** shows the invariant mass for track pairs assuming one is a proton and the other a pion, with the combined Λ $\bar{\Lambda}^0$ peak. The points are the data and the solid lines give the Gaussian fit to the invariant mass peak. The width is larger at 91 GeV due to poorer resolution from the lack of a vertex chamber and higher backgrounds.

TABLE 8. The numbers of tracks or vertices passing each cut, shown for data, general Monte Carlo data, and tagged K_S^0 and Λ in the Monte Carlo data.

	29 GeV		91 GeV	
Cut	Data	M.C.	Data	M.C.
Hadronic Events	8723		349	
Track Cuts	82,512	113,669	5585	119,970
$\cos\theta$	76,754	105,803	5367	114,224
p_T	74,403	102,990	5291	112,541
Z_{fid}	71,561	101,935	5074	110,875
N_{DAZM}	71,016	101,573	5009	109,829
DCA	20,807	25,985	1559	34,287
p_T·DCA	11,387	13,772	905	16,120
Vertex Cuts	9470	10,932	1169	17,715
Δz	5802	7260	716	11,354
$\cos\alpha_{rp}$	3079	4540	298	5679
First mass cut	2387	3740	164	3742
χ^2	2220	3560	148	3541
Second Mass Cut	1536,308	2544,622	73,34	2142,572

CHAPTER 5

CORRECTIONS AND ERRORS

The selection criteria described in the previous section give a nearly clean sample of K^0_S and Λ, but they also reduce the number of K^0_S and Λ in the signal. Before discussing the global properties of K^0 and Λ production in hadronic events, it is necessary to determine the real production rates from the signals found. This means that the loss of signal introduced by the lack of a perfect detector and the imposition of selection criteria must be corrected with efficiency calculations. Also, although the selection criteria are designed to give a nearly clean signal, some background events still pass the cuts. These backgrounds must be accounted for and removed from the signals to give an accurate estimate of the behavior of K^0 and Λ in hadronic events. All of these corrections can introduce systematic errors in the final calculations of K^0 and Λ production, which must be estimated in order to present accurate results. This chapter treats the background calculations, efficiency calculations, and error estimates used in deriving the final results on K^0 and Λ production.

5.1 Backgrounds

There are several types of backgrounds which affect the study of K^0 and Λ production in hadronic events. First, there are the backgrounds to the hadronic event sample itself, and then there are the backgrounds to the K^0_S and Λ sample within the hadronic events. The backgrounds to the hadronic event sample are of two kinds: backgrounds from physics processes and backgrounds from the machine environment.

5.1.1 Backgrounds to Hadronic Event Sample: Mimic Events

At both 29 GeV and the Z^0 resonance, the hadronic event sample must be separated from other types of events. The selection criteria used to do this were discussed in the previous chapter, along with the motivation for each cut. However, the two principle physics backgrounds which were discussed there are not completely eliminated by the selection criteria. These backgrounds are lepton pair events and two photon events, as pictured in the Feynman diagrams in Figure 21. Most lepton pair events are eliminated by multiplicity cuts, except for τ pair events, which can have high multiplicity.

These backgrounds have been estimated for both energy regions by previous analyses which originated the hadronic selection criteria used here.[24][50] The data sample used here for the 29 GeV study is slightly larger than that used in reference 24, so the results there are scaled to give the backgrounds in this hadronic event sample. Von Zanthier *et al* estimate that the fraction of the hadronic event sample passing cuts which comes from $\tau^+\tau^-$ backgrounds is $0.9\% \pm 0.4\%$. For the current hadronic event sample of 8723 events, this gives 78 ± 35 background $\tau^+\tau^-$ events. They also estimate that $1.0\% \pm 0.4\%$ of the final hadronic event sample comes from two-photon events which pass all the selection criteria, and $0.5\% \pm 0.3\%$ from high multiplicity Bhabha events. The background from beam-gas events was estimated to be less than 0.1%. This gives a total background in the hadronic event sample for the 29 GeV data of $2.4\% \pm 0.6\%$, or 209 ± 52 events.

The backgrounds to the hadronic event sample at 91 GeV were estimated from Monte Carlo and data by K. O'Shaugnessy *et al* in reference 50. The total backgrounds from beam-gas scattering, lepton pairs, and two-photon events are less than 0.5 event in the 91 GeV data sample.

5.1.2 Machine Related Backgrounds

In addition to events of other types which mimic hadronic events, further backgrounds in the hadronic event sample can come from machine-related noise which is superimposed on the hadronic event information in the detector. This was not a great problem at PEP, where the environment was fairly clean; random noise hits are added to events in the Monte Carlo in order to take into account any noise background at PEP.

At the SLC, however, machine related backgrounds pose a greater problem. Muons coming from upstream collimators pass longitudinally through the liquid argon, simulating photons; synchrotron radiation photons convert into low momentum curving tracks in the detector or local masses of charge, or light up the liquid argon calorimeter. In order to take into account such backgrounds, the Monte Carlo generated events are put through a full detector simulation and then combined with real data from random beam crossings collected at a time near that of the Z^0 decays. This technique is called "mixing" and gives a good picture of the effect of machine related backgrounds on the Z^0 data. After this combination, the mixed data are passed through the standard track and shower reconstruction routines used for the real data.

5.1.3 Backgrounds to the K^0 and Λ Samples

Within an established hadronic event sample, there exist backgrounds to a K^0 and Λ search. These are mostly from random combinations of tracks. Given any two tracks, there is some probability that their invariant mass is that of the K^0 or Λ. The distributions of invariant mass for all track pairs not from K^0 or Λ are shown in Figure 36, after all cuts have been imposed. As can be seen from the figure, the background is fairly straight through the regions around the mass peaks.

The contribution of this combinatorial background to the K^0 and Λ peak could be estimated from Monte Carlo. However, this would give rise to systematic

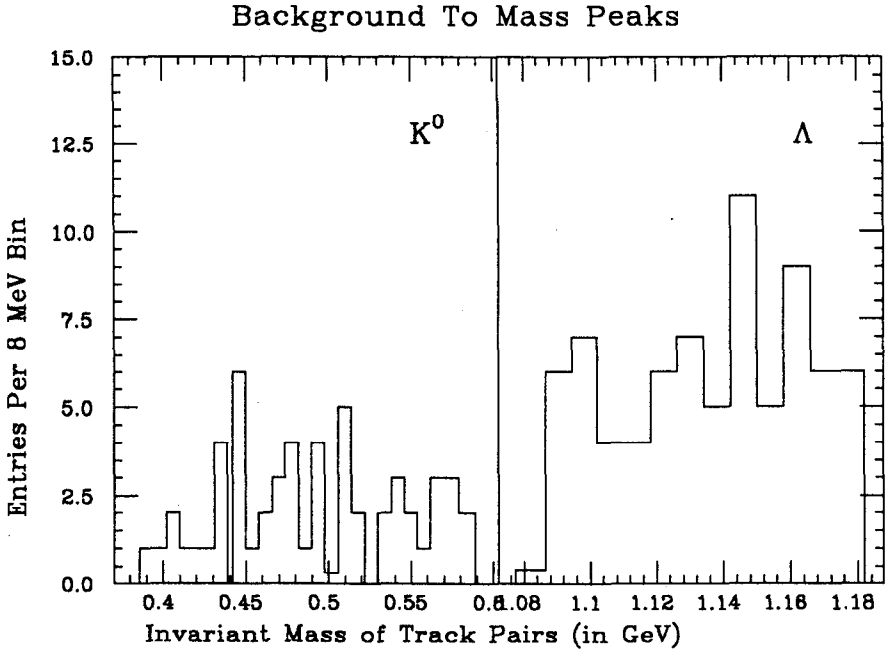

FIGURE 36. The distributions of invariant mass of random pairs of tracks in the regions of the signal show a fairly straight background through the K^0_S mass and a flat background above the Λ mass. These distributions represent tagged background tracks in the 91 GeV Monte Carlo.

errors, because a slight difference in the resolution on distance of closest approach or momentum times distance of closest approach could materially alter the amount of background creeping into the signal. Instead, this analysis uses the fact that the distribution of the combinatorial background is linear in the region of the mass peak to estimate the backgrounds. The technique used is to count the number of entries in the wings of the histogram over a 40 MeV wide region starting 20 MeV away from the bounds of the mass cut for the K^0 (20 MeV wide and 10 MeV away in the case of the Λ). This gives a good estimate of the number of background events per bin. This is multiplied by the number of defined signal bins to give the number of background events included in the sample passing all cuts.

Another sort of background to the signals is misidentification between the K^0 and Λ themselves when the decay kinematics make identification ambiguous. As stated in the previous chapter, discrimination on the basis of the difference between the pair mass and the appropriate particle mass is very sensitive to the

mass resolution and can be a large source of systematic error since Monte Carlos do not duplicate detectors exactly. The same is true of dE/dx and time-of-flight measurements.

In order to make the estimates of misidentification less dependent on detector simulation in the Monte Carlo, any track pair which is within 20 MeV of the K^0 mass (0.4977 GeV) is assigned identification as a K^0. Therefore some Λ are appearing in the K^0 peak. The number of Λ which give a mass near the K^0 peak if the tracks are hypothesized to be two pions does not depend much on resolution; instead, it is a kinematic effect, and should be well modeled by the Monte Carlo. Monte Carlo indicates that the amount of Λ misidentified as K^0 by this method is 20.6% of the amount of Λ identified as Λ at 29 GeV, and 27.1% at 91 GeV. The difference arises from the change in the momentum distributions of K^0 and Λ, which alters the kinematics of the decays.

There can still be K^0 for which the mass calculated is far enough off the peak that they are still misidentified as Λ. These, however, should be fairly evenly distributed across the invariant mass distribution for track pairs using the πp hypothesis, and should be taken care of by the background subtraction described above. This is estimated at 0.5% of K^0 at 29 GeV and 0.9% of K^0 at 91 GeV.

Table 9 shows the selected signals, together with their estimated backgrounds. The number of real K^0 found in the 29 GeV data is estimated to be 1442, and the number of real Λ found is estimated to be 245. At 91 GeV, the number of real K^0 found is 60, and the number of real Λ found is 28. These numbers must be corrected for the inefficiencies of the selection criteria to give the total number of K^0 and Λ in the hadronic data.

TABLE 9. The number of vertices in the signal region of the invariant mass distribution is given for both K^0 and Λ at 29 GeV and 91 GeV, together with the estimated backgrounds and the calculated signals of real K^0 and Λ.

No. in Signal Region	K^0, 29 GeV	Λ, 29 GeV	K^0, 91 GeV	Λ, 91 GeV
Total	1524	308	73	34
Background	31.4	63.0	5.2	6.0
Misidentified Λ	50.5	–	7.6	–
Calculated Pure Sample	1442.1	245.0	60.2	25.0

5.2 Efficiencies

The efficiencies of the selection algorithms were calculated by running the data selection algorithms on tapes of Monte Carlo generated events. The hadronic event selection efficiencies have been estimated in the papers in which the selection criteria originated. The efficiency for hadronic event selection is 0.77 ± 0.01 at 91 GeV and 0.637 ± 0.003 at 29 GeV.[24][50] These efficiencies are used only to calculate the corrected number of hadronic events in the sample; the effect of the hadronic event cuts on efficiencies for finding K^0 and Λ is determined separately.

For the calculation of efficiencies and correction factors for the K^0 and Λ samples, K^0 and Λ were tagged in Monte Carlo hadronic events and then run through the analysis, including the hadronic selection criteria. Thus, the efficiency for K^0 and Λ includes the inefficiency due to the fact that some hadronic events do not pass the hadronic event cuts: the corrected numbers of K^0 and Λ are those for all hadronic events. Also, both charged and neutral decay modes of K^0 and Λ are included in the initial tagged sample, so the neutral decay modes, which make up 31.39% and 35.7% respectively of the signals and are not visible to this analysis, are taken into account in the final corrections. In addition, the initial tagged K^0 sample includes both K^0_S and K^0_L; since the K^0_L decays are generally not visible in the detector and are not searched for in this analysis, this contributes a factor of

0.5 to the inefficiency. The correction factors for the K^0 compensate for this loss of information. All distributions are assumed to be the same for K^0_S and K^0_L since the two forms oscillate. The efficiencies quoted for Λ are for the combined Λ and $\bar{\Lambda}^0$ signals.

5.2.1 Loss of Efficiency from Lost Tracks

For both the K^0 and the Λ, a large part of the inefficiency results from the fact that the decay products are not visible in the detector. This can occur because of the neutral decay modes, or because of the K^0_l, as mentioned above. However, even for two-charged-prong decay modes of the K^0 or Λ, one or both tracks can be missed in the detector if they make too low an angle with the beam direction, are very low momentum, come from a decay too far out in the detector, or are lost through tracking inefficiency.

This loss of efficiency through failure to find both tracks coming from the decay vertex has been studied in Monte Carlo using a tagging routine which matches tracks found by the tracking routine with tracks generated in the Monte Carlo. This tagging routine bases the track-matching on the found track's DAZMs; that Monte Carlo track with which it shares the most DAZMs is considered its match. The validity of the match is tested by a χ^2 of the agreement between track parameters ϕ, dip angle, curvature, distance of closest approach, and z value at the distance of closest approach. If two found tracks both share a Monte Carlo track as a match, the Monte Carlo track is assigned to the found track which gives the smaller χ^2.

5.2.2 Intrinsic Loss of Efficiency

One of the chief sources of failure to find both tracks from a decay vertex is the finite fiducial volume of the detector in $|\cos\theta|$. The detector is fairly efficient out to $|\cos\theta| > 0.8$; however, the fiducial volume for detecting both tracks of a two prong decay is smaller, since one of the decay products is likely to appear at larger $\cos\theta$ than that of the original neutral track. This means that the region of

acceptance for reconstruction of the neutral track is smaller than that for finding charged tracks. Figure 37a shows the efficiency for finding both tracks from a neutral kaon decay as a function of $\cos\theta$. The efficiency falls off steeply above $\cos\theta = 0.6$; combined with the fact that the production of K^0 and Λ is peaked at $|\cos\theta| = 1.0$, as shown in Figure 37b, this geometrical effect leads to the largest loss in efficiency. Note that this loss in efficiency is entirely due to the detector's finite extension; the cut on the $|\cos\theta|$ of the tracks in the selection process has not been imposed yet.

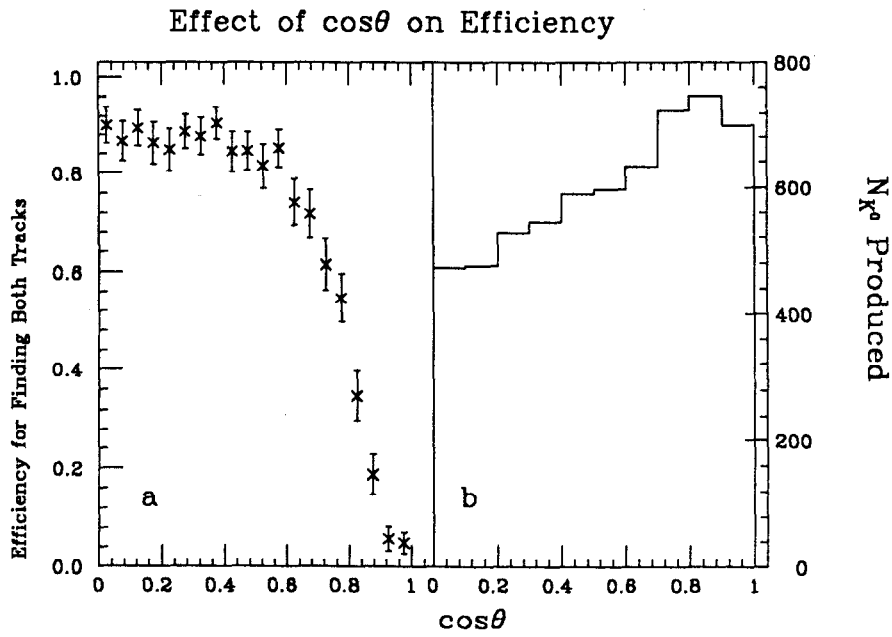

FIGURE 37. The dependence on $\cos\theta$ of finding both tracks from a K^0 decay together with the $\cos\theta$ dependence of K^0 production shows a large loss of efficiency due to the detector fiducial volume. No cuts have been made on the tracks yet. Distributions are shown for the 91 GeV Monte Carlo. Distributions for 29 GeV are similar.

Other sources of inefficiency for finding both tracks from the two-prong decays can include failure of the detector to differentiate the two tracks if they are too close together for the resolution of the drift chamber. This is not generally a problem, since most of the decays occur with a fairly large opening angle. Also,

since the two tracks from the decays have opposite charge, they will tend to separate in the drift chamber magnetic field and should be distinguishable.

If the parent neutral has low momentum, the decay products can have momentum too small for them to be found in the drift chamber. This is particularly the case for Λ, where the proton generally receives most of the momentum of the Λ, leaving the pion with little momentum.

For neutrals with very high momentum, $\gamma\beta c\tau$ is large, and the K^0 or Λ may decay very far out in the drift chamber. Table 10 gives the number of available DAZMs versus the radius at which the neutral decays; each superlayer can contribute six DAZMs to the track.

TABLE 10. The number of possible hits in the drift chamber for tracks from K^0_S and Λ decay, given the radius of the decay. Since the sense wires of the drift chamber are arranged in superlayers, the available number will decrease rapidly as the radius increases through a superlayer, and then remain constant over the space between superlayers. The values given are for the inner radius of a superlayer. The six sense wires in the superlayer are spaced by approximately 8.33 mm.

Decay Radius (cm)	Possible DAZMs
24.9	72
36.1	66
46.3	60
57.1	54
67.3	48
78.0	42
88.2	36
98.8	30
108.0	24

The decay products then traverse few layers of the drift chamber, so that tracking efficiency would be poor. This affects Λ more than K^0, because the Λ

has a longer decay length. It also affects the higher energy production more, since more of the K^0 and Λ have high momentum. Figure 38a shows the efficiency for finding both tracks from a K^0 decay depending on the radius at which the decay occurs. The efficiencies for Λ are similar. The efficiency peaks at about 0.2 m, and then begins to fall off. No tracks are found beyond 0.8 m. The distribution of the decay vertices in radius are shown in Figure 38b for K^0_S at 91 GeV. 95.3% of all K^0_S and 89.4% of Λ decay within 0.5 m in radius from the origin at 91 GeV. At 29 GeV, these percentages decrease to 98.6% and 94.8% respectively. A very small percentage of all K^0_S and Λ decay beyond the region of complete inefficiency: less than 0.3% for all cases.

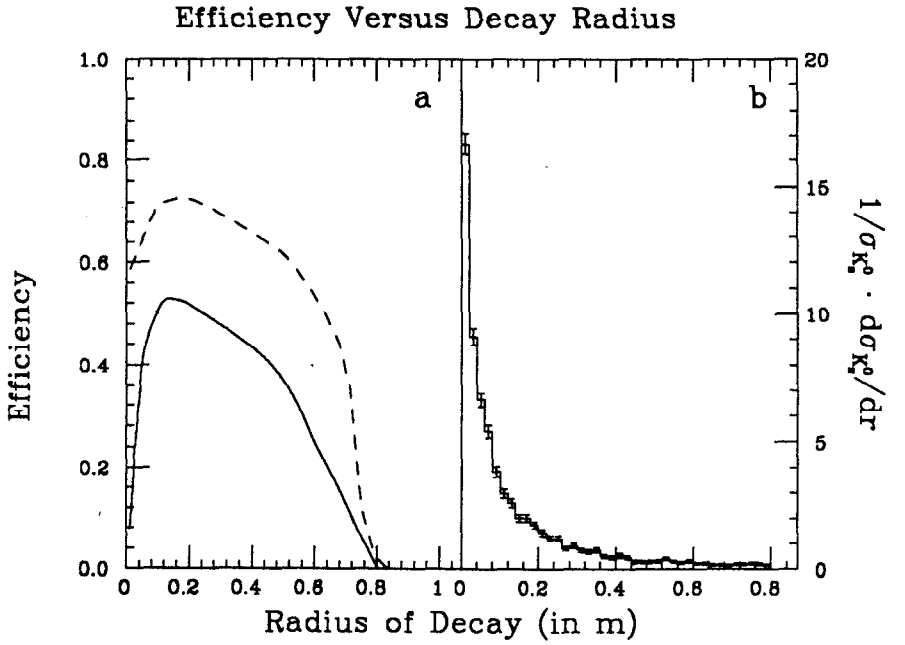

FIGURE 38. The efficiency for finding K^0 is shown as a function of the radius of the decay. The efficiency for finding both decay tracks is shown with the dashed line in **a**, while the efficiency for finding a K^0_S or from those tracks is shown with the solid line. The efficiency peaks at small radius and remains reasonably good out to 0.6 m, after which it falls of to 0.8 m. The radii of decay of the K^0 are shown in **b**. The efficiencies are shown for K^0 in the 91 GeV Monte Carlo.

The net effect of all these contributions, both from detector effects in tracking and from the non-visible decay modes, is to make only 0.185 of all K^0 and

0.33 of all Λ findable at 29 GeV, where "findable" is defined as having two tracks visible in the detector. At 29 GeV, 0.189 of all K^0 and 0.30 of all Λ are findable.

5.2.3 Efficiency Loss from Selection Criteria

Those K^0_S and Λ decays for which both tracks are found in the detector must pass the selection criteria, which further reduce the efficiency. Table 11 shows the reduction of the data sample arising from the various cuts, for data and all Monte Carlo tracks. Here the hadronic event selection has already been done.

TABLE 11. The numbers of tracks or vertices passing each cut, shown for signal and background tracks tagged in the Monte Carlo data for K^0 at 29 GeV and 91 GeV.

	29 GeV		91 GeV	
Cut	Signal	Background	Signal	Background
Track Cuts	13,502	129,299	6747	78,765
$\cos\theta$	12,387	113,727	6510	73,763
p_T	12,155	110,993	6444	72,790
Z_{fid}	11,941	110,581	6330	72,337
N_{DAZM}	11,888	110,336	6265	71,847
DCA	10,854	22,507	5636	19,973
p_T·DCA	9942	8184	5107	7195
Vertex Cuts	5216	2723	3025	3847
Δz	4448	1736	2427	2455
$\cos\alpha_{rp}$	4390	749	2375	910
First mass cut	4303	283	2285	306
χ^2	4188	241	2244	272
Second Mass Cut	4084	18	2072	24

The four track quality cuts somewhat reduce the efficiency. However, the major loss of efficiency comes from the two cuts on the distance of closest approach, which are the main criteria used to reject background. Both distance of closest approach and transverse momentum times distance of closest approach are peaked near 0 for the signal as well as the background, as can be seen from Figures 29and 27 from the last chapter. The cuts on the z distance between the tracks at the vertex in the $r-\phi$ plane and on $\cos\alpha_{rp}$ (the cosine of the angle between the momentum vector of the neutral and the vector from the origin to the decay vertex of the neutral) do not remove as many real K^0_S and Λ as would appear from the table; many of those vertices failing these cuts are the second of two which can be made from a single pair of tracks, and are thus backgrounds to the signal. Most of those K^0_S and Λ candidates removed by the $\cos\alpha_{rp}$ cut are from this second vertex forming behind the origin, so that the momentum and vertex position vectors are anti-parallel: the $\cos\alpha_{rp}$ distribution is very strongly peaked at ± 1.00 for real signal events.

The cut on $|\cos\theta|$ in effect further reduces the fiducial volume for tracks from K^0_S and Λ decays, but not by much, since the efficiency for finding tracks beyond the cut falls off quickly anyway. The efficiency falls off rapidly above $|\cos\theta| = 0.6$, and remains steady until that point; it follows closely the efficiency for finding both tracks from the decay, shown in Figure 37. This should affect most kinematic distributions evenly.

The cut on z_{fid} likewise should affect most distributions the same way, except that some decays which occur far out in the chamber could fail this cut. The cut on N_{DAZM} also is most likely to reduce efficiency for decays which occur far out in the chamber, which will tend to be from high momentum neutrals; however, this effect is already absorbed by the failure of the tracking algorithm to find tracks which are that far out in the chamber. It is difficult to assess this effect exactly, as it requires a great amount of Monte Carlo, but Figure 38a indicates that the efficiency for finding the decay vertices when both tracks are found remains reasonably good

over half the radius of the drift chamber. This distribution is also heavily dependent on the momentum dependence of the efficiency, since decays which occur at larger radius generally come from high-momentum tracks.

The cuts which most affect the kinematic dependence of the efficiency are the cuts on distance of closest approach and momentum times distance of closest approach. The requirement that the distance of closest approach be greater than 1 mm will eliminate decays which occur near the primary vertex of the event. All K^0_S and Λ tend to decay near the origin, but since the mean decay distance is related to $\gamma\beta c\tau$, the lower momentum tracks will decay closer to the origin. This means a greater loss of efficiency for low momentum tracks. However, although the higher momentum tracks tend to decay at larger distance, the opening angle between their tracks is smaller than that for low momentum tracks, so that they can also fail the distance of closest approach cut.

The cut on transverse momentum times distance of closest approach also reduces efficiency for finding low momentum K^0_S and Λ. It cannot affect any neutral with momentum greater than 2 GeV, so it does not affect the higher end of momentum distributions. The distribution of efficiency *versus* momentum is shown in Figure 39.

The vertex cuts only affect kinematic distributions inasmuch as the quality of the tracking is dependent on momentum; high momentum tracks have a greater momentum spread and a larger width on the mass distribution, and are thus more likely to appear in the tails of the distribution and be eliminated by the final mass cuts, whereas low momentum tracks which multiple scatter badly can miss the cuts on Δz and $\cos\alpha_{r\cdot p}$ or have an opening angle so mismeasured that they fail the mass cuts also.

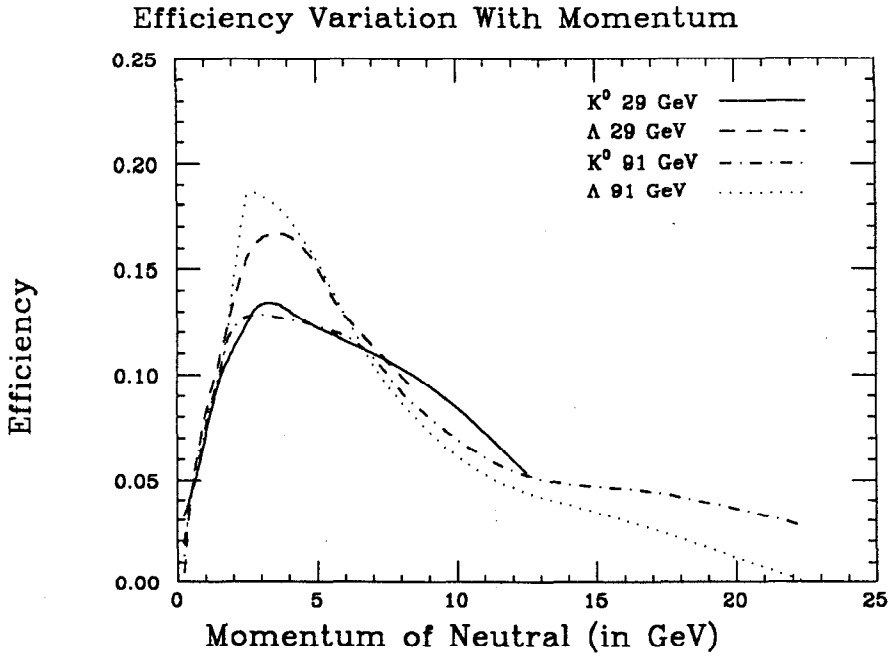

FIGURE 39. The dependence of efficiency on momentum is shown for both K^0 and Λ. These efficiencies are taken from the 29 GeV Monte Carlo. The 91 GeV dependence will be slightly shifted owing to the change in magnetic field in the drift chamber.

5.3 Correction Factors for Kinematic Distributions

Since the efficiencies are strongly momentum dependent, it is necessary to correct kinematic distributions for the effects of inefficiency in order to give an accurate picture of K^0 and Λ production in hadronic events. For variables which are not altered much by the detector simulation in the Monte Carlo, this can be done on a bin-by-bin basis. The kinematic distributions studied here should not be affected much by detector simulation; there will be some smearing of momentum but not enough to be a significant effect. Therefore corrections are done on a bin-by-bin basis by calculating the number of produced K^0 and Λ in each bin in Monte Carlo before putting the Monte Carlo events through the analysis to see how many are found in a given bin. The results of this procedure give a correction factor for each bin for a given kinematic variable x:

$$C(x) = \frac{n_{gen}(x)/N_{gen}}{n_{det}(x)/N_{det}}$$

Here n_{gen} is the number generated in Monte Carlo in a given bin in x, N_{gen} is the total number generated, n_{det} is the number detected in the x bin for the same Monte Carlo, and N_{det} is the total number detected. This correction factor gives a distribution normalized to the total number of K^0 or Λ. For the kinematic distributions, the correction factors included the backgrounds, since proportions of background events in the data agreed within errors with those from the Monte Carlo. In order to obtain the distributions normalized to the number of hadrons, N_{gen}^{had} and N_{det}^{had} are substituted for N_{gen} and N_{det}. Then the corrected distributions are given by

$$n_{cor}(x) = C(x)n_{observed}(x)$$

or

$$n_{cor}(x) = C^{had}(x)n_{observed}(x)$$

where $n_{observed}(x)$ is, of course, the number of data points in that bin. Errors introduced by making these corrections will be discussed later.

5.4 Radiative Corrections

It is customary to discuss results of K^0 and Λ measurements at a given energy as if all hadronic events were generated at that energy, whereas in e^+e^-colliders initial state radiation brings many of the e^+e^-interactions down to lower energy. Therefore it is necessary to make radiative corrections to the data for purposes of comparison with results from other experiments at other machines.

At the Z^0 resonance, initial state radiation has little effect; when an initial state photon carries away any substantial fraction of the collision energy, the e^+e^-annihilation no longer occurs near the resonance and the cross-section for production of hadronic events becomes small. Likewise, for energies above the resonance, most of the hadronic events occur for e^+e^-pairs which have radiated photons to bring them down to the Z^0 mass. Therefore one can be reasonably assured that all hadronic events seen were actually produced at the Z^0 resonance.

At 29 GeV, however, initial state radiation can be quite a large effect. Pairs of electrons and positrons which have emitted an initial state photon interact in a region of higher cross section than they would without the initial state radiation. The visible cross section is

$$\sigma_h = \sigma_0(1 + \delta_h)$$

where σ_0 is the Born level hadronic cross section, which does not include higher order QED corrections. These radiative corrections are contained in the correction factor, δ_h. This increases the number of hadronic events produced for a given luminosity. However, the hadronic events are occurring at lower center-of-mass energy so that there is less energy available for hadronization, which will tend to lower the production of strange particles in hadronic events.

The effect of initial state radiation on the data is taken care of by running Monte Carlo with and without the Lund simulation of state radiation, and making a bin by bin correction of the number of produced K^0 or Λ per hadronic event. Table 12 shows these radiative corrections as a function of momentum.

5.5 Estimation of Errors

There are many factors that can contribute to errors in this measurement. Statistical errors are obvious, and are treated as the square root of the numbers used in calculations. The calculation of the corrections to the data, however, can introduce systematic errors, which it is the goal of this section to estimate. All corrections to the data are made from Monte Carlo; therefore the accuracy of these correction is dependent upon the accuracy with which the Monte Carlo reproduces the physics of event production and detection.

Firstly, it has been shown that the efficiency for K^0_S and Λ detection is strongly dependent upon the momentum at which those neutrals are produced. Therefore, if the Monte Carlo used to estimate efficiency has a momentum distribution which differs a great deal from the data, the efficiency calculated can

TABLE 12. The radiative corrections to the number of K^0_S and Λ per hadronic event for various momentum bins of the strange particle. The corrections are listed for both 29 GeV and 91 GeV data; the corrections to the 91 GeV data are much smaller, as explained in the text. Most of the corrections made to the data occur over larger momentum bins than those listed in this table.

Bin	K^0_S	Λ	K^0_S	Λ
0-0.5 GeV	0.949 ± 0.018	0.944 ± 0.068	1.019 ± 0.019	1.04 ± 0.08
0.5-1 GeV	0.920 ± 0.012	0.870 ± 0.036	0.981 ± 0.013	0.98 ± 0.04
1-1.5 GeV	0.939 ± 0.014	0.884 ± 0.036	0.991 ± 0.014	1.03 ± 0.04
1.5-2 GeV	0.960 ± 0.017	0.865 ± 0.039	0.981 ± 0.016	0.98 ± 0.04
2-2.5 GeV	0.927 ± 0.019	0.931 ± 0.046	0.980 ± 0.018	1.04 ± 0.04
2.5-3 GeV	0.997 ± 0.023	0.971 ± 0.051	1.002 ± 0.020	1.00 ± 0.05
3-4 GeV	0.921 ± 0.018	0.987 ± 0.044	0.993 ± 0.016	0.95 ± 0.03
4-5 GeV	0.957 ± 0.024	0.915 ± 0.045	1.012 ± 0.019	1.03 ± 0.04
5-7 GeV	0.914 ± 0.023	0.855 ± 0.039	1.013 ± 0.016	0.95 ± 0.03
7-10 GeV	0.825 ± 0.032	0.806 ± 0.052	0.999 ± 0.016	1.00 ± 0.03
10-15 GeV	0.718 ± 0.083	0.060 ± 0.100	0.963 ± 0.017	1.03 ± 0.04
15-20 GeV	-	-	1.020 ± 0.027	0.98 ± 0.05
20-25 GeV	-	-	0.975 ± 0.031	0.87 ± 0.04

be incorrect. In order to estimate this effect, the parameters of the Monte Carlo hadron production are varied to alter the distributions. These hadronic events with different momentum distribution are used to calculate efficiencies, and the difference in the efficiencies is taken to be the systematic error due to production parameter tuning in the Monte Carlo. This error is estimated at 4% for 91 GeV data and 4% for 29 GeV data.

Secondly, the radiative corrections discussed above are not made to all orders, so that the ideal value of the correction may differ from that used. The radiative corrections were made with the Lund Monte Carlo initial state radiation

routine, which makes corrections to $O(\alpha^3)$. Von Zanthier *et al* have estimated the errors on the total hadronic cross section at 29 GeV owing to the neglect of higher orders in α as $0.3\% \pm 0.3\%$.[24] The effect on the strange particle production in hadronization will occur at a slower pace than the change in the total hadronic cross section; the $O(\alpha^3)$ change in the hadronic cross section is 19%, but the change in the strange particle production is $\sim 8\%$. Therefore the error on the measurements from the neglect of terms of order greater than α^3 is estimated to be 0.3% for the 29 GeV data.

At 91 GeV, the $O(\alpha^3)$ corrections to the strange particle production are less than 1%; the error on the measurement from the neglect of terms greater than α^3 should decrease also, owing to the resonance effect discussed above; in order to be conservative, the error in the radiative corrections is estimated to be the same as that for 29 GeV: 0.3%.

5.5.1 Systematic Errors Arising from Detector Simulation

The most significant source of systematic errors in these calculations arise from the fact that the detector simulation in the Monte Carlo is not perfect. Since the same algorithm is used for finding Monte Carlo data tracks and real data tracks, the differences would arise in the production of the data in the detector. Such effects as a failure to model noise well, or the random smearing of signals on drift chamber wires, or the single wire inefficiency, are the most likely sources of the differences between Monte Carlo and data. If the tracking efficiency for the Monte Carlo simulated data and the real data are not the same, the effect of the difference in tracking efficiency is squared in the efficiency for finding these two-prong decays. Similarly, if the resolutions of various parameters are incorrect in the Monte Carlo simulation, the tails of distributions upon which cuts are made will be different from those of the data, which will induce further error in the measurement.

In order to estimate the effects of these differences between Monte Carlo detector simulation and the true response of the detector to the passage of charged

particles, Monte Carlo and data are compared for each distribution upon which cuts are made in selecting the signal. The difference between the percentage eliminated in Monte Carlo and the percentage eliminated in the data is taken to be the systematic error for that cut. The systematic errors for the track cuts are included twice, those for the vertex cuts only once.

There are some correlations among the quantities cut upon. For instance, the amount of tracks found at large $|\cos\theta|$ is correlated to the number of tracks found with a small number of DAZMs, since the $\cos\theta$ of the track determines how many layers of the drift chamber it passes through. Similarly, if Monte Carlo has more tracks passing the distance of closest approach cut, these are most likely to be background tracks which will then appear outside the accepted region of other cuts designed to reduce backgrounds. In order to avoid this double counting, the four track quality cuts are compared after the preceding cuts have been made, but the cuts designed to separate signal and background are compared for distributions without imposing the previous cuts. This also aids in comparisons for the 91 GeV data, where after the first signal selection cuts are made (DCA and $p_T \cdot DCA$) the statistics are quite low and make comparison difficult.

The only exceptions to this procedure are made for the distance of closest approach and $p_T \cdot DCA$ cuts. Here a small difference in resolution on the impact parameter can greatly change the percentage of tracks which fail the cut. However, this affects primarily the background tracks, which come almost entirely from the primary vertex. Here a worsening of the resolution smears more tracks into the defined signal region. However, the tracks which come from K^0_S and Λ decays have a much flatter distribution of distance of closest approach and $p_T \cdot DCA$, so that almost as many are smeared out of the accepted region as are smeared into it, and the net effect of a resolution change on the efficiency is not large. In order to determine the error due to these two selection criteria, the differences between the percentage accepted in Monte Carlo and in data are multiplied by the ratio of

the signal slope to the background slope at the value where the cut is made; this corrects for the difference in the distribution shapes.

5.5.2 Errors from Track Quality Cuts

The distributions for data and Monte Carlo for the track quality cuts are shown in the last chapter, Figures 23, 24, 25, and 26. The track quality selection criteria are $|\cos\theta| < 0.80$, $p_T > 1.1$ GeV, $|Z_{fid}| < 0.1$ m, and $N_{DAZM} > 24$. The differences of acceptance on these distributions give an error of 0.04% per track for the $|\cos\theta|$ cut at 29 GeV, and 0.7% at 91 GeV; as can be seen from Figure 23, the Monte Carlo expects to find more tracks at large $|\cos\theta|$. The p_T distributions, as can be seen from Figure 24, agree quite well between Monte Carlo and data at both energies. Here the systematic error due to the p_T cut is 0.61% at 29 GeV and 0.05% at 91 GeV.

Agreement on the distributions of the number of DAZMs per track is not so good. Especially with the $|\cos\theta|$ cut turned on, the number of tracks with a small number of DAZMs is larger in the data than in the Monte Carlo. The fact that the $|\cos\theta|$ distribution shows more tracks at small angles for the Monte Carlo is strongly correlated with the depletion of DAZMs in the data. The error due to these discrepancies is calculated to be 2.8% for the 29 GeV data and 2.7% for the 91 GeV data.

The last distribution for track quality is that for the z fiducial volume, which measures whether the track passes close enough to the origin in z to be a good track. Here again the resolution in the data appears to be slightly worse than the Monte Carlo. The tracks far out in the wings in the data could be from cosmic rays and beam gas events; it is difficult to tell how much of the discrepancy is a real effect. The whole discrepancy shall be included in the error, which is calculated at 0.43% for the 29 GeV data and 0.34% for the 91 GeV data.

5.5.3 Distance of Closest Approach and $p_T \cdot DCA$

The cuts on distance of closest approach and $p_T \cdot DCA$ must be treated somewhat differently, as described above. The difference between the data distribution for DCA and that for the Monte Carlo is 3.85% at 29 GeV and 0.74% at 91 GeV. The Monte Carlo distribution of DCA for K^0_S and Λ, shown in Figure 27 of the last chapter, is used to estimate the error for the K^0_S and Λ efficiency: the ratio of the slope of the signal distribution in that region to the slope of the background distribution is multiplied by the difference in acceptance. This keeps the error from being overestimated due to the great difference between shapes of the distributions. The net effect is small: an error of 0.58% for the 29 GeV data and 0.11% for the 91 GeV data.

The same procedure was followed for the cut on $p_T \cdot DCA$. Here the discrepancy between data and Monte Carlo was 2.23% at 29 GeV and 4.07% at 91 GeV. Figure 29in the last chapter shows the distribution for this variable for K^0_S; the distribution for Λ is similar. The final error on the K^0_S and Λ efficiency is estimated at 1.32% for 29 GeV and 2.40% for 91 GeV.

5.5.4 Errors from Vertex Cuts

The first vertex cut made on the data is on the distance between the two tracks in z at their crossing point in the $r - \phi$ plane. Here again the agreement between data and Monte Carlo is not perfect: the Monte Carlo gives a better resolution in z. Since no cuts have been made on the tracks other than those used to assure reasonable track quality, most of the track pairs in this Δz distribution come from the primary vertex and should meet in z, thus giving a good measure of the accuracy of this parameter. The systematic error from using this parameter as a selection criterion is estimated to be 2.37% at 29 GeV and 2.17% at 91 GeV.

The second vertex cut depends on the alignment of the radius vector to the decay vertex with the momentum vector of the reconstructed neutral. For K^0_S and Λ from hadronization, these should line up well; for those from decay, the

alignment should still be fairly good if the original particle decayed near the origin, which is generally the case. However, for backgrounds formed from random track combinations these vectors are not necessarily aligned. Therefore the disagreement between the data and Monte Carlo can depend on the random combinatorical background, which in turn will depend on the resolution in distance of closest approach. The disagreement in the amount separated by the cut is 0.95% in the 29 GeV data and 1.20% in the 91 GeV data.

5.5.5 First Mass Cut

The first mass cuts are so loose that they should not affect the efficiency much, except for the case of extremely mismeasured tracks. Backgrounds in the inner layers of the detector or hit inefficiencies very different from that in the data can cause track parameters to be so wrong that real K^0_S and Λ can fail these cuts. It is assumed that such differences show up in the other distributions.

5.5.6 χ^2 Cut

The error from the cut on the χ^2 fit of two tracks to a common vertex is best estimated by looking at all tracks without any of the K^0_S and Λ search cuts imposed previously, because most of these tracks do come from a common vertex. If the search cuts are previously imposed, then extra background tracks in either the data or the Monte Carlo are those that miss the vertex, and will bias the tail of the χ^2 distribution. Thus the distribution for all tracks gives a better idea of the χ^2 resolution of the detector. The error introduced by the χ^2 cut is 3.81% at 29 GeV and 4.89% at 91 GeV.

5.5.7 Second Mass Cuts

The error from the second mass cut will primarily depend on differences in the mass resolution between the data and the Monte Carlo. The mass resolution, as measured as the Gaussian width of the K^0_S peak given in Table 13, is generally better for the Monte Carlo than for the data. This causes the efficiency to be overestimated owing to the tails outside the defined signal region being smaller in

the Monte Carlo than in the data. The error due to this effect is calculated by fitting the mass peaks and using the fitted form to evaluate the size of the tails outside the mass region. Less than one percent of any of the Gaussian fits lie outside the cuts for any of the mass fits, because the size of the signal region is in all cases more than two an a half times the width of the Gaussian; however, there are non-Gaussian tails arising from the variation of resolution with momentum and poorly tracked decays which can increase inefficiency. To take into account such effects, the error calculated from the Gaussian widths is increased. It is assumed that the existence of these tails will be modelled by the Monte Carlo. There is some difficulty with the 91 GeV data; since the statistics are small, the error on the calculated width of the peak is fairly large. For those cases where the width of the fitted Gaussian is less than 1/3 the width of the defined signal region, an error of 1% is assigned. This calculation results in an error of 1% for both Λ signals and for the K^0 signal at 29 GeV. The error on the K^0 signal for 91 GeV is assigned to be 3%.

TABLE 13. The fitted width of the K^0 and Λ mass peaks is given for data and Monte Carlo at both 29 GeV and 91 GeV. The Monte Carlo gives a consistently better mass resolution.

Particle	29 GeV		91 GeV	
	Data	Monte Carlo	Data	Monte Carlo
K^0_s	5.5 GeV/c^2	4.4 GeV/c^2	7.7 GeV/c^2	6.0 GeV/c^2
Λ	2.2 GeV/c^2	1.8 GeV/c^2	2.9 GeV/c^2	2.6 GeV/c^2

5.5.8 Total Systematic Error

The total systematic error from all causes is calculated by summing in quadrature the various contributions, which gives a systematic error of 11.5% for the K^0 at 91 GeV and 10.9% for the Λ. The systematic errors calculated for the 29 GeV data give 10.9% for both the K^0 and Λ signals. Table 14 gives the breakdown of the contributions to the systematic errors.

TABLE 14. The breakdown of the contributions to the systematic errors is shown for the 29 GeV data and the 91 GeV data. Systematic errors for the K^0 and Λ are shown together; if they differ, the two values are given separated by a semi-colon.

Source	29 GeV	91 GeV
Momentum Spectrum	4%	4%
Radiative Corrections	0.3%	0.3%
Selection Criteria:		
$\cos\theta$	0.4%	0.7%
$p_\perp$	0.61%	0.05%
z_{fid}	2.8%	0.27%
N_{DAZM}	0.43%	0.34%
DCA	0.58%	0.11%
$p_\perp \cdot DCA$	1.32%	2.40%
Δz	2.37%	2.17%
$\cos\alpha_{r\cdot p}$	0.95%	1.20%
χ^2	3.81%	4.89%
Mass Cuts	1%,1%	3%,1%
Total Detector	6.58%	7.21%,6.63%
Total	10.88%	11.51%,10.93%

5.5.9 Miscellaneous Checks on Accuracy of Simulation

In order to check that the detector simulation in the Monte Carlo agrees with the data, particularly for efficiency on tracks coming from a decay vertex far out in the detector, Figure 40 shows the number of K^0_S found at a given radius for data and Monte Carlo at 29 GeV. The agreement is good between the two, indicating that the efficiency for finding tracks from remote vertices is well-modelled.

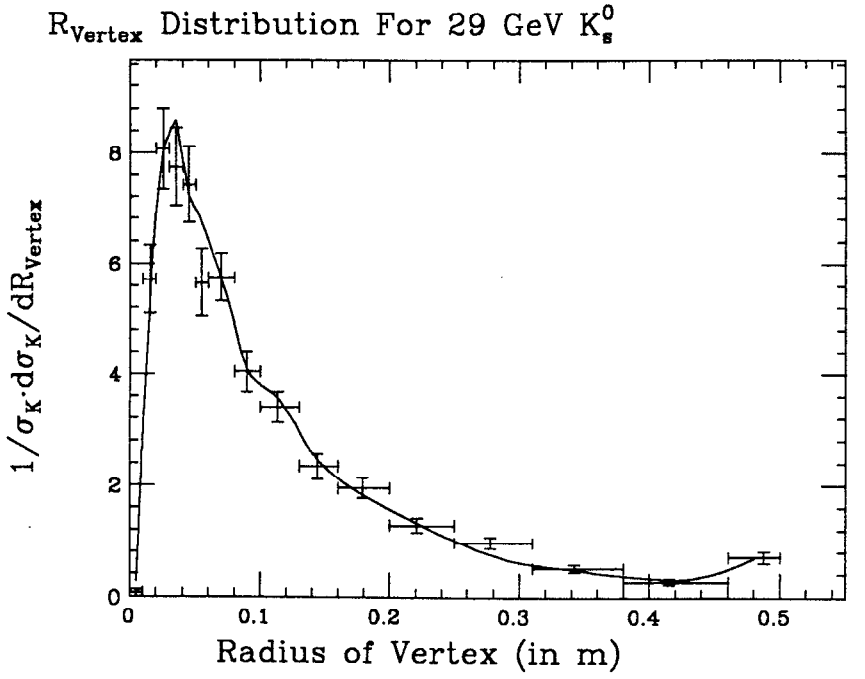

FIGURE 40. The distribution of the radius of K^0_S vertices in the 29 GeV data sample is compared with the Lund Monte Carlo. Agreement is good over the full range of the plot. The increase at the high end of the plot reflects the overflow bin of the histogram; good agreement there indicates that the data and Monte Carlo show similar distributions even beyond the range shown in the plot. The Monte Carlo is shown by the solid curve, the data by the points.

As another check on the quality of the K^0_S and Λ samples, $c\tau$ is plotted for the corrected data samples and the Monte Carlo produced samples. These are shown in the lifetime section in the next chapter. Again, agreement is good, indicating that the purity of the K^0_S and Λ samples is well-modelled, as is the dependence of efficiency on the radius at which the decay occurs.

A further check, to see whether the Monte Carlo properly models the dependence of efficiency on the opening angle of the decay, is to look at the distribution of the decay angle of the kaon in its center-of-mass frame. Since the kaon is a spin-0 particle, it should decay isotropically, and the distribution of decays should be flat in $|\cos\theta|$. Figure 41 shows the corrected distribution for the center-of-mass decay angle of the kaons, where the angle has been plotted for the positive track. As can be seen in the figure, the distribution is flat within errors, so the Monte Carlo modelling of the variation of efficiency with decay angle can be considered good. The efficiency is fairly constant except in the highest and lowest bins, where it falls, because the tracks fail to miss the vertex by a sufficient amount when they decay along the flight path of the kaon.

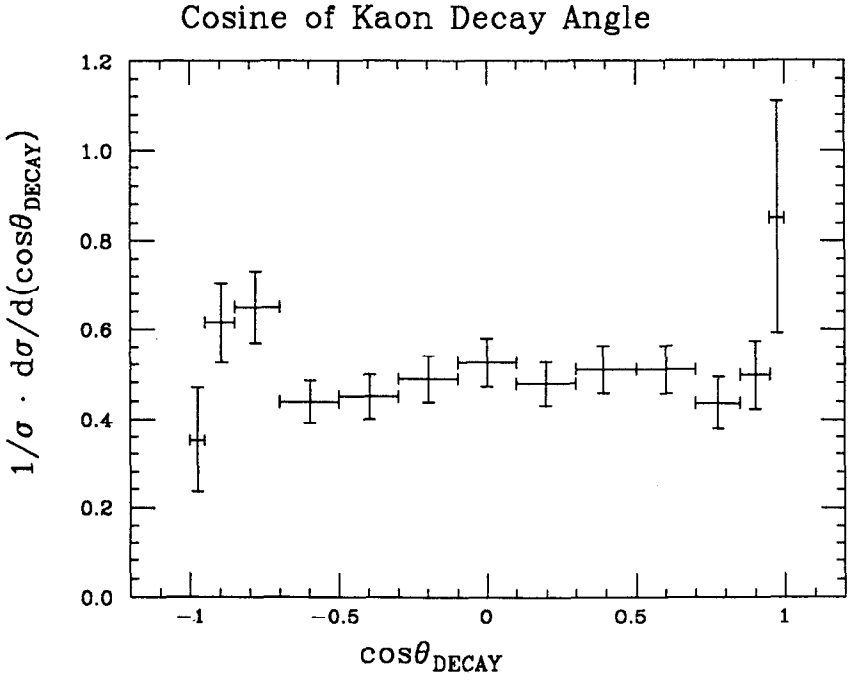

FIGURE 41. The distribution of the decay angle of the kaon in its center-of-mass frame is shown as a function of $\cos\theta_{decay}$. The distribution is flat within errors, as expected for a spin-0 particle. The decay angle is defined as the angle between the positive pion and the kaon flight path.

CHAPTER 6

RESULTS

Using the corrections and error estimates from the previous chapters, the final data sample can be translated into meaningful results. These results will be compared with the Monte Carlos, tuned in previous measurements to match the data at 29 GeV. They will also be compared with the results of other measurements on K^0 and Λ production in e^+e^- experiments.

If a hadronization model is to provide an accurate picture of the production of hadrons in e^+e^- collisions, it must not only agree with the rough numbers of hadrons produced in data, but must generate event shapes which accurately mimic the data. Within the hadronic event, the various kinds of hadrons must appear in the proper proportions and with correct kinematics. The models considered here have already been compared with general hadronic distributions in both the 29 GeV and the 91 GeV data taken with the Mark II detector as designed for the SLC, and found to compare well.[15][50]

Here the production of K^0 and Λ will be investigated within these hadronic events. The total numbers of K^0 and Λ will be calculated and compared with the models. The momentum and momentum flow of the produced K^0 and Λ will also be compared with the models. The dependence of K^0 and Λ production on event sphericity will also be checked for agreement with models, since production of strange particles may alter with increased gluon radiation and definitely increases with production of heavy quarks in the primary interaction, both of which increase event sphericity. First, however, as a check that the K^0 and Λ found in this analysis give a sample of the purity expected from Monte Carlo, the lifetime distributions of the K^0 and Λ will be compared to the expected lifetimes.

Unless stated otherwise, the distributions and values quoted for K^0 are for both K^0_S and K^0_L. Those for Λ include both the Λ and the $\bar{\Lambda}$.

6.1 K^0 and Λ Lifetimes

If the Monte Carlo gives the proper efficiencies and background contamination for the K^0 and Λ sample, the corrected distributions of $c\tau$ should show the expected exponential shape for both K^0_S and Λ, with the mean lifetime having a value of $c\tau = 2.67$ cm for the K^0_S and $c\tau = 7.89$ cm for the Λ.

In order to calculate the correction factors for this distribution, it is necessary to have a Monte Carlo which agrees with the momentum distributions of the particles. Monte Carlo which produces a harder momentum distribution for these particles will generally overestimate efficiencies for the short lifetime particles, because the decay distance is equal to $\beta\gamma c\tau$ and the short lifetime particles will travel further into the detector before decaying, and thus will be more likely to be detected (see Figure 38 for the dependence of detection efficiency on the radius of the vertex). Likewise, it will underestimate the efficiency for the long lifetime particles, because the higher momentum will make more of them decay outside of the effective detection volume of the drift chamber. As can be seen in Figure 43 later in the chapter, the momentum distributions of the Monte Carlos agree well with the data.

The correction factors used for the lifetime distributions are shown in Table 15. No correction for initial state radiation has been made here as the $c\tau$ distribution is independent of initial state radiation. Here the correction factors are made before background subtraction; they assume that the Monte Carlo has correctly modelled the background, and are calculated as the total number particles tagged as K^0_S or Λ per bin divided by the total number produced in that bin. The levels of background contamination in the data and the Monte Carlos agree within errors.

Figure 42a shows the distributions of $c\tau$ for the K^0_S in data and Monte

TABLE 15. Values and correction factors for the lifetime distributions are given. The center of gravity of the bin is given, together with the normalized value for that bin and the correction factor for that bin, for Λ and K^0 at 29 GeV and 91 GeV.

	29 GeV			91 GeV		
Particle	$c\tau$	$\frac{1}{\sigma}\frac{d\sigma}{d(c\tau)}$	$C(c\tau)$	$c\tau$	$\frac{1}{\sigma}\frac{d\sigma}{d(c\tau)}$	$C(c\tau)$
K^0_s	0.0025	32.7 ± 6.0	5.42 ± 0.02	0.0069	38.8 ± 9.4	1.57 ± 0.03
	0.0075	30.5 ± 2.9	1.25 ± 0.05	0.0156	19.9 ± 4.8	0.806 ± 0.06
	0.0125	26.5 ± 2.4	0.91 ± 0.06	0.0239	12.5 ± 3.8	0.83 ± 0.07
	0.0175	19.4 ± 2.0	0.88 ± 0.07	0.0340	11.3 ± 3.7	0.83 ± 0.08
	0.0249	13.4 ± 1.0	0.73 ± 0.06	0.0439	6.98 ± 2.70	0.73 ± 0.11
	0.0349	11.1 ± 1.0	0.77 ± 0.08	0.0596	4.88 ± 1.89	1.02 ± 0.08
	0.0455	6.34 ± 0.69	0.71 ± 0.09	0.0925	0.49 ± 0.49	1.06 ± 0.10
	0.0585	3.27 ± 0.35	0.74 ± 0.09	0.125	0.0	1.42 ± 0.14
	0.0795	2.13 ± 0.29	0.95 ± 0.10	0.178	0.0	2.99 ± 0.24
	0.1194	0.297 ± 0.078	1.08 ± 0.13	0.248	0.21 ± 0.27	0.70 ± 1.15
	0.1758	0.096 ± 0.080	2.69 ± 0.022			
	0.2385	0.11 ± 0.13	1.54 ± 0.69			
Λ	0.0172	12.2 ± 3.0	4.23 ± 0.04	0.0217	9.32 ± 2.79	1.32 ± 0.06
	0.0448	5.87 ± 0.91	0.87 ± 0.10	0.0875	3.78 ± 1.38	0.80 ± 0.10
	0.0787	3.94 ± 0.58	0.72 ± 0.12	0.129	2.87 ± 1.33	0.98 ± 0.12
	0.122	2.67 ± 0.44	0.76 ± 0.13	0.165	2.38 ± 1.25	1.01 ± 0.15
	0.179	2.21 ± 0.47	0.89 ± 0.16	0.275	1.01 ± 0.61	1.15 ± 0.15
	0.250	0.85 ± 0.20	0.95 ± 0.16	0.345	0.17 ± 0.17	0.56 ± 0.46
	0.342	0.44 ± 0.17	1.06 ± 0.24	0.495	0.07 ± 0.07	0.23 ± 1.10
	0.491	0.091 ± 0.03	0.15 ± 1.33			

Carlo at 29 GeV and 91 GeV. The data agrees well with the curve for the expected value of $c\tau = 2.675$ cm.[49] The average $c\tau$ found at 29 GeV 2.65 ± 0.37 cm; the average found at 91 GeV is 2.5 ± 1.1 cm. Figure 42b shows the distributions of $c\tau$ for the lambda in the data and Monte Carlo at both energies. Again, the data agrees with the expected distribution for $c\tau = 7.89$ cm. The average $c\tau$ found for the 29 GeV data is 9.6 ± 2.2 cm; for the 91 GeV data, it is 9.8 ± 5.4 cm. This indicates that the efficiencies calculated in Monte Carlo, as well as the backgrounds to the K^0 and Λ signals, are well-modelled in the Monte Carlo.

6.2 K^0 and Λ Multiplicities

The number of K^0 and Λ per hadronic event is expected to increase with $\sqrt{s}$ in the same manner as the overall charged multiplicity. With more energy available to the event, more partons can be produced and produce more hadrons in fragmentation.

6.2.1 Momentum Dependence of K^0 and Λ Production

The momentum distribution of the K^0 and Λ is important in the derivation of total numbers of K^0 and Λ because the efficiency is strongly momentum dependent, as shown in Chapter 5. If the data and Monte Carlo disagree on the momentum distribution, the use of a global efficiency with the numbers of K^0 and Λ found will give an incorrect result for the total numbers of those particles produced in the events. Therefore the agreement between the momentum distributions of the data and Monte Carlo must be checked. Figure 43a shows the momentum distributions for the K^0 at 29 GeV and 91 GeV, compared with the Lund and Webber Monte Carlos. The distributions agree well with the models. Figure 43b gives the same comparison for the Λ. Again, the data and Monte Carlo agree fairly well, although the 29 GeV data may show a slightly softer momentum spectrum than the Lund Monte Carlo. Table 16 lists the correction factors for the momentum distribution, together with the corrected value of the differential cross section in that bin.

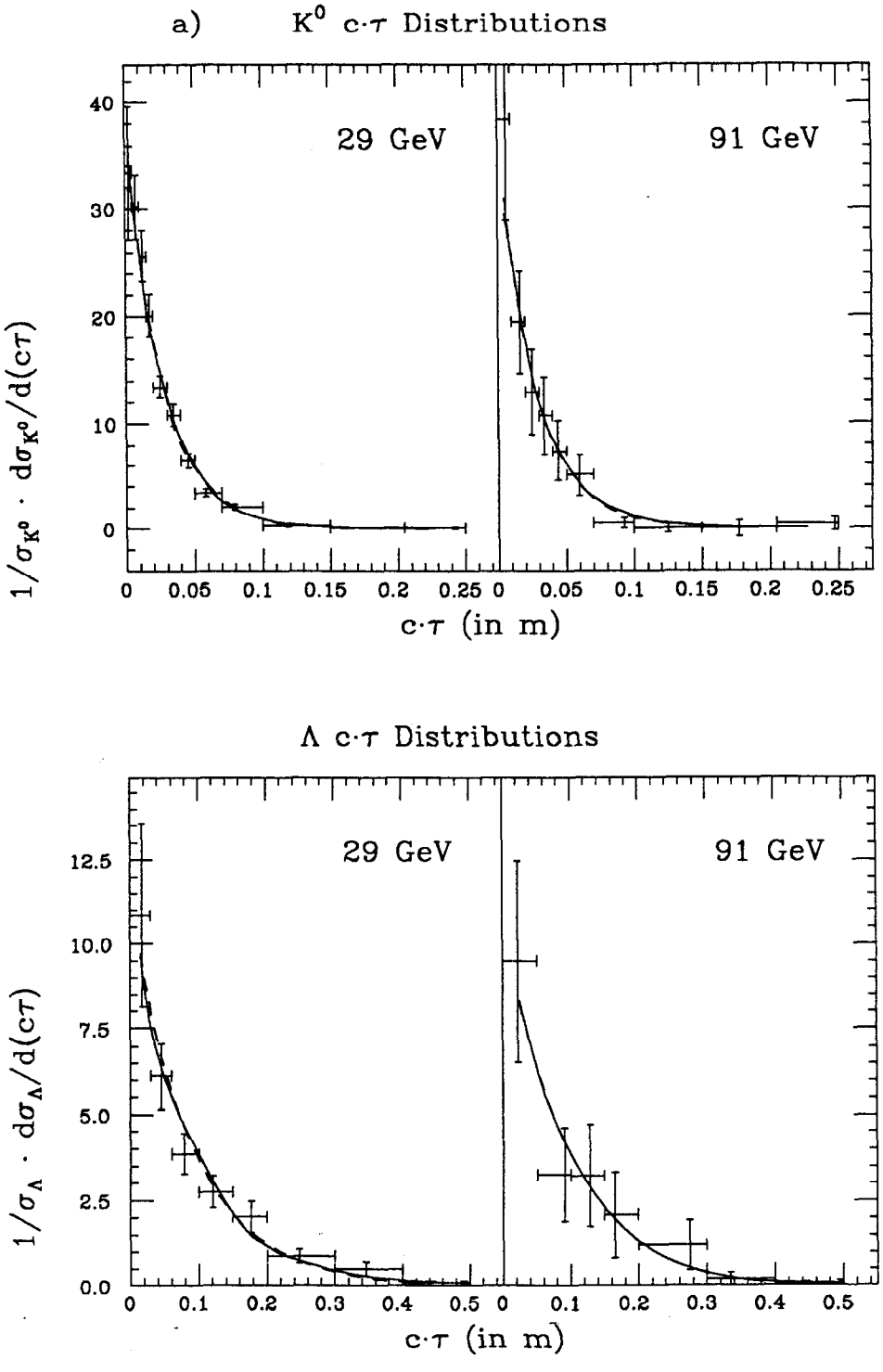

FIGURE 42. The lifetime distributions for K_S^0 and Λ are shown for both the 29 GeV and the 91 GeV data. The lines give the expected lifetime distribution from the Monte Carlo, which treats decay lifetime correctly.

TABLE 16. The values and correction factors for the momentum distributions are listed. The center of gravity of the bin is given, together with the normalized value of the differential cross section for that bin and the correction factor for that bin, for Λ and K^0 at 29 GeV and 91 GeV.

	29 GeV			91 GeV		
Particle	p	$\frac{1}{\sigma}\frac{d\sigma}{dp}$	$C(p)$	p	$\frac{1}{\sigma}\frac{d\sigma}{dp}$	$C(p)$
K_s^0	0.25	0.165 ± 0.029	2.45 ± 0.04	0.25	0.0	4.48 ± 0.04
	0.75	0.381 ± 0.034	1.60 ± 0.03	0.75	0.30 ± 0.13	1.67 ± 0.05
	1.25	0.361 ± 0.028	1.10 ± 0.05	1.41	0.26 ± 0.07	0.92 ± 0.05
	1.75	0.253 ± 0.021	0.86 ± 0.06	2.50	0.12 ± 0.05	0.68 ± 0.08
	2.25	0.201 ± 0.018	0.78 ± 0.07	3.79	0.058 ± 0.022	0.70 ± 0.07
	2.75	0.151 ± 0.015	0.67 ± 0.10	5.66	0.062 ± 0.021	0.75 ± 0.09
	3.45	0.105 ± 0.009	0.64 ± 0.08	9.00	0.008 ± 0.008	1.05 ± 0.08
	4.45	0.052 ± 0.006	0.73 ± 0.10	12.05	0.025 ± 0.014	1.74 ± 0.06
	5.85	0.031 ± 0.004	0.84 ± 0.10	17.58	0.015 ± 0.012	2.44 ± 0.08
	8.07	0.007 ± 0.002	0.91 ± 0.16	22.50	0.0	3.26 ± 0.09
	10.75	0.0005 ± 0.0005	0.95 ± 0.42			
Λ	0.25	1.70 ± 1.27	1.37 ± 0.17	0.25	0.0	1.57 ± 0.25
	0.75	0.37 ± 0.11	1.12 ± 0.11	0.75	0.21 ± 0.19	0.81 ± 0.18
	1.45	0.30 ± 0.05	1.06 ± 0.08	1.50	0.22 ± 0.10	0.85 ± 0.12
	2.40	0.17 ± 0.03	0.87 ± 0.10	2.54	0.11 ± 0.05	0.65 ± 0.16
	3.44	0.12 ± 0.02	0.81 ± 0.13	3.81	0.067 ± 0.028	0.69 ± 0.13
	4.49	0.10 ± 0.02	0.90 ± 0.15	7.25	0.007 ± 0.007	1.30 ± 0.08
	5.77	0.036 ± 0.011	1.09 ± 0.13	15.65	0.038 ± 0.020	2.76 ± 0.07
	7.94	0.016 ± 0.006	1.71 ± 0.14	22.75	0.0	-
	12.50	0.0	0.97 ± 0.49			

Since the agreement between the data and Monte Carlo is not perfect, the total numbers of K^0 and Λ are calculated by integrating the momentum distributions, and using the Monte Carlo to predict the numbers at low and high momentum, where the statistics are poor. These numbers are compared with those calculated using a global efficiency and background subtraction in the next section. The distributions are integrated over the range of momenta $0.5 < p < 10$ GeV/c. Even though K^0 and Λ are produced at higher momenta in the 91 GeV data, the statistics are so low that the appearance of any events in these higher momentum range bins can completely dominate the measurement when combined with the low expected efficiencies. The values obtained by this method are: $1.26 \pm 0.04 \pm 0.14$ K^0 and $0.170 \pm 0.015 \pm 0.018$ Λ per hadronic event at 29 GeV, and $1.54 \pm 0.21 \pm 0.18$ K^0 and $0.47 \pm 0.10 \pm 0.05$ Λ per hadronic event at 91 GeV. Integrating over a momentum range of 1 GeV/c to 10 GeV/c, thus dropping the lowest momentum bin which may be more subject to systematic errors, does not alter the values much: the multiplicities at 29 GeV become 1.31 for K^0 and 0.162 for Λ, while at 91 GeV they become 1.58 for K^0 and 0.432 for Λ. These changes are well within the statistical errors of the measurements. Addition of the bins from 10 GeV/c to 20 GeV/c does change the values by a large amount: the K^0 multiplicity at 91 GeV becomes 1.47 and the Λ multiplicity becomes 0.671. These changes are still within statistical errors. The large change in the Λ multiplicity is entirely due to three events at high momentum, which is not a statistically significant sample.

Values for the integration over $0.5 < p < 10$ GeV/c will be the ones quoted as the results in this paper; this is chosen because leaving out the 0.5-1.0 GeV/c range causes the systematic errors due to the method chosen for extrapolation to low momenta to become quite high, up to 20%.

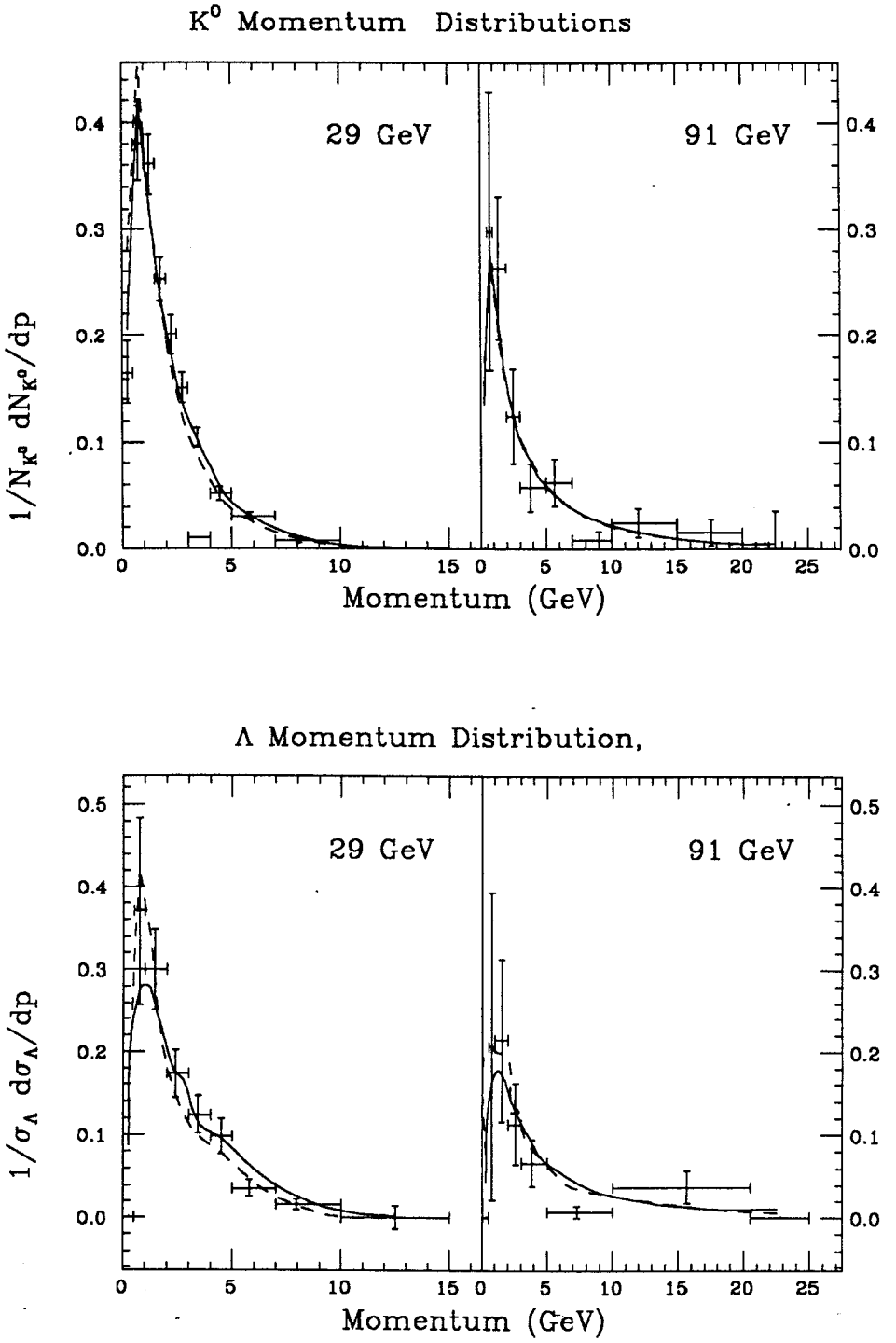

FIGURE 43. The momentum distributions for the corrected K^0 sample are shown in **a** for both 29 GeV and 91 GeV data; **b** shows the momentum distributions for the Λ. The solid line gives the Lund prediction; the dashed line gives the Webber prediction.

6.2.2 Total Production of K^0 and Λ

The total number of K^0 and Λ per hadronic event can also be calculated using the total numbers found together with background subtraction in the manner described in the previous chapter and a global efficiency. The use of a global efficiency assumes that the momentum distributions are well modelled by Monte Carlo, which the figures show to be a reasonable assumption, especially in the case of the K^0 distributions. Here the low and high momentum regions are automatically included in the efficiency.

This method gives a total number of K^0 per hadronic event of $1.28 \pm 0.04 \pm 0.10$ in the 29 GeV data and $1.35 \pm 0.19 \pm 0.10$ in the 91 GeV data. The number of Λ per hadronic event is found in this analysis to be $0.168 \pm 0.012 \pm 0.015$ at 29 2eV and $0.548 \pm 0.109 \pm 0.040$ at 91 GeV. These numbers agree within errors with those achieved by the method of integrating the momentum spectrum and using Monte Carlo to predict amounts in bins with very low efficiency. However, the previous results will be the results quoted as the integration over momentum bins is more Monte Carlo independent.

6.2.3 Comparison with Previous Analyses and Model Predictions

Table 17 shows the results of other experiments on the number of K^0 and Λ per hadronic event. The value obtained here for the number of K^0 at 29 GeV is slightly lower than the previous value obtained by the Mark II detector with different tracking chambers, but is within errors of all previous measurements. The value for the number of K^0 per hadronic event at 91 GeV, however, does not reflect the expected trend towards higher K^0 multiplicity with higher energy; it is about the same as the values measured in the region of 40 GeV by TASSO.

Figure 44 shows the number of K^0 per hadronic event *versus* $\sqrt{s}$, the center of mass energy of the interaction, together with the curves predicted by hadronization models. The Lund and Webber Monte Carlos, as tuned at 29 GeV, predict that the number of K^0 per hadronic event should be 2.2 and

TABLE 17. Measurements of the number of K^0 per hadronic event at various center-of-mass energies. All experiments are e^+e^- collider experiments.

Particle	Experiment	$< \sqrt{s} >$	Reference	Mean Multiplicity
K^0	Jade	12.0	53	$1.14 \pm 0.27 \pm 0.11$
	Jade	14.0	53	$1.05 \pm 0.10 \pm 0.11$
	Tasso	14.8	54	$1.17 \pm 0.09 \pm 0.07$
	Tasso	22	54	$1.28 \pm 0.11 \pm 0.08$
	Jade	22	53	$1.27 \pm 0.16 \pm 0.13$
	TPC	29	56	$1.22 \pm 0.03 \pm 0.15$
	Mark II	29	55	$1.27 \pm 0.03 \pm 0.15$
	Mark II	29	here	$1.26 \pm 0.04 \pm 0.14$
	HRS	29	57	$1.58 \pm 0.03 \pm 0.15$
	Jade	30	53	$1.49 \pm 0.22 \pm 0.15$
	Jade	34.5	53	$1.45 \pm 0.08 \pm 0.15$
	Tasso	34.5	54	$1.49 \pm 0.04 \pm 0.05$
	Tasso	35	54	$1.47 \pm 0.03 \pm 0.05$
	Cello	35	58	$1.42 \pm 0.09 \pm 0.18$
	Tasso	42.6	54	$1.52 \pm 0.05 \pm 0.05$
	Mark II	91	here	$1.54 \pm 0.21 \pm 0.18$
Λ	Mark II	29	here	$0.170 \pm 0.015 \pm 0.018$
	Mark II	29	59	$0.213 \pm 0.012 \pm 0.018$
	TPC	29	56	$0.197 \pm 0.012 \pm 0.017$
	HRS	29	57	$0.217 \pm 0.009 \pm 0.022$
	PEP 4/9	29	61	$0.211 \pm 0.009 \pm 0.014$
	Tasso	34.8	54	$0.218 \pm 0.011 \pm 0.021$
	Cello	35	58	$0.211 \pm 0.027 \pm 0.027$
	Jade	35	53	0.234 ± 0.064
	Tasso	42.1	54	$0.256 \pm 0.030 \pm 0.025$
	Mark II	91	here	$0.47 \pm 0.10 \pm 0.05$

2.5, respectively; the number found here is substantially lower, but falls within three sigma of the Lund prediction. The UCLA model predicts a lower value of K^0 production, 2.01 per hadronic event,[64] which agrees better with the value measured here but is still too high by over twice the statistical error. The Lund Monte Carlo predicts for the 29 GeV data a K^0 per hadronic event fraction of 1.39, which is well above the number measured here and most other measurements made at 29 GeV, although still within errors. The Webber Monte Carlo predicts 1.73 K^0 per hadronic event in the 29 GeV data, which is above the measurements but still within errors. The UCLA model predicts a value of 1.34 for the K^0 multiplicity, which is closer to the value measured here. Note, however, that use of a lower strange suppression factor in the Lund model will bring both the prediction at 29 GeV and the prediction at 91 GeV closer to the values measured here: a value of 0.27 for γ_s gives a 29 GeV prediction of 1.29 and a 91 GeV prediction of 2.0.

The ratio of K^0 multiplicity at 91 GeV and 29 GeV is found to be $1.22 \pm 0.17 \pm 0.20$. Here the full systematic error is kept; some of the systematics, however, should cancel since the same techniques and detector have been used at both energies. This ratio is within 2σ of the statistical error of the prediction of the UCLA model of 1.50 ± 0.02; it is also within 2σ of the prediction of the Lund model, 1.58. The prediction of the Webber model gives a ratio of about 1.5 also, so no discrimination between the models can be made on the basis of this measurement. It could, however, indicate that something is occurring in fragmentation which is not taken into account by the models, but given the large statistical errors on the measurement it should not be taken very seriously as an indication of problems with the models.

Table 17 gives the numbers of Λ per hadronic event found in previous analyses in e^+e^- experiments. The value of the number of Λ per hadronic event found here for the 29 GeV data is low compared to previous measurements at 29 GeV, but is consistent with them within errors. The Webber Monte Carlo as tuned by the Mark II at 29 GeV predicts fewer Λ per hadronic event than

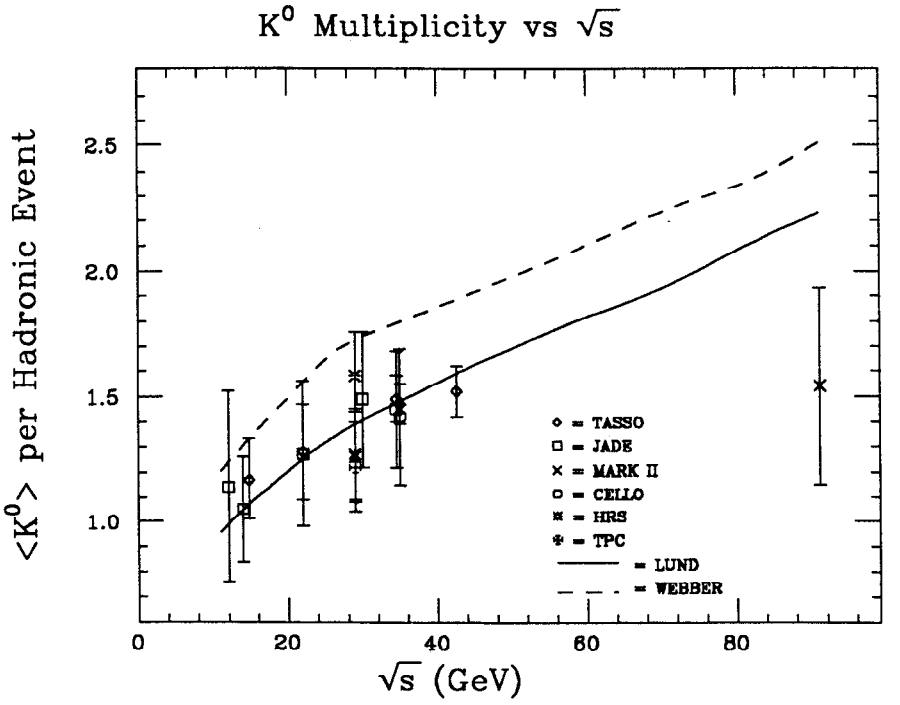

FIGURE 44. The K^0 multiplicity is shown as a function of $\sqrt{s}$. The predictions of the Lund and Webber Monte Carlos are also shown. The value found here at 91 GeV is substantially below the prediction of the model that K^0 multiplicity should rise with $\sqrt{s}$.

were found: 0.117 Λ per hadronic event, which is well below any measurement of the Λ fraction. The Lund Monte Carlo with the standard Mark II parameters predicts 0.229 Λ per hadronic event, which is higher than the value measured here but consistent with previous measurements and within errors of this measurement. The Lund Monte Carlo with $\gamma_s = 0.27$ gives a value of 0.207, which agrees better with this measurement. The UCLA model predicts a Λ multiplicity of 0.191 at 29 GeV, which is well within 2σ of the statistical error of this measurement.

The value of the Λ multiplicity for 91 GeV shows more than the expected increase from measurements at lower center-of-mass energy, although owing to low statistics it is within three sigma of the statistical error to all previous measurements. Figure 45 shows the values of the number of Λ per hadronic event *versus* $\sqrt{s}$. The value found at 91 GeV for the number of Λ per hadronic event is well above that predicted by the Webber Monte Carlo as tuned at 29 GeV, which

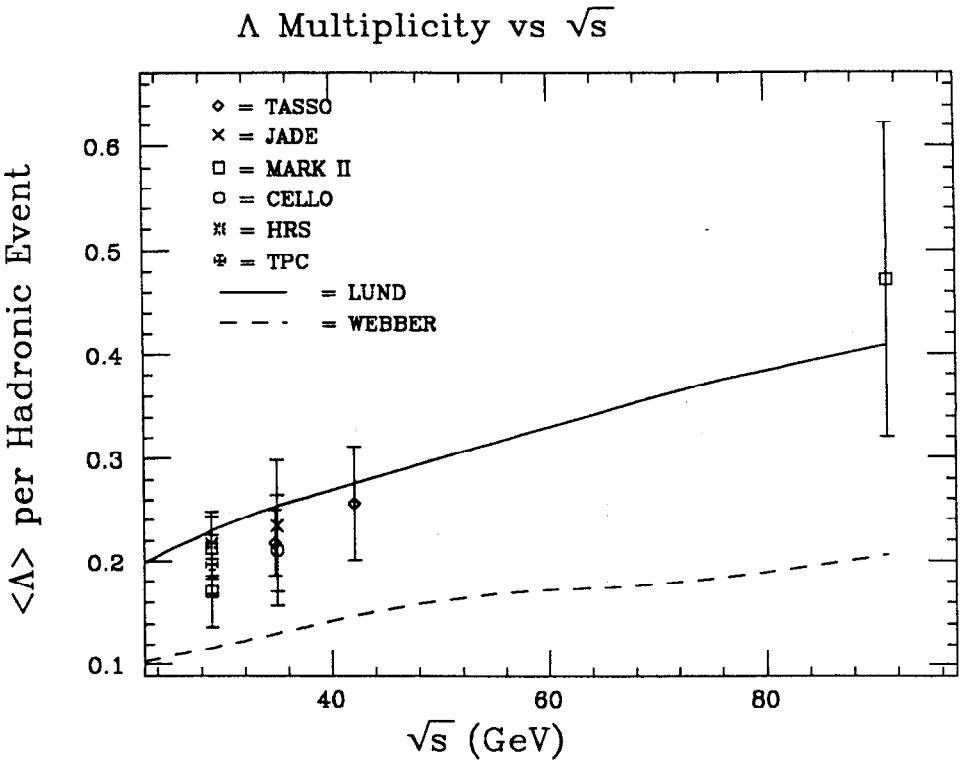

FIGURE 45. Measurements of the Λ multiplicity in hadronic events made at various e^+e^- colliders are plotted versus $\sqrt{s}$. The predictions of the Lund model and the Webber model as tuned at 29 GeV by the Mark II are also plotted.

expects .206 Λ per hadronic event; however, it is within several σ of the errors of the value. The agreement is better with the prediction of the Lund Monte Carlo of 0.408 Λ per hadronic event. The UCLA model predicts a Λ multiplicity at 91 GeV of 0.368, which is one sigma of the statistical error away from the value measured here. The parameters of the Webber model as tuned on general hadronic distributions at TASSO predict a value of Λ multiplicity of less than 0.01, which is far too low.

The ratios of Λ multiplicities at 91 GeV to those at 29 GeV predicted by the models are: 1.76 for the Webber model, 1.77 for the Lund model, and 1.97 for the UCLA model. The value found here is $2.77 \pm 0.64 \pm 0.42$. Again, the full systematic error is quoted although some of the systematics should cancel out owing to the nearly identical measurement methods used at the two energies. The value found here is well above any of the model predictions, although the UCLA

model comes closest, and all are within 2σ of the statistical error.

Note that the number of lambda found and the number of antilambda found were equal within errors.

6.3 Sources of K^0 and Λ

This measurement of K^0 and Λ production is intended to study the appearance of strange mesons and baryons in fragmentation. However, there are many sources of K^0 and Λ production in hadronic events: a primary $s\bar{s}$ pair can combine with quarks from the vacuum to produce K^0 and Λ; K^0 and Λ will also appear in the decay products of primary b and c quarks. In addition, heavier strange or even possibly charmed particles in fragmentation can decay into K^0 and Λ. Unfortunately, it is not possible to tell which K^0 and Λ are from primary production, and certainly difficult to tell which are the result of decays. Therefore, all K^0 and Λ will be treated together in the discussions of production kinematics which follow.

Figure 46 shows the various contributions to K^0 and Λ production as a function of energy. Direct production through fragmentation only contributes about a third of all K^0 and Λ; the majority of them come from decay of heavier fragmentation products, or the decay of primary c and b. The production of K^0 and Λ from primary strange quarks is not a very large contribution, although it increases near 91 GeV because of the larger coupling of the Z^0 to strange quarks. The production from decay of charm and bottom quarks stays fairly steady as energy changes. The production of Λ is expected to increase faster than the production of K^0, as could be seen by the ratios discussed in the previous section. This is mostly due to a faster increase in production from decay of heavier fragmentation particles.

Note that the production of K^0 from primary strange quarks is expected to increase by about 0.16 from 29 GeV to 91 GeV. If this is indeed the case, then the K^0 multiplicities measured here would indicate that production through

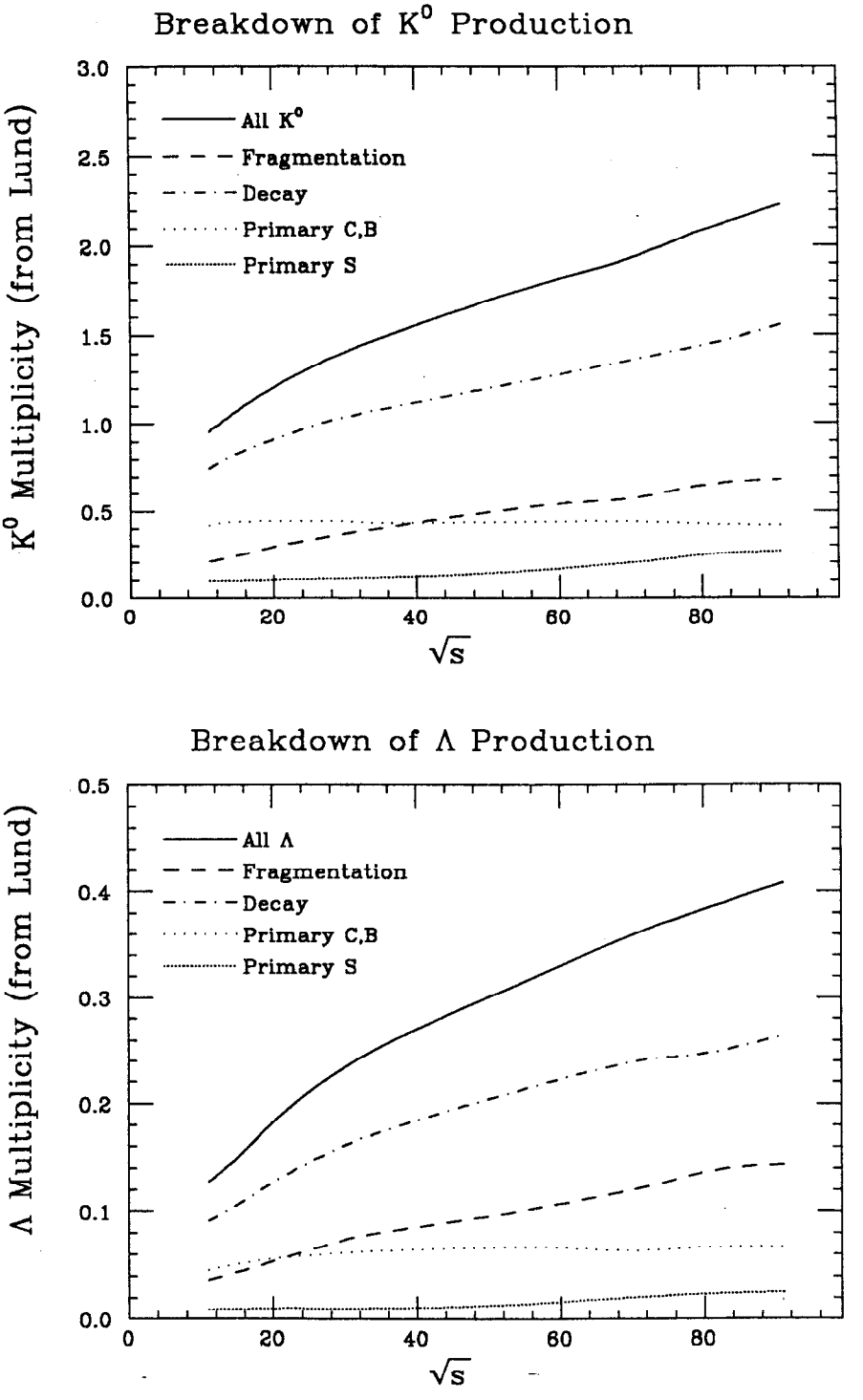

FIGURE 46. The production of K^0 and Λ is broken down into four categories: all fragmentation production (including primary $s\bar{s}$), primary $s\bar{s}$ alone, all decay of heavier particles, and decay of primary charm and bottom quarks alone. Predictions are made from the Lund monte carlo as tuned by the Mark II.

fragmentation has increased by only 0.12. However, this should not be taken too seriously given the large statistical errors on the measurement.

6.4 Scaled Momentum Distributions

Closely related to the momentum distribution is the scaled momentum distribution, which shows the dependence of production on the variable $x = 2 \cdot \frac{p}{E_{cm}}$. Since the maximum possible energy a particle can have is $E_{cm}/2$, x must lie between 0.0 and 1.0, and shows the fraction of the initial quark momentum with which a given particle is produced. Fragmentation into many hadrons of the initial state quarks means that none will have $x = 1.0$, and the majority of particles will appear at small x. If only one hadron were produced for each initial state quark, both should have $x = 1.0$.

The acquisition of a given fraction of initial state momentum by a particle would have the same probability at all center-of-mass energies if gluon radiation did not occur. This property, known as scaling, means that the distribution $\frac{1}{\sigma}\frac{d\sigma}{dx}$ would be the same for all $\sqrt{s}$. However, gluon radiation increases the number of partons in fragmentation and thus decreases the momentum available to particles formed in fragmentation. With higher energy, the number of gluons radiated increases and amount of energy available has to be shared between more partons. Therefore particles formed in fragmentation of these partons have a smaller fraction of the initial quark momentum.

6.4.1 Results

The correction factors for the distribution of $\frac{1}{\sigma}\frac{d\sigma}{dx}$ are calculated on a bin-by-bin basis, as described in the previous chapter. The correction factors for the distributions for both K^0 and Λ are shown in Table 18. They vary greatly over the range in x as can be seen from the momentum dependence of the efficiencies shown in the last chapter.

The corrected distributions in x are shown in Table 18 and in Figure 47a for the K^0 and in Figure 47b for the Λ. Both figures also show the Monte Carlo

TABLE 18. The values and correction factors for the x distributions are listed. The center of gravity of the bin is given, together with the normalized value for that bin and the correction factor for that bin, for Λ and K^0 at 29 GeV and 91 GeV.

	29 GeV			91 GeV		
Particle	x	$\frac{1}{\sigma}\frac{d\sigma}{d(x)}$	$C(x)$	x Bin	$\frac{1}{\sigma}\frac{d\sigma}{d(x)}$	$C(x)$
K_s^0	0.0263	2.07 ± 0.31	2.10 ± 0.04	0.026	10.5 ± 2.2	$1.33pm0.03$
	0.0500	4.81 ± 0.59	1.50 ± 0.05	0.060	5.5 ± 1.2	0.69 ± 0.06
	0.0700	5.33 ± 0.59	1.27 ± 0.05	0.103	3.0 ± 0.9	0.72 ± 0.08
	0.0900	4.62 ± 0.48	0.96 ± 0.07	0.140	0.90 ± 0.37	0.87 ± 0.07
	0.1100	4.52 ± 0.47	0.87 ± 0.08	0.242	1.02 ± 0.47	1.49 ± 0.07
	0.1410	3.09 ± 0.27	0.87 ± 0.06	0.343	1.00 ± 0.61	2.43 ± 0.08
	0.1800	2.32 ± 0.21	0.70 ± 0.08	0.430	0.38 ± 0.38	2.78 ± 0.10
	0.2205	1.75 ± 0.18	0.65 ± 0.10	0.550	0.0	4.11 ± 0.14
	0.2694	1.14 ± 0.12	0.74 ± 0.09	0.700	0.0	4.36 ± 0.16
	0.3460	0.66 ± 0.08	0.85 ± 0.09			
	0.4391	0.41 ± 0.07	1.10 ± 0.10			
	0.5348	0.18 ± 0.05	1.29 ± 0.14			
	0.6700	0.06 ± 0.02	1.76 ± 0.13			
Λ	0.028	0.85 ± 0.31	1.06 ± 0.18	0.020	5.10 ± 1.86	0.87 ± 0.10
	0.060	4.64 ± 0.83	1.11 ± 0.10	0.057	6.94 ± 1.93	0.67 ± 0.12
	0.097	4.55 ± 0.77	0.98 ± 0.11	0.097	2.51 ± 1.05	0.85 ± 0.11
	0.143	3.86 ± 0.74	1.03 ± 0.12	0.230	0.66 ± 0.48	1.58 ± 0.08
	0.178	2.14 ± 0.44	0.78 ± 0.15	0.355	2.54 ± 1.45	3.46 ± 0.65
	0.219	1.74 ± 0.39	0.78 ± 0.16	0.520	0.0	10.90
	0.272	1.37 ± 0.29	0.78 ± 0.16	0.700	0.0	-
	0.337	1.10 ± 0.25	1.11 ± 0.12			
	0.447	0.50 ± 0.17	1.31 ± 0.14			
	0.533	0.38 ± 0.19	1.96 ± 0.15			
	0.650	0.04 ± 0.04	2.46 ± 0.14			

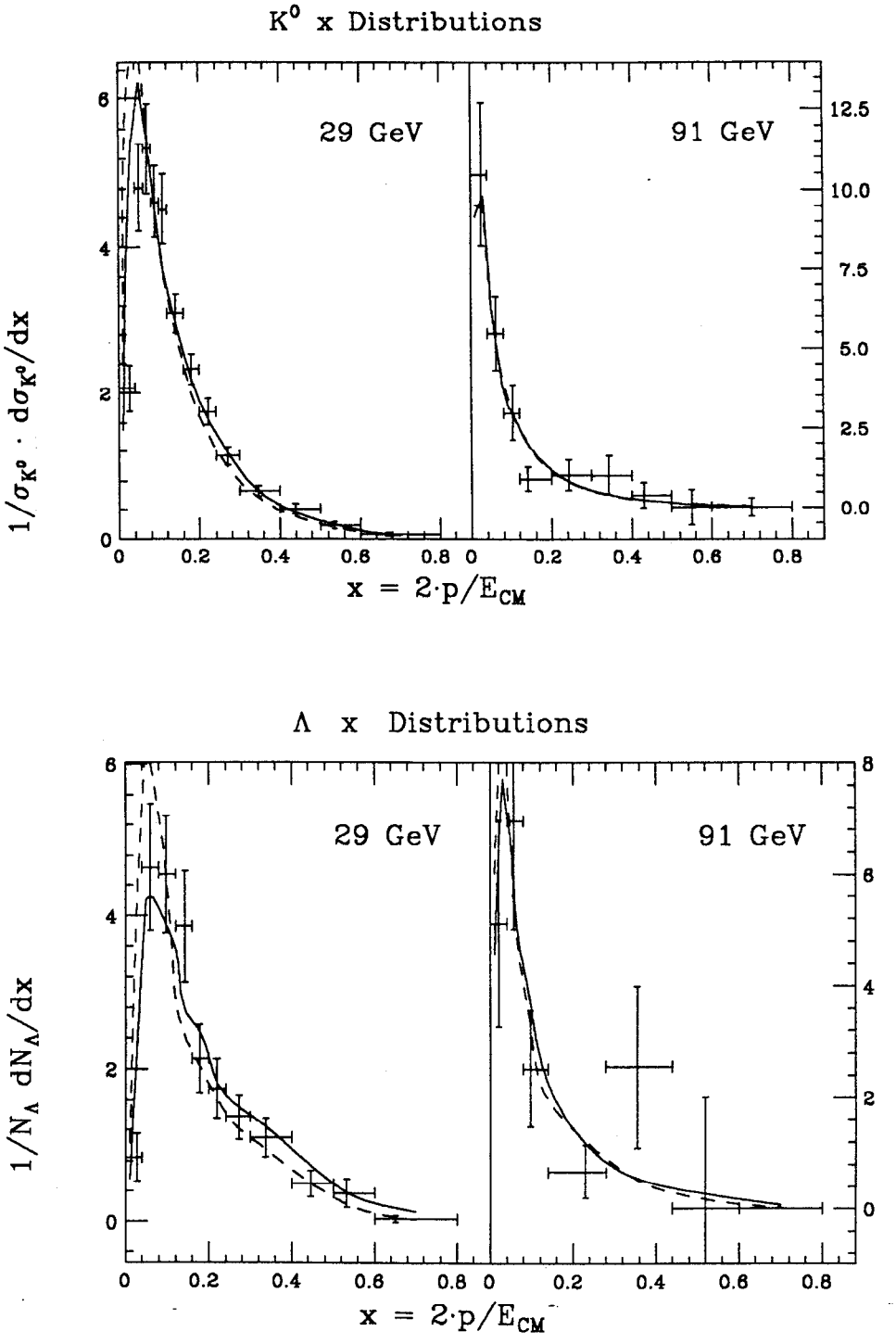

FIGURE 47. The variation of normalized cross section with scaled momentum are shown for both K^0 and Λ at 91 GeV and 29 GeV. The solid and dashed lines give the Lund and Webber Monte Carlo predictions, respectively.

models' predictions for the x distributions at both energies. Both models agree well with the data, although for the 29 GeV Λ the scaled momentum spectrum may again be softer than that predicted by the Lund model, although harder than that predicted by the Webber model. Scaling violations can be seen in the low and high x bins for the K^0, although the errors are large; in the Λ distributions the statistics are too low to show any such effect. Such scaling violations are expected in the Monte Carlo models, as can be seen from the figures.

6.5 Rapidity

In hadronization models, it is not only important to achieve the correct momentum distributions, but to have the flow of the momenta of produced particles, compared to the general flow of the energy of the event, be correct. In order to look at the behavior of the produced K^0 and Λ with respect to the general momentum flow of the event, it is first necessary to define the general momentum flow. In this analysis, the direction of general momentum flow is defined to be the thrust axis of the event. The thrust axis is defined as the unit vector $\hat{n}_1$ which maximizes the value of the thrust:

$$T = \frac{\sum_i |p_{i\|}|}{\sum_i |p_i|}$$

where i is an index running over all particles in the event and $p_{i\|}$ is the component of momentum parallel to $\hat{n}_1$. The secondary thrust axis is defined as the unit vector which maximizes the sum of momenta in a direction perpendicular to $\hat{n}_1$ and the third of the thrust axes is the unit vector orthogonal to the first two.

The rapidity y measures the distribution of a particle's momentum along the direction of the thrust of an event. It is defined as

$$y = |\frac{1}{2} \ln \frac{E + p_\|}{E - p_\|}|$$

where E is the energy of the event and $p_\|$ is the component of the particle's

momentum parallel to the thrust axis of the event. The mass of the tagged particle is used in calculating the energy.

6.5.1 Results

Again, correction factors for this distribution are calculated on a bin-by-bin basis. These correction factors are shown in Table 19 for K^0 and Λ at both energies.

The corrected rapidity distributions are shown in Figure 48a for the K^0 and in Figure 48b for the Λ. These figures also show the expected distributions from Monte Carlo. Note that the hadronization models predict a dip at low values of rapidity, followed by a plateau which falls off steeply to 0 at high values of rapidity. The dip at low rapidity is expected because few particles a produced with momentum near zero, and most particles should have momentum along the thrust axis of the event. The discrepancy on the prediction of this dip visible in the Webber model at 29 GeV is due to the fact that the Webber model predicts a smaller production of Λ from fragmentation, so that more of the Λ produced are from decay of heavier particles. The width of the plateau is expected to increase at higher energy due to the increase in parton energy. The data are consistent with the Monte Carlo models; however, the statistics are too low to determine well whether the rapidity distribution is indeed broader at 91 GeV than 29 GeV. Also, for the Λ at 29 GeV, the rapidity is peaked lower than the Lund Model predicts; this may not be a statistically significant effect, but it corresponds to the difference in momentum spectra discussed earlier.

6.6 $p_\perp$ Distributions

The amount of a particle's momentum which is transverse to the general energy flow of a hadronic event is also a physically significant quantity. Particles gain some of their transverse momentum from gluon radiation, which causes fragmentation to take place along directions other than the original quark direction; hard gluon radiation, producing additional jets, very much alters the transverse

TABLE 19. The values and correction factors for the rapidity distributions are given. The center of gravity of the bin is given, together with the corrected, normalized value for that bin and the correction factor for that bin, for Λ and K^0 at 29 GeV and 91 GeV.

	29 GeV			91 GeV		
Particle	Rapidity	$\frac{1}{\sigma}\frac{d\sigma}{dy}$	$C(y)$	Rapidity	$\frac{1}{\sigma}\frac{d\sigma}{dy}$	$C(y)$
K_s^0	0.206	0.38 ± 0.05	2.01 ± 0.04	0.200	0.22 ± 0.11	1.61 ± 0.05
	0.612	0.31 ± 0.03	1.42 ± 0.04	0.767	0.26 ± 0.09	1.24 ± 0.05
	1.014	0.38 ± 0.03	1.17 ± 0.04	1.278	0.37 ± 0.09	0.89 ± 0.06
	1.388	0.44 ± 0.03	0.98 ± 0.05	1.930	0.35 ± 0.08	0.76 ± 0.06
	1.798	0.41 ± 0.03	0.82 ± 0.06	2.563	0.23 ± 0.06	0.84 ± 0.06
	2.196	0.32 ± 0.02	0.70 ± 0.07	3.367	0.14 ± 0.06	1.35 ± 0.06
	2.655	0.14 ± 0.01	0.74 ± 0.08	3.900	0.0	1.90 ± 0.11
	3.198	0.028 ± 0.005	0.75 ± 0.18			
Λ	0.210	0.34 ± 0.08	1.46 ± 0.09	0.375	0.27 ± 0.10	0.92 ± 0.09
	0.602	0.53 ± 0.09	1.04 ± 0.10	1.331	0.36 ± 0.10	0.76 ± 0.10
	0.994	0.50 ± 0.08	0.89 ± 0.10	1.967	0.26 ± 0.09	0.98 ± 0.08
	1.437	0.40 ± 0.07	0.91 ± 0.10	3.150	0.24 ± 0.13	2.83 ± 0.06
	1.784	0.38 ± 0.06	0.86 ± 0.11			
	2.164	0.22 ± 0.05	1.07 ± 0.12			
	2.540	0.16 ± 0.05	1.31 ± 0.17			
	2.900	0.002 ± 0.002	0.76 ± 0.58			

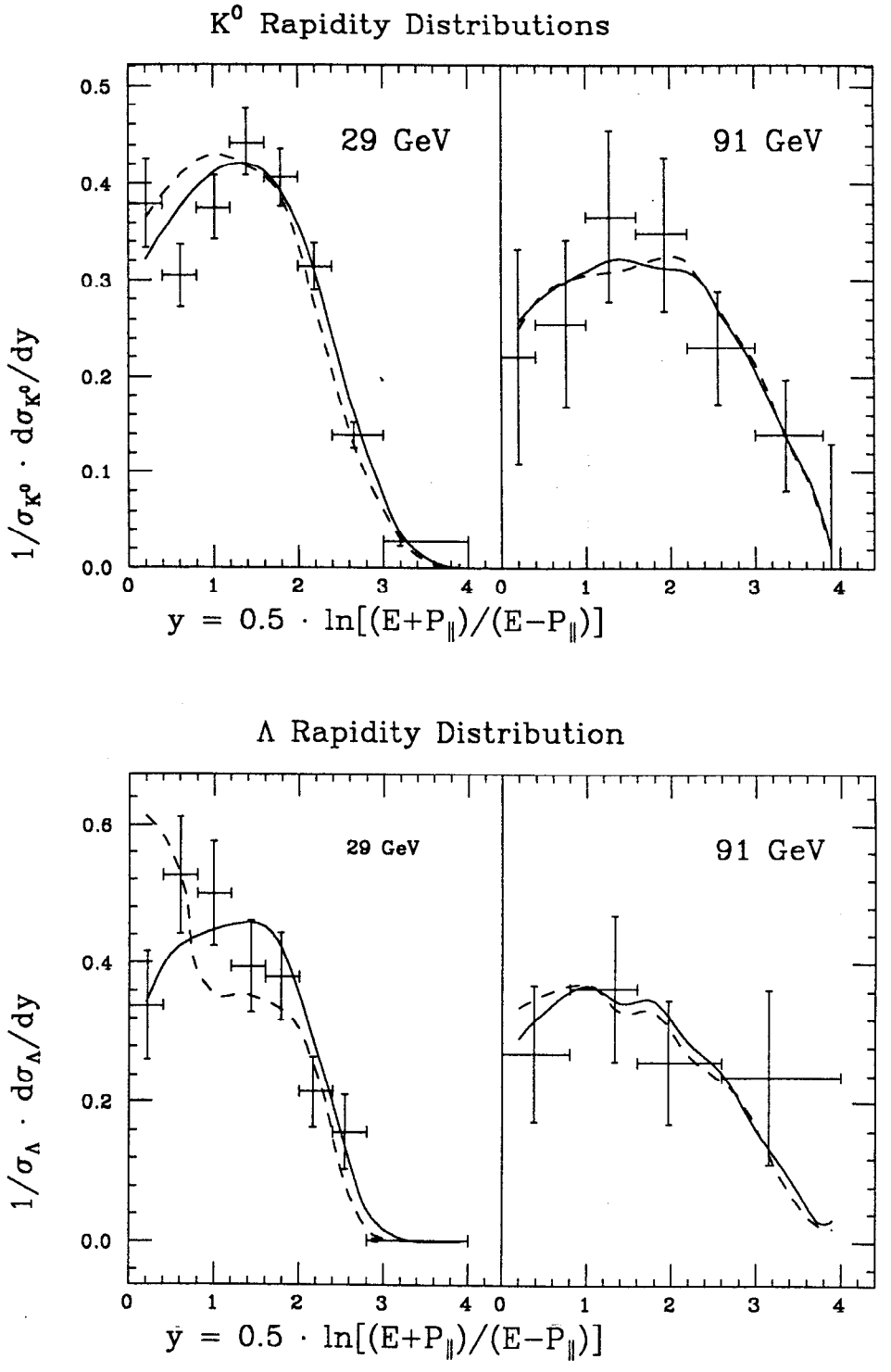

FIGURE 48. The rapidity distributions for K^0 are shown in **a** and those for Λ in **b**. The Lund Monte Carlo prediction is shown with the solid line, the Webber with a dashed line.

momentum distribution in an event.

According to the Lund Model, particles also gain transverse momentum in the process of tunneling from the vacuum; it produces particles with a Gaussian distribution of transverse momentum. In the Webber Model, the kinematics of cluster decay can give particles additional transverse momentum.

Two transverse momentum distributions are investigated here: the transverse momentum in ($p_{\perp in}$) and out ($p_{\perp out}$) of the event plane. The event plane here is defined by the thrust axis and the secondary thrust axis. In events with no hard gluon radiation little difference should show between the two directions, but in events with gluon radiation the direction of the third jet will largely determine the event plane. Due to the presence of gluon jets, therefore, the $p_{\perp in}$ distribution will be dominated by hard gluon radiation effects, but $p_{\perp out}$ will show the effects of the transverse momentum acquired by quarks in hadronization, which give a smaller transverse momentum distribution.

6.6.1 Results

Again, correction factors were calculated on a bin-by-bin basis. These correction factors are shown in Table 20 for the distributions of $1/\sigma\,(d\sigma/dp_{\perp in})$ and Table 21 for the distributions of $1/\sigma(d\sigma/dp_{\perp out})$. The corrected distributions are shown in Figure 49a for the kaon $p_{\perp in}$ and Figure 50a for the kaon $p_{\perp out}$. Figures 49b and 50b show the same distributions for the lambda.

The data agree with the predictions of the Monte Carlo models on the shapes of the distributions. The $p_{\perp in}$ distribution is wider than the $p_{\perp out}$ distribution, as is expected, and shows a long tail out to higher $p_{\perp}$ as would be expected for production of strange particles in fragmentation of gluon jets.

TABLE 20. The center of gravity of the bin is given, together with the normalized value for that bin and the correction factor for that bin, for Λ and K^0 at 29 GeV and 91 GeV.

	29 GeV			91 GeV		
Particle	$p_{\perp in}$ Bin	$\frac{1}{\sigma}d\sigma/d(p_{\perp in})$	$C(p_{\perp in})$	$p_{\perp in}$ Bin	$\frac{1}{\sigma}d\sigma/d(p_{\perp in})$	$C(p_{\perp in})$
K_s^0	0.050	1.34 ± 0.12	1.03 ± 0.05	0.106	1.20 ± 0.31	1.10 ± 0.04
	0.150	1.67 ± 0.14	1.15 ± 0.05	0.289	0.98 ± 0.28	1.10 ± 0.05
	0.250	1.55 ± 0.14	1.14 ± 0.05	0.550	0.72 ± 0.19	1.05 ± 0.05
	0.394	1.01 ± 0.07	0.98 ± 0.04	0.840	0.44 ± 0.14	0.96 ± 0.07
	0.599	0.61 ± 0.05	0.95 ± 0.06	1.138	0.18 ± 0.06	0.82 ± 0.08
	0.838	0.32 ± 0.03	0.88 ± 0.07	1.670	0.09 ± 0.04	0.67 ± 0.14
	1.190	0.15 ± 0.02	0.83 ± 0.09	2.275	0.10 ± 0.05	0.88 ± 0.16
	1.761	0.051 ± 0.010	0.89 ± 0.15	2.650	0.02 ± 0.02	0.75 ± 0.23
	2.446	0.014 ± 0.004	0.77 ± 0.23	3.850	0.01 ± 0.01	0.80 ± 0.21
	3.280	0.007 ± 0.004	1.06 ± 0.40	4.500	0.0	1.64 ± 0.15
	4.050	0.0004 ± 0.0004	0.63 ± 1.21			
Λ	0.099	1.53 ± 0.21	0.99 ± 0.09	0.133	0.95 ± 0.28	0.81 ± 0.10
	0.303	0.96 ± 0.14	0.83 ± 0.10	0.42	1.07 ± 0.35	1.09 ± 0.09
	0.536	0.77 ± 0.12	1.11 ± 0.08	0.79	0.40 ± 0.18	1.09 ± 0.10
	0.841	0.42 ± 0.09	1.24 ± 0.10	1.17	0.30 ± 0.14	1.02 ± 0.13
	1.163	0.19 ± 0.04	0.98 ± 0.14	1.85	0.046 ± 0.046	0.78 ± 0.21
	1.723	0.10 ± 0.04	1.07 ± 0.22	2.35	0.036 ± 0.36	1.22 ± 0.15
	2.250	0.0	0.97 ± 0.35	3.50	0.0	1.69 ± 0.19
	2.750	0.0	0.89 ± 0.54	4.50	0.0	2.38 ± 0.14
	3.550	0.002 ± 0.002	0.5 ± 0.8			

TABLE 21. The center of gravity of the bin is given, together with the normalized value for that bin and the correction factor for that bin, for Λ and K^0 at 29 GeV and 91 GeV.

	29 GeV			91 GeV		
Particle	$p_{\perp out}$ Bin	$\frac{1}{\sigma}d\sigma/d(p_{\perp out})$	$C(p_{\perp out})$	$p_{\perp out}$ Bin	$\frac{1}{\sigma}d\sigma/d(p_{\perp out})$	$C(p_{\perp out})$
K^0_s	0.050	2.79 ± 0.18	1.11 ± 0.04	0.050	2.07 ± 0.54	1.01 ± 0.05
	0.150	2.25 ± 0.16	1.09 ± 0.04	0.205	1.47 ± 0.32	0.98 ± 0.04
	0.250	1.43 ± 0.12	0.99 ± 0.05	0.383	1.09 ± 0.29	1.07 ± 0.05
	0.395	1.03 ± 0.07	0.94 ± 0.05	0.579	0.49 ± 0.19	1.02 ± 0.07
	0.581	0.45 ± 0.04	0.81 ± 0.08	0.780	0.47 ± 0.15	1.02 ± 0.09
	0.831	0.13 ± 0.02	0.78 ± 0.13	1.283	0.08 ± 0.05	0.94 ± 0.14
	1.225	0.03 ± 0.01	1.05 ± 0.23	1.550	0.02 ± 0.02	0.59 ± 0.35
	1.600	0.0014 ± 0.0009	0.26 ± 1.86	2.500	0.0	-
	2.500	0.0	-			
Λ	0.050	2.49 ± 0.33	0.86 ± 0.10	0.100	1.18 ± 0.38	0.80 ± 0.09
	0.150	2.06 ± 0.31	0.97 ± 0.09	0.35	1.61 ± 0.45	1.17 ± 0.07
	0.250	1.63 ± 0.28	0.98 ± 0.10	0.64	0.57 ± 0.20	1.08 ± 0.09
	0.392	1.16 ± 0.19	1.22 ± 0.08	1.25	0.03 ± 0.03	1.13 ± 0.16
	0.588	0.41 ± 0.10	1.08 ± 0.13	2.50	0.0	1.50 ± 0.40
	0.80	0.18 ± 0.06	0.95 ± 0.20			
	1.25	0.02 ± 0.01	1.36 ± 0.32			
	1.75	0.0	-			
	2.50	0.0	-			

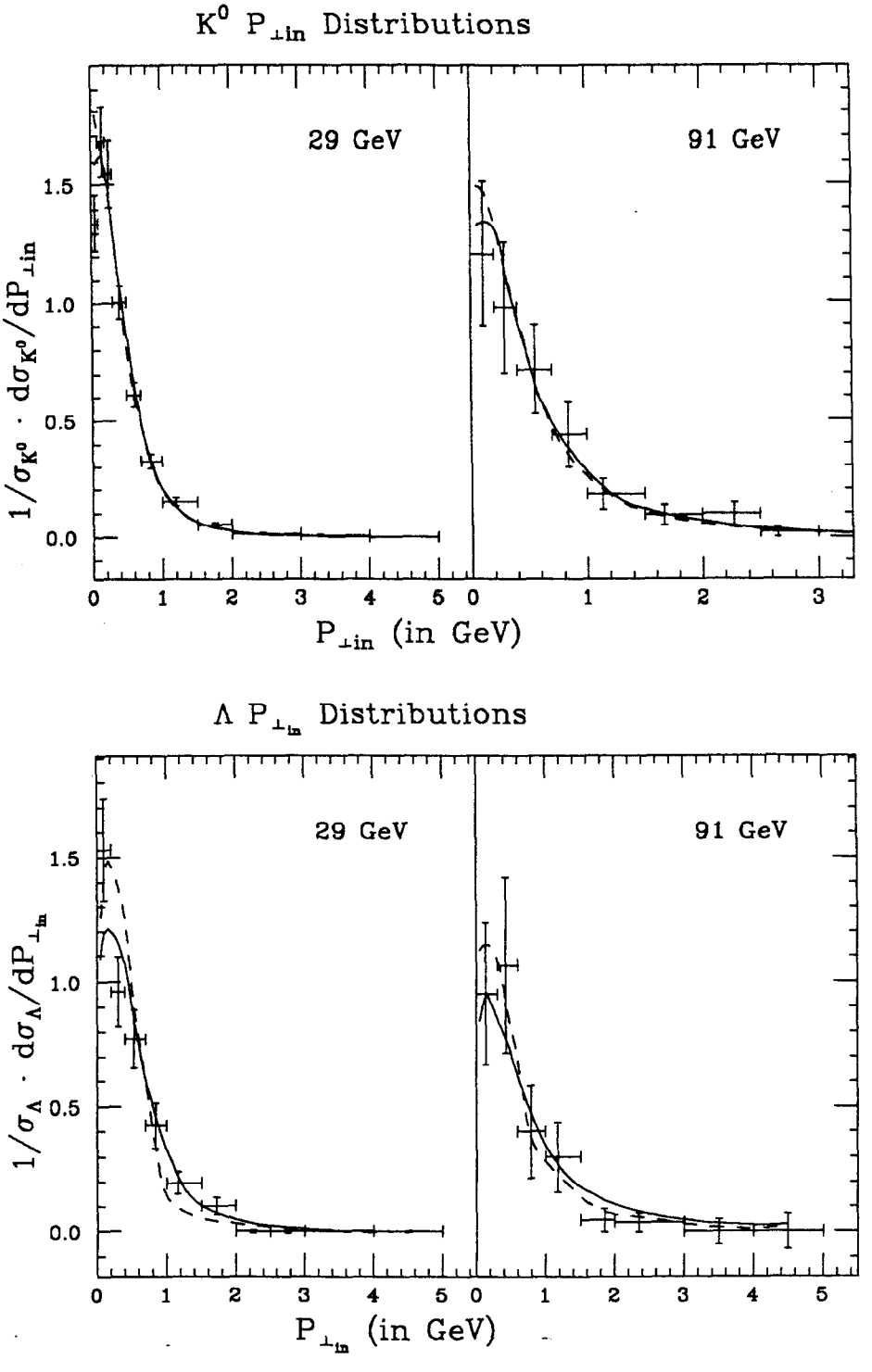

FIGURE 49. The distributions of $p_{\perp in}$ are shown for the K^0 in **a** and for the Λ in **b**. They show the long tail at high transverse momentum expected from gluon radiation by the Monte Carlos, shown by a solid line for Lund and a dashed line for the Webber model.

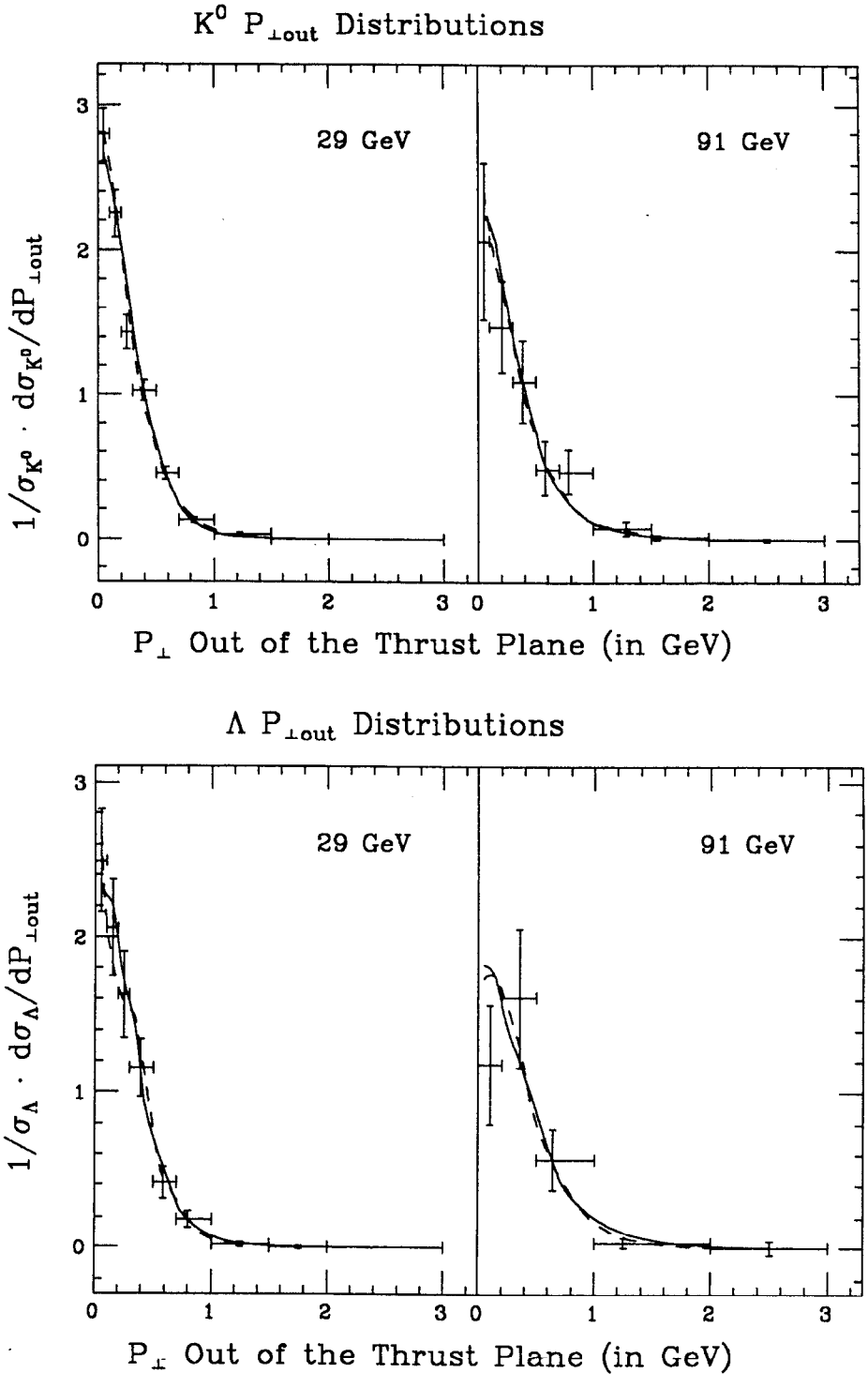

FIGURE 50. The distributions of $p_{\perp out}$ are shown for the K^0 in **a** and for the Λ in **b**. They show the long tail at high tranverse momentum expected from gluon radiation by the Monte Carlos, shown by a solid line for Lund and a dashed line for the Webber model.

6.7 Sphericity Dependence of Strange Particle Production

The dependence of strange particle production on event sphericity is also of interest. The sphericity of an event depends partly on the hard gluon emission in an event and partly on the nature of the primary quarks: heavy quarks such as bottom and charm have lower velocity so the jets they produce are less highly boosted and less collimated. Bottom and charm decay predominantly into strange quarks, so that events arising from bottom and charm production should show a slightly higher number of strange quarks than the average; however, this effect is partly offset by the production of primary strange quarks in low sphericity events. Also, since this analysis looks only at K^0 and Λ, the fraction of these particles generated by the decays of bottom and charm is much smaller than the number of strange quarks expected to be produced, so this effect is not expected to be visible with the present statistics. Gluon jets may even enhance the number of lambda produced, according to the string models, because of the double break at the kink in the string. This effect would primarily affect Λ produced at high momentum. Again, is an effect which would require large statistics to become visible. However, it is of interest to know whether gluon radiation affects fragmentation into strange particles, or whether strange particle production could be depleted in gluon jets.

As a consequence it is of interest to look at the dependence of strange particle production on the sphericity of events. Figure 51a shows the number of kaons per hadronic event versus the hadronic event sphericity. Figure 51b shows the same distribution for the lambda. Table 22 lists the correction factors used for each bin. Again, these correction factors were calculated on a bin-by-bin basis. They do not include radiative corrections.

The distributions show an expected rise from the value near zero sphericity, followed by flat distributions above a value of 0.2. This indicates that strange particles are being produced in the fragmentation of the gluon jets, since the high sphericity region shows no depletion in either K^0 or Λ. The data at

TABLE 22. The center of gravity of the bin is given, together with the normalized value for that bin and the correction factor for that bin, for Λ and K^0 at 29 GeV and 91 GeV.

	29 GeV			91 GeV		
Particle	Sphericity	$N_{K^0,\Lambda}/N_{had}$	$C(Spher)$	Sphericity	$N_{K^0,\Lambda}/N_{had}$	$C(Spher)$
K_s^0	0.0125	0.82 ± 0.10	5.80 ± 0.01	0.038	1.39 ± 0.21	7.99 ± 0.003
	0.0375	0.99 ± 0.08	6.33 ± 0.01	0.179	1.87 ± 0.43	7.68 ± 0.01
	0.0625	1.10 ± 0.09	6.29 ± 0.01	0.395	2.72 ± 1.05	7.38 ± 0.01
	0.0875	1.24 ± 0.12	6.09 ± 0.01			
	0.124	1.31 ± 0.11	6.47 ± 0.01			
	0.215	1.20 ± 0.09	6.98 ± 0.01			
	0.439	1.36 ± 0.12	7.60 ± 0.01			
Λ	0.0125	0.09 ± 0.02	2.73 ± 0.05	0.040	0.48 ± 0.11	5.78 ± 0.01
	0.0375	0.15 ± 0.03	4.92 ± 0.02	0.154	0.38 ± 0.16	5.25 ± 0.02
	0.0625	0.16 ± 0.03	4.71 ± 0.02	0.479	1.61 ± 0.70	5.10 ± 0.03
	0.0875	0.20 ± 0.04	4.55 ± 0.03			
	0.123	0.20 ± 0.04	5.59 ± 0.02			
	0.218	0.17 ± 0.03	4.90 ± 0.02			
	0.411	0.19 ± 0.03	4.28 ± 0.03			

91 GeV show a tendency to continue rising with sphericity, but the errors are too large in the high sphericity region to make any definitive conclusion.

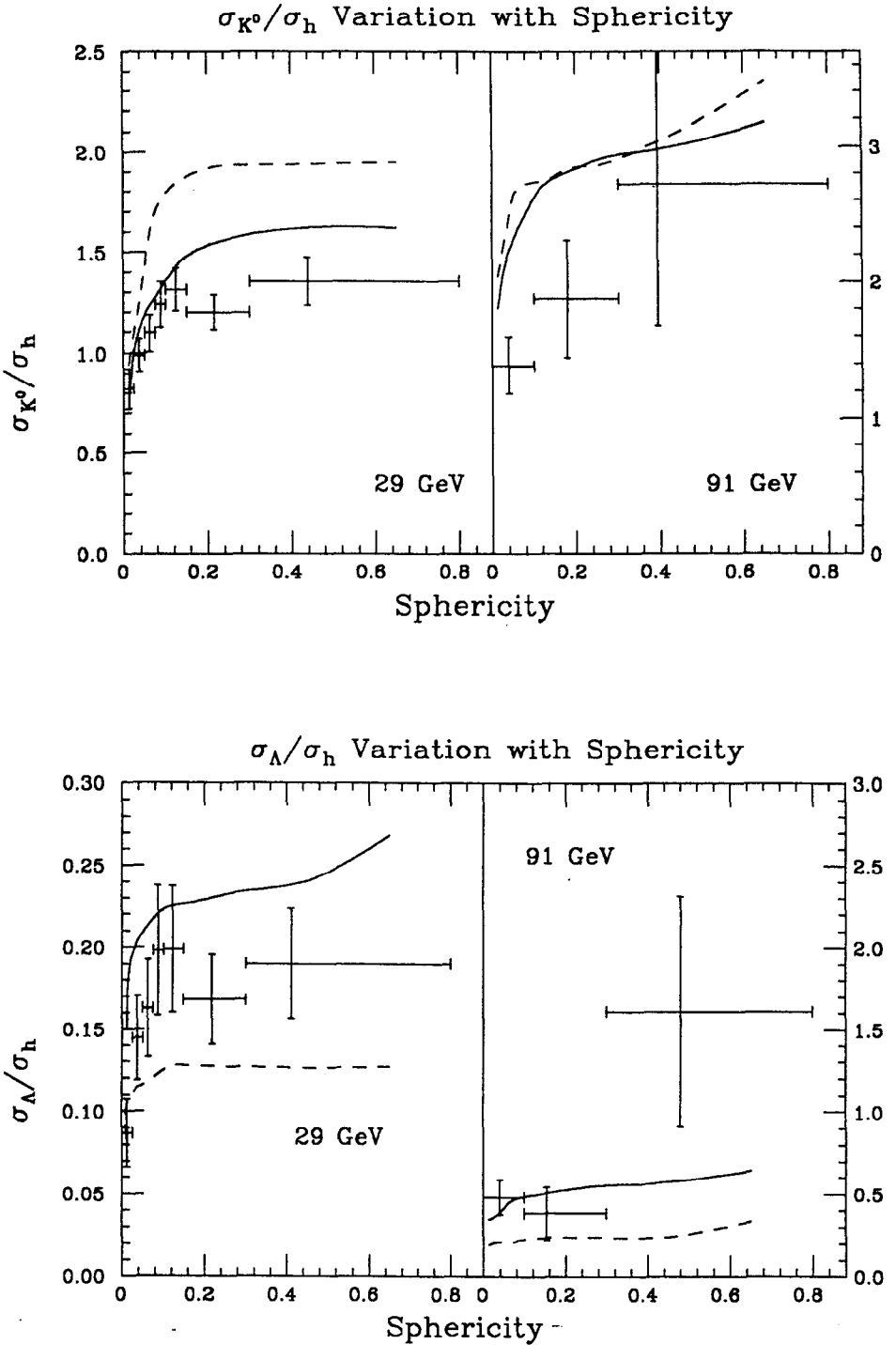

FIGURE 51. The number of K^0 and Λ per hadronic event is shown as a function of event sphericity at both 29 GeV and 91 GeV. The high peak at large sphericity in the 91 GeV Λ data comes from three events each of which held a found Λ.

CHAPTER 7

CONCLUSIONS

The last chapter presented measurements of aspects of K^0 and Λ production in hadronization. These measurements were made at two energies, 29 GeV and 91 GeV, using the same methods at both energies. The statistics at 91 GeV are unfortunately small, but still give indications of the behavior of strange particle production at the Z^0 resonance.

The multiplicities of K^0 and Λ in hadronic events have been measured at 29 GeV and 91 GeV. At 29 GeV, where other measurements have been published with higher but comparable statistics, the K^0 multiplicity has been measured at $1.26 \pm 0.04 \pm 0.14$. This is close to the values measured by other experiments, both at 29 GeV and at nearby energies. Measurements made at 22 GeV by TASSO and JADE are slightly higher, but have large statistical error; the measurements made at 29 GeV at PEP mostly lie lower than the curve extrapolated between measurements made at 22 GeV and 35 GeV by TASSO and JADE.

The measurement of K^0 multiplicity in 91 GeV hadronic events made here finds a value of $1.54 \pm 0.21 \pm 0.18$. This is much lower than the trend expected by all hadronization models; in fact, it is very close to values of the multiplicity measured in the region of 40 GeV by experiments at PETRA. The difference between the two multiplicities at 91 GeV and at 29 GeV is $0.28 \pm 0.21 \pm 0.23$ (Full systematic error is quoted; most of the systematic error should cancel since the same techniques and detector are used at both energies.) Since increased production from primary strange quarks is expected to account for 0.15 of the increase in multiplicity, this allows for very little increase in production from fragmentation. However, as the statistical errors are large this should not be taken as an indication of anomalies in fragmentation until measurements with higher statistics are available at 91 GeV.

The ratio of K^0 multiplicity at 91 GeV to that at 29 GeV is of interest because it can reveal more clearly than the separate numbers features of the models such as the energy dependence which appears in the UCLA model. Also, since the measurements made here of the K^0 multiplicities use the same techniques and essentially the same detector at both 29 GeV and 91 GeV, much of the systematic error should cancel. However, given that the machine environment was different and the absence of the vertex chamber, this is not entirely the case. The ratio found here is $1.22 \pm 0.17 \pm 0.20$ with all systematic errors included.

The values for Λ multiplicity measured here are $0.170 \pm 0.015 \pm 0.018$ at 29 GeV and $0.47 \pm 0.10 \pm 0.05$ at 91 GeV. The value at 29 GeV is low compared to other measurements and is slightly over 2.5σ of the statistical error lower than the world average of 0.208 ± 0.014. The change in multiplicity of Λ is $0.30 \pm 0.10 \pm 0.05$, again with full systematic errors quoted. The measured ratio of multiplicity at 91 GeV to that at 29 GeV is $2.77 \pm 0.64 \pm 0.42$ with full systematic errors quoted. These results are summarized in Table 23, together with the predictions of the Lund, Webber, and UCLA models.

The Lund Monte Carlo, using strange suppression factor $\gamma_s = 0.3$, predicts a value of K^0 per hadronic event at 29 GeV which is quite a bit higher than the measurement made here and by other experiments at PEP, but matches the trend of multiplicity measurements made at PETRA by JADE and TASSO. The value it predicts at 91 GeV is over 3σ higher than the measurement made here. Reducing the strange suppression factor reduces the production of strange quarks and thus gives predictions for K^0 multiplicity closer to the values measured here; however, the ratio of multiplicities is fairly resistant to a change in the strange suppression factor. The Lund Monte Carlo predicts a ratio which is 2σ from the value measured here. Therefore the Lund model, although high in its predictions, agrees within errors with the measurements made here.

For the Λ multiplicities, the Lund Monte Carlo predicts a value at 29 GeV which is higher than the measurement made here by 4σ but also higher than the

TABLE 23. The results of this measurement on K^0 and Λ multiplicities are given, together with the ratio of the multiplicities and the predictions of the Lund, Webber, and UCLA models.

$< K^0 >$	29 GeV	91 GeV	Ratio 91 GeV: 29 GeV
Data	$1.26 \pm 0.04 \pm 0.14$	$1.54 \pm 0.21 \pm 0.18$	$1.22 \pm 0.17 \pm 0.20$
Lund $\gamma_s = 0.3$	1.39	2.23	1.60
Lund $\gamma_s = 0.27$	1.29	2.05	1.59
Webber	1.72	2.51	1.46
UCLA	1.34	2.01	1.50
$< \Lambda >$	29 GeV	91 GeV	Ratio 91 GeV: 29 GeV
Data	$0.170 \pm 0.015 \pm 0.018$	$0.47 \pm 0.10 \pm 0.05$	$2.77 \pm 0.64 \pm 0.42$
Lund $\gamma_s = 0.3$	0.229	0.408	1.78
Lund $\gamma_s = 0.27$	0.209	0.384	1.84
Webber	0.117	0.206	1.76
UCLA	0.191	0.368	1.97

world average by 1.5σ. For $\gamma_s = 0.27$, which gives better agreement with the K^0 multiplicity measured here, it matches the world average and gives a value 2.5σ higher than the measurement made here. At 91 GeV, the Lund Monte Carlo prediction is well within errors of the multiplicity measured here. The lower γ_s gives a lower value but it is also within errors. The ratio of Λ multiplicities at 91 GeV and 29 GeV from the Lund Monte Carlo is about 1.5σ lower than the value measured here.

The Lund Monte Carlo therefore predicts a faster growth in K^0 multiplicity and a slower growth in Λ multiplicity than appears in the measurements made here, but the statistical errors are such that the discrepancy is not conclusive.

The Webber model, as tuned to general hadronic shape variables by the Mark II, has more severe discrepancies with the data. It predicts values of $< K^0 >$

at 29 GeV and at 91 GeV which are higher by more than 3σ of the statistical error than the values measured here. The ratio of its predictions agrees better; it finds a ratio of multiplicities which is within 2σ of the value measured here. Reducing the cluster masses by tuning the parameters of the Monte Carlo could bring the total multiplicities for K^0 into better agreement.

However, this would cause more problems with the Λ multiplicities: the Webber model predicts a Λ multiplicity at 29 GeV which is low compared to the value measured here by 3.5σ, and low compared to the world average by 6σ. At 91 GeV, it predicts a value for the Λ multiplicity which is 2.5σ below the value measured here. A tuning of the cluster masses down to reduce the K^0 multiplicity would further reduce the Λ multiplicities, which already disagree badly with the data. The ratio of Λ multiplicities predicted by the Webber Monte Carlo agrees better with the data than its absolute multiplicity predictions.

The UCLA model predicts multiplicities for K^0 at 29 GeV and 91 GeV which agree better with the values measured here than do the Lund model with $\gamma_s = 0.3$ and the Webber model, differing by about 2σ in both cases. The ratio of the multiplicities at the two energies also agrees better with the value measured here than do the ratios predicted by other models, probably due to the inclusion of dependence on center-of-mass energy in the UCLA model.

For the Λ multiplicities, the UCLA model prediction at 29 GeV agrees better than the other three models with the value measured here, differing by less than 1.5σ; however, it is lower than the world average. The value at 91 GeV is about 1σ low from the measurement made here, agreeing about as well as the Lund Monte Carlo. The ratio of the multiplicities at the two energies is 1.97 for the UCLA model; this gives better agreement than the other two models, but is still more than 1σ lower than the value measured here.

Of the three models, the UCLA model seems to agree best with the K^0 and Λ multiplicities measured here. The Lund model also agrees fairly well, particularly with a retuning of the strange suppression factor. The Webber model

fails to duplicate the absolute multiplicities well, but agrees about as well as the other models on the multiplicities.

In addition to overall K^0 and Λ multiplicities, various kinematic distributions have been examined and compared with the models. Only the Lund and Webber models are included in this comparison, since the kinematics of the UCLA model are similar to those of the Lund model and statistics are too low here to differentiate the two.

The momentum and scaled momentum distributions of the K^0 and Λ agree fairly well between the data and both the Lund and Webber Monte Carlos. The momentum spectrum of the Λ may be slightly softer than that predicted by Lund and harder than that predicted by Webber, but no definite conclusion can be made, given the statistics. The distributions for the K^0 agree well at both energies.

Distributions in rapidity also agree well for K^0 at both energies, with no discrimination between the models possible. For the Λ at 29 GeV the Webber Monte Carlo gives a peak at low rapidity which does not duplicate the data well; however, the Lund Monte Carlo gives a harder rapidity spectrum than the data. At 91 GeV and both models agree with the data.

The behavior of the $p_\perp$ spectra both in and out of the event plane show that the data is behaving as expected. The strange particles have more transverse momentum in the event plane than out, as expected for strange particles produced in gluon jets. The transverse momentum spectrum in the event plane for the 91 GeV K^0 may be slightly harder than expected by the Monte Carlos. Otherwise the predictions and the data agree well.

The production of K^0 and Λ *versus* sphericity was also studied. The data show the expected increase in multiplicity with sphericity. This increase is in large part due to the fact that larger multiplicity events tend to be more spherical; however, gluon radiation and heavy quark production are expected to increase both the event sphericity and the strange particle production. Unfortunately, statistics at high sphericity are too low to make these comparisons meaningful.

So far, the various hadronization models seem to do a good job at predicting hadronization at 91 GeV with the parameters tuned at lower energies, at least in their predictions of kinematic distributions for the K^0 and Λ. They have already been shown to duplicate the general event kinematics well. The discrepancy between the model predictions and the absolute multiplicities measured here may be an indication of some aspect of fragmentation which is not taken into account well; however, the discrepancies can be purely the result of statistical and systematic errors, since both the Lund model and the UCLA model are within 3σ of errors for all multiplicities. The Webber Monte Carlo shows a more severe disagreement with the data, indicating that the three parameter fit and cluster decays of the Webber model is probably failing to take some aspect of fragmentation into account. The UCLA model shows the best agreement with measured multiplicities and does it with only a few parameters in the Monte Carlo.

So far measurements at 91 GeV show some possible deviations from model predictions, but much more data is needed to determine whether these are real effects or statistical fluctuations. With the large samples of K^0 and Λ available at LEP, many more tests of our understanding of hadronization can be made which were not possible here. Correlations between K^0 and Λ can be studied, as can polarization of Λ produced in fragmentation. With these fine tests of fragmentation effects, it may be possible to tune our understanding of hadronization further, even in the absence of firm theoretical calculations.

REFERENCES

1. H. Becquerel, *Comptes rendus des Seánces de l'Academie des Sciences* **122**:502 (Seánce of March 2 1896).

2. J. J. Thomson, *London, Dublin, and Glasgow Philosophical Magazine and Journal of Science*, series 5, 44, no. 269, (1897) 293.

3. E. Rutherford, *Proceedings of the Manchester Literary and Philosophical Society*, series 4, 55, no.1 (March 1912) 18.

4. S. L. Glashow, *Nuc. Phys.* **22** (1961) 589;

   S. Weinberg, *Phys. Rev. Lett.* **19** (1967) 1264;

   A. Salam and J. C. Ward, *Phys. Lett.* **13** (1964) 168.

5. For further discussion of the standard model, see *e.g.* F. Halzen and A. Martin *Quarks and Leptons: An Introductory Course in Modern Particle Physics*, (John Wiley & Sons, New York, 1984).

6. G. S. Abrams *et al., Phys. Rev. Lett.* **63** (1989) 2173;

   P. Aarnio *et al., Phys. Lett.* **B231** (1989) 539;

   M. A. Akrawy *et al., Phys. Lett.* **B231** (1989) 530;

   D. Decamp *et al., Phys. Lett.* **B231** (1989) 519;

   B. Adeva *et al., Phys. Lett.* **B231** (1989) 509.

7. a partial list includes:

   G. S. Abrams *et al., Phys. Rev. Lett.* **63** (1989) 2447;

   D. Decamp *et al., Phys. Lett.* **B236** (1990) 511;

   P. Aarnio *et al.,* CERN preprint CERN-EP/90-49 (submitted to *Phys. Lett. B*);

   M. A. Akrawy *et al., Phys. Lett.* **B236** (1990) 364.

8. R. Field and R. Feynman, *Phys. Rev.* **76** (1949) 749,746

9. G. Altarelli and G. Parisi, *Nuc. Phys.* **B126** (1977) 298.

10. J. D. Bjorken, in *Proc. SLAC Summer Institute on Part. Physics*, SLAC-**167** (1973) Vol. 1 p. 1

examined through the distributions of rapidity and momentum transverse to the thrust both in and out of the event plane. The dependence of K^0 and Λ production on the sphericity of the hadronic events is also examined. All these distributions show that the behavior of K^0 and Λ in hadronic events is consistent with the hadronization models.

11. W. Bartel *et al.,Z. Phys.* **C21** (1983) 37;

    W. Bartel *et al.,Phys. Lett.* **B134** (1984) 275;

    W. Bartel *et al.,Phys. Lett.* **B157** (1985) 340;

    H. Aihara *et al.,Z. Phys.* **C28** (1985) 31;

    W. Althoff *et al.,Z. Phys.* **C29** (1985) 29.

12. W. Bartel *et al., Phys. Lett.* **104b** (1981) 325;

    M. Althoff *et al., Z. Phys.* **C17** (1983) 5.

13. T. D. Gottschalk and M. P. Shatz, *Phys. Lett.***B150**, (1985) 451.

14. T. Sjöstrand and M. Bengtsson, *Comput. Phys. Commun.* **43** (1987) 367;

    M. Bengtsson and T. Sjöstrand, *Nuc. Phys.* **B289** (1987) 810;

    B. Andersson *et al., Phys. Rept.* **97** (1983) 33.

15. A. Peterson *et al., Phys. Rev.* **D37** (1988) 1.

16. W. Braunschweig *et al., Z. Phys.* **C41** (1988) 359.

17. C. D. Buchanan and S.-B. Chun, UCLA-HEP-80-003, June 1989;

    C. D. Buchanan and S.-B. Chun, *Phys. Rev. Lett.* **59** (1987) 1997.

18. K.G. Wilson, *Phys. Rev.* **D10** (1974) 2445.

19. B. R. Webber, *Nuc. Phys.* **B238** (1984) 492;

    G. Marchesini and B. R. Webber, *Nuc. Phys.* **B238** (1984) 1;

    G. Marchesini and B. R. Webber, *Nuc. Phys.* **B310** (1988) 461.

20. D. Amati and G. Veneziano, *Phys. Lett.* **B83** (1979) 87.

21. J. J. Aubert *et al., Phys. Rev. Lett.* **33** (1974) 1404;

    J.-E. Augustin *et al., Phys. Rev. Lett.* **33** (1974) 1406.

22. SLAC-0171, *A Proposal for a Positron-Electron Colliding-Beam Storage Ring Project (PEP)*, April 1974.

23. C. von Zanthier *et al.,* SLAC-PUB-5213, LBL-28859, March 1990

24. SLAC-229, *SLAC Linear Collider Conceptual Design Report*, June 1980.

25. W. A. Koska *et al., Nucl. Instr. and Meth.* **A286** (1990) 32.

26. R. Fulton *et al., Nucl. Instr. and Meth.* **A274** (1989) 37.

27. G. Abrams *et al., Phys. Rev. Lett.* **63** (1989) 2173.

28. G. Abrams *et al., Nucl. Instr. and Meth.* **A281** (1989) 55.

29. G. Hanson *et al., Nucl. Instr. and Meth.* **A252** (1983) 343.

30. D. Briggs *et al., IEEE Trans. Nucl. Sci.* **NS-32** (1985) 653.

31. D. Bernstein *et al., IEEE Trans. Nucl. Sci.* **NS-33** (1986) 86.

32. H. Brafman *et al., IEEE Trans. Nucl. Sci.* **NS-32** (1985) 336.

33. J. Perl *et al., Nucl. Instr. and Meth.* **A252** (1986) 616.

34. A. Weinstein and P. Burchat, Mark II/SLC Note **155**, October 1986.

35. G. S. Abrams *et al., IEEE Trans. Nucl. Sci.* **NS-25** (1978) 309.

    G. S. Abrams *et al., IEEE Trans. Nucl. Sci.* **NS-27** (1980) 59.

36. E.L. Cisneros *et al., IEEE Trans. Nucl. Sci.* **NS-24** (1977) 413.

37. M. Breidenbach *et al., IEEE Trans. Nucl. Sci.* **NS-25** (1978) 706.

38. C. Blocker, Ph.D. thesis, University of California, Berkeley, LBL-10801 (1980).

39. J. A. Kadyk, *Proceedings of the Gas Sampling Calorimetry Workshop II.* Batavia, IL (1985) 373.

40. W. T. Ford *et al., Nucl. Instr. and Meth.* **A255** (1987) 486.

41. P. Baringer *et al.,* IUHEE-12, SLAC-PUB-3390 (1984).

42. J. Seeman *et al.,* SLAC-PUB-3945, April 1986.

43. H. Brafman *et al.,* SLAC-PUB-2033, October 1977;

    T. Himel, Ph. D. thesis, SLAC-REP-223, October 1979.

44. R. Alekson *et al., Proceedings of the International Conference on The Impact of Digital Microelectronics and Microprocessors on Particle Physics, World Scientific* (1988) 38.

45. D. J. Nelson *et al., IEEE Trans. Nucl. Sci.* **NS-28** (1981) 336.

46. E. J. Siskind, *IEEE Trans. Nucl. Sci.* **NS-30** (1983) 188.

47. A. J. Lankford and T. Glanzman, *IEEE Trans. Nucl. Sci.* **NS-31** (1984) 225;

T. Barklow *et al., IEEE Trans. Nucl. Sci.* **NS-33** (1986) 775.

48. Particle Data Group, M. Aguilar-Benitez *et al., Phys. Lett.* **B170** (1986).

49. G. S. Abrams *et al., Phys. Rev. Lett.* **64** (1990) 1334.

    K. O'Shaughnessy, Ph.D. thesis, **SLAC-Report-360** (1990).

50. J. Dillon, VFINDP Vee Finder, Trilling-Goldhaber Group Physics note #232 (March 1982).

51. R. Jacobsen, *private communication,* (August, 1990).

52. W. Bartel *et al., Z. Phys.* **C20** (1983) 187.

53. W. Braunschweig *et al., Z. Phys.* **C47** (1990) 167.

54. H. M. Schellman *et al., Phys. Rev.* **D31** (1985) 3013

55. H. Aihara *et al., Phys. Rev. Lett.* **53** (1984) 2378.

56. M. Derrick *et al., Phys. Rev.* **D35** (1987) 2639.

57. H.-J. Behrend *et al., Z. Phys.* **C46** (1990) 397.

58. C. de la Vaissiere *et al., Phys. Rev. Lett.* **54** (1985) 2071.

59. H. Aihara *et al., Phys. Rev. Lett.* **54** (1985) 274.

60. H. Aihara *et al.,* **UCLA-HEP-90-002** (May 1990).

61. W. Braunschweig *et al., Z. Phys.* **C45** (1989) 209.

62. W. Bartel *et al., Phys. Lett.* **B104** (1981) 325.

63. C. D. Buchanan, *private communication* (October 1990).